

## Bake hardening effect in advanced high-strength steels

*Master's thesis in Applied Mechanics*

KARL LINDQVIST

Department of Applied Mechanics  
Division of Material and Computational Mechanics  
CHALMERS UNIVERSITY OF TECHNOLOGY  
Gothenburg, Sweden 2013  
Master's thesis 2013:16



MASTER'S THESIS IN APPLIED MECHANICS

# Bake hardening effect in advanced high-strength steels

KARL LINDQVIST

Department of Applied Mechanics  
*Division of Material and Computational Mechanics*  
CHALMERS UNIVERSITY OF TECHNOLOGY

Gothenburg, Sweden 2013

Bake hardening effect in advanced high-strength steels  
KARL LINDQVIST

© KARL LINDQVIST, 2013

Master's thesis 2013:16  
ISSN 1652-8557  
Department of Applied Mechanics  
Division of Material and Computational Mechanics  
Chalmers University of Technology  
SE-412 96 Gothenburg  
Sweden  
Telephone: +46 (0)31-772 1000

Cover:

Temperature field in virgin (as-rolled) and work- and bake hardened specimens at maximum force;  
From left to right: Docol 1200M virgin, Docol 1200M work+bake hardened, Docol 600DP virgin, Docol 600DP  
work+bake hardened

Chalmers Reproservice  
Gothenburg, Sweden 2013

Bake hardening effect in advanced high-strength steels  
Master's thesis in Applied Mechanics  
KARL LINDQVIST  
Department of Applied Mechanics  
Division of Material and Computational Mechanics  
Chalmers University of Technology

## ABSTRACT

---

The yield- and tensile strength in cold-formed components of advanced high strength steels can be significantly affected by the paint-baking cycle employed in automotive production lines. Typically, a 10 % increase in yield strength is observed after pre-straining and baking. In addition, adverse effects on the apparent ductility of martensitic steels have been reported. It is of interest to include these phenomena in subsequent simulations of component behavior in order to predict realistic in-service strength and failure properties.

In the present work, an experimental programme that details the effect of bake hardening in dual-phase and martensitic steels is presented. A constitutive model that accounts for bake hardening is also evaluated with respect to strength and failure prediction. Results show that after baking, the dual-phase steel deforms smoothly and uniformly. On the contrary, strain localization and failure was observed immediately after yielding of the martensitic steel, both in uniaxial and plane strain tension tests. The strength increase in non-proportional loading was very small for both materials.

The predictive capability of the constitutive model is shown to be rather poor for the dual-phase steel. The strength after baking was overpredicted in all validation cases, most likely owing to the assumption of isotropic bake hardening. In the martensitic steel, however, a good representation of strength and failure in material tests was found for small plastic strains and a sufficiently fine spatial discretization. More work is needed to properly account for the strengthening due to bake hardening, but the model show adequate failure prediction of martensitic steels.

Keywords: Bake hardening, strain aging, strain ageing, dual-phase steel, martensitic steel, constitutive modeling, tensile testing



## PREFACE

---

The work presented in this report was conducted in close collaboration with CRI SIMLab, a research centre hosted by the Norwegian University of Science and Technology (NTNU) in Trondheim, Norway. The work was also made possible through cooperation with the research organization SINTEF and steel manufacturer SSAB. I would like to express my gratitude to all involved in the project, especially my supervisors, Adjunct Professor Odd-Geir Lademo (SINTEF) and Professor Odd-Sture Hopperstad (NTNU). Their continuous support, helpfulness and interest in my work has been invaluable.

I would also like to thank the following individuals for their contributions:

- Dr. Stéphane Dumoulin, Research Scientist at SINTEF, for extensive help and tutorials in LS-DYNA as well as happily answering all my questions
- Dr. Torodd Berstad, Researcher at NTNU, for practical help, many good explanations and superior insight in numerical methods
- Dr. Egil Fagerholt, Postdoc. at NTNU, for continuously giving me the latest version of your DIC code straight from the compiler
- Trond Auestad, Senior Engineer at NTNU, for assistance with the experimental tests
- Dr. Joachim Larsson, Manager, Structural technology at SSAB, for a good introduction to bake hardening as well as providing test samples
- Arne Gellein, Senior Technician at SINTEF, for practical help with specimen preparation

Finally, thanks are due to my colleagues at the Department of Applied Mechanics and Corrosion at SINTEF Materials and Chemistry for treating me as one of you.

Karl Lindqvist

Trondheim  
June, 2013



# CONTENTS

---

1	INTRODUCTION	1
1.1	Purpose . . . . .	2
1.2	Objective . . . . .	2
1.3	Scope . . . . .	2
1.4	Outline of the thesis . . . . .	3
2	THEORETICAL FRAMEWORK	5
2.1	Plasticity and constitutive modeling . . . . .	5
2.1.1	Yield criterion . . . . .	6
2.1.2	Work hardening . . . . .	7
2.1.3	Formability . . . . .	9
2.2	Bake hardening . . . . .	10
2.2.1	History . . . . .	10
2.2.2	Phenomenology . . . . .	11
2.2.3	Mechanisms . . . . .	13
2.2.4	Influence of temperature and time . . . . .	15
2.2.5	Influence of pre-straining . . . . .	16
2.2.6	Constitutive modeling . . . . .	17
2.3	Characterization methods . . . . .	18
2.3.1	Uniaxial tension test . . . . .	18
2.3.2	Plane strain tension test . . . . .	20
3	METHOD	23
3.1	Experimental studies . . . . .	23
3.1.1	Uniaxial tension tests . . . . .	23
3.1.2	Plane strain tension test . . . . .	26
3.2	Modeling approach . . . . .	27
3.3	Parameter identification procedure . . . . .	29
3.3.1	Curve fitting . . . . .	29
3.3.2	Inverse modeling . . . . .	30
3.4	Numerical simulations . . . . .	31
3.4.1	PST geometry . . . . .	31
3.4.2	Plane strain tension test . . . . .	33
3.4.3	Plane strain bending test . . . . .	34
4	RESULTS AND ANALYSIS	39
4.1	Experimental studies . . . . .	39
4.1.1	Uniaxial tensile tests . . . . .	39
4.1.2	Plane strain tension tests . . . . .	42
4.2	Parameter identification . . . . .	46
4.3	Numerical simulations . . . . .	47
4.3.1	Plane strain tension test . . . . .	47

4.3.2	Plane strain bending test . . . . .	47
5	DISCUSSION . . . . .	51
5.1	Characteristics of bake hardening . . . . .	51
5.2	Evaluation of constitutive model concept . . . . .	53
6	CONCLUDING REMARKS . . . . .	55
6.1	Summary and conclusion . . . . .	55
6.2	Recommendations for further work . . . . .	56
	FIGURES AND TABLES, CHAPTER 4 . . . . .	57
A	DETAILS OF THE EXPERIMENTAL TESTS . . . . .	85
A.1	Uniaxial tension test . . . . .	85
A.2	Plane strain tension test . . . . .	87
	BIBLIOGRAPHY . . . . .	89

## INTRODUCTION

---

In the ongoing challenge of creating lighter and stronger components out of sheet metal, the automotive industry cooperate closely with major steel manufacturers towards further development of formable high-strength steel materials [3]. A significant driver for this development is the highly competitive vehicle market and pressure from legislations towards cars with simultaneously improved fuel efficiency, safety, equipment level and, as of recent, battery storage [7]. Advances in materials technology are used as a key component in achieving these goals. Specifically, high-strength steels are candidates for use in structural body parts and energy absorbing components since their high strength permits use of thinner gauges. This in turn lowers a significant portion of the total weight while retaining energy absorption and stiffness properties of the car body [7, 3].

Bake hardening is an important part of achieving a high strength in certain sheet metals without excessive degradation of ductility. In automotive applications, the strengthening occurs during the finishing heat treatment of the paint coating, i.e. after forming and assembly. The baking is typically undertaken at 160°C for 20 minutes [22]. In a bake hardenable steel material, this temperature causes interstitial atoms (mainly carbon) to interact with dislocations that were created during forming of the product, giving increased yield strength as well as increased tensile strength [33, 34].

Practical testing of dual phase and martensitic steels [18] has indicated that the yield strength is increased by about 10% for a typical painting cycle. The magnitude of the bake hardening effect could be of the same order as the increase of the yield stress due to work hardening during the forming process, and should therefore be accounted for in simulations of component behavior. Material tests have concurrently shown that in certain conditions, bake hardened steel is susceptible to plastic instability modes leading to early material failure. It is of both academic and industrial interest to study the details of the bake hardening effect in order to explain why such failures occur, and to formulate a constitutive model that can represent changes in strength and ductility due to baking.

Some principal outcomes of the competence centre CRI SIMLab, hosted by the Norwegian University of Science and Technology, are numerical implementations of constitutive models and fracture criteria. In the present context, a versatile metal model has been developed that allows representation of the various phenomena that affects the mechanical characteristics of metals and alloys in for instance struc-

tural impact analyses. An experimental study on two advanced high-strength steels, Docol 600DP and Docol 1200M, has earlier been carried out in collaboration with the Swedish steel manufacturer SSAB and has formed as basis for the related modeling strategy in the SIM-Lab Metal Model. The overall objective of the ongoing research is to develop a material model that takes the bake hardening effect into account, in order to gain fundamental understanding and promote industrial use of these materials. However, additional work is needed to study and document the characteristics of the plastic deformation and to evaluate the proposed model concept (i. e. the constitutive model, along with assumptions and simplifications) with respect to its accuracy in representing the strength and ductility of high-strength steels subjected to paint baking.

### 1.1 PURPOSE

The purpose of the present work is *to study the bake hardening effect in two advanced high-strength steels and to assess the capability of an existing modeling strategy to represent the findings*. In particular, the constitutive model's ability to be used in predictive design will be addressed.

### 1.2 OBJECTIVE

In accordance with the above, the objectives are formulated as follows:

- A. To investigate and document the characteristics of deformation bands, strain localization and failure of material tests of Docol 600DP and Docol 1200M and how these are affected by paint baking.
- B. To evaluate the existing model concept with respect to its accuracy in representing the response and structural ductility of simple and complex (though generic) components.

### 1.3 SCOPE

The present work is an experimental and numerical study that builds upon the previous work of [Hopperstad et al. \[20, 21, 26\]](#). The experimental work will focus on detailing the results of previous work, as well as to extend the experimental tests to other stress states. Component tests are outside the scope of this work, but the relevance of this work for such tests will be discussed. The numerical parts of this work include simulations of material tests, both from previous and present experimental work.

It is not the purpose of this thesis to improve the existing model concept, but to evaluate its efficacy and explore methods of parame-

ter identification. Therefore, the SIMLab Metal Model will be used to as large extent as possible in the simulations and the modeling strategy outlined by Hopperstad et al. will be applied. Assumptions and possible areas of improvement are discussed in the closing chapters.

Finally, to limit the scope of the parameter identification, fracture modeling is excluded from the present work. Although it is possible to calibrate stress based fracture criteria on basis of this work, it is not considered central to the objectives outlined above.

#### 1.4 OUTLINE OF THE THESIS

This report is divided into 5 chapters. After the introduction, [Chapter 2](#) give a theoretical motivation to the approach chosen in the present work and presents an introduction to the observed phenomena and underlying physics of bake hardening. [Chapter 3](#) explain the steps, procedures and calculations carried out in the course of the present work and [Chapter 4](#) present the results of these procedures. An analysis of the results is also given. In [Chapter 5](#), the results of the present work are discussed in a broader context and viewed in light of the objectives presented in this introduction. The report ends with summary and conclusions, given in [Chapter 6](#).



## THEORETICAL FRAMEWORK

---

This chapter aims at briefly introducing the observed phenomena and underlying physics of bake hardening and give a theoretical motivation to the approach chosen in the present work. The reader is assumed to be familiar with metal plasticity and phenomenological strength of materials, so only a short introduction is given. In addition, the modeling approach adopted in this work is presented and relevant testing methods that has been used successfully to calibrate material models are reviewed.

### 2.1 PLASTICITY AND CONSTITUTIVE MODELING

Figure 1 show a schematic stress-strain behavior of an engineering metal in uniaxial tension, as well as two possible behaviors under reloading. Plastic deformation occurs when the elastic limit, characterized by the yield stress,  $\sigma_0$ , is exceeded. At this point, permanent deformation is produced by the movement of lattice defects, *dislocations*, along activated *slip planes* [9]. The importance of dislocations for the bake hardening effect will be discussed later in the chapter. Plastic deformation beyond the yield point is characterized by formation of new dislocations and an increase of the stress level due to *work hardening*. As shown by the indicated unloading path, the plastic part of the deformation is permanent and the total strain can be decomposed into an elastic and a plastic component:

$$\varepsilon = \varepsilon^e + \varepsilon^p$$

Upon reloading, the material will remain elastic up to the point where it was unloaded,  $\sigma^*$ . This is the new yield stress caused by the work hardening. If the loading direction is reversed, however, the yield stress is often observed to be lower than  $\sigma^*$ . This effect is neglected in many situations, but can be significant in for example bending situations where tensile and compressive stresses occur simultaneously.

When it comes to constitutive modeling, significant simplifications can be made if a material can be assumed to be isotropic. This assumption can apply to several of the above mentioned phenomena, such as isotropic elasticity, isotropic yielding, isotropy in plastic flow and isotropic work hardening. The modeling strategy adopted in the present work is motivated and presented in the following two sections.

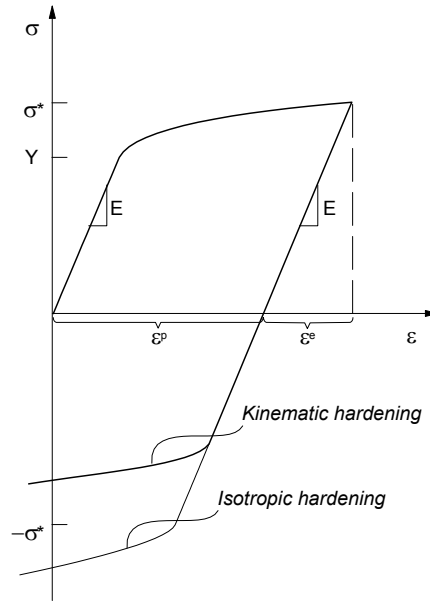


Figure 1: Schematic stress-strain behavior of a structural metal, after [23]

### 2.1.1.1 Yield criterion

The purpose of a yield criterion and its related yield surface is to translate an arbitrary multiaxial stress state to an equivalent stress and use it to determine whether yielding occurs or not. Moreover, if the associated flow rule is adopted, the yield surface also determines the direction of plastic flow. Finally, a work hardening rule that describes expansion and translation of the yield surface as a function of plastic strain is needed.

In his work on a dual phase steel very similar to the one studied in this work, Gruben [17] adopted a  $J_2$  (von Mises) plasticity model and compared its applicability with a high exponent yield criterion in numerical representation of deformation and ductile fracture of several different material tests. It was concluded that the results from numerical models using von Mises plasticity were in good agreement with experimental findings in all but one case (an Arcan test in  $45^\circ$ ). For the Arcan  $45^\circ$  test, a high exponent model gave improved agreement.

Previous work at SIMLab has also shown that a calibrated von Mises plasticity model with isotropic work hardening provides a good description of virgin Docol 600DP material in other stress states than the one for which it was calibrated [26].

Since von Mises plasticity has proven to be adequate for dual phase steels, it will be adopted also for the present work. Although Docol 1200M has been shown to have significant anisotropy in plastic flow [18], the focus of this thesis will rather be on modeling the work

hardening. Thus, the yield function  $f$ , associated flow rule and consistency condition can be stated according to Equation (1) below.

$$\begin{aligned} f(\boldsymbol{\sigma}) &= \sigma_{eq} - (\sigma_0 + R(p)) \leq 0 \\ \dot{\boldsymbol{\epsilon}}_p &= \dot{\lambda} \frac{\partial f}{\partial \boldsymbol{\sigma}} \\ \dot{f} \dot{\lambda} &\leq 0 \end{aligned} \quad (1)$$

where  $\sigma_{eq}$  is the second invariant of the deviatoric stress tensor, viz.

$$\sigma_{eq}(\boldsymbol{\sigma}) = \sqrt{\frac{3}{2} \boldsymbol{\sigma}' : \boldsymbol{\sigma}'} \quad (2)$$

and  $p$  is the equivalent (non-decreasing) plastic strain.

### 2.1.2 Work hardening

The vast majority of all metals used for engineering purposes are polycrystalline, and the grain boundaries that constitute the interface between neighboring grain lattices act as a barrier for dislocation movement [9]. The result is that dislocations pile up at the grain boundaries along the active slip plane. This dislocation pile-up is responsible for work hardening during early stages of straining. In single crystals, and in later stages of straining of polycrystals, work hardening is caused by dislocations interacting with each other and with elements dissolved in the lattice (foreign atoms, precipitates etc.) [9].

A common approach to model work hardening is through an isotropic two component Voce rule, see (3). It consists of two exponential terms that are determined by their saturation values at infinite strain,  $Q_1$  and  $Q_2$  [MPa], and the initial slope of each component,  $\theta_1$  and  $\theta_2$  [-]. By these parameters, the whole stress-strain curve is normally accurately represented.

$$R(p) = Q_1(1 - e^{-\frac{\theta_1}{Q_1} p}) + Q_2(1 - e^{-\frac{\theta_2}{Q_2} p}) \quad (3)$$

One particular feature that will be used in this thesis is the possibility to update the parameters to account for pre-straining. One situation where this can be convenient is in numerical modeling of reloading of a pre-strained test specimen. If isotropic hardening can be assumed, the expansion of the yield surface due to the pre-straining,  $p_0$ , can be recast as an update in the yield stress and work hardening parameters. The benefit of using such approach is that the numerical model need not know the history of the material (i. e. the effective plastic strain imposed by the pre-straining).

Consider a single Voce term with initial parameters  $Q$  and  $\theta$  which is given a pre-strain  $p_0$ . If the plastic strain is reset after pre-straining

such that  $p$  starts from zero, the hardening curve will follow the following rule upon reloading:

$$\begin{aligned} R(p) &= Q \left( 1 - e^{-\frac{\theta}{Q}(p+p_0)} \right) \\ &= Q \left( 1 - e^{-\frac{\theta}{Q}p_0} e^{-\frac{\theta}{Q}p} \right) \end{aligned}$$

By introducing  $A = e^{-\frac{\theta}{Q}p_0}$  and adding and subtracting  $QA$ ,

$$\begin{aligned} R(p) &= Q - QAe^{-\frac{\theta}{Q}p} + QA - QA \\ &= \underbrace{QA}_{Q_{new}} \left( 1 - e^{-\frac{\theta}{Q}p} \right) + \underbrace{Q(1-A)}_{\Delta\sigma_0} \end{aligned} \quad (4)$$

As seen, the rate of saturation  $\frac{\theta}{Q}$  is unchanged while the saturation level  $Q$  and the yield stress is changed.

A problem that can arise with the Voce rule is that experimental data is only available for very small strains while a problem at hand require a constitutive model which is valid up to very large strains ( $\varepsilon^P \approx 1$ ). This can occur if the material is susceptible to early diffuse necking in uniaxial tension. In such situations, the work hardening model can be augmented with a power law (Ramberg-Osgood) type model calibrated such that only one additional parameter, the stress at 100% plastic strain, need to be determined. This leads to the following hardening rule:

$$R(p) = \begin{cases} \sum_{i=1}^2 Q_i (1 - e^{-\frac{\theta_i}{Q_i} p}) & \text{for } \varepsilon^P \leq \varepsilon_t \\ A + Bp^n & \text{for } \varepsilon^P > \varepsilon_t \end{cases} \quad (5)$$

where  $\varepsilon_t$  is a transition strain and the parameter  $A, B, n$  are chosen to give  $C_1$ -continuity of the hardening curve at the transition strain as well as to satisfy

$$\sigma_0 + R(p = 1) = \sigma_{100}$$

In this thesis, a kinematic hardening rule is used to represent the Bauschinger effect in the plane strain bending simulations. The evolution of the back stress tensor used in the SIMLab Metal Model can be expressed as [12]

$$\chi(\varepsilon^P) = \chi_0 + \text{sgn}(\sigma - \chi) Q_\chi \left( 1 - e^{-\text{sgn}(\sigma - \chi) \frac{\theta_\chi}{Q_\chi} (\varepsilon^P - \varepsilon_0^P)} \right)$$

where  $Q_\chi$  and  $\theta_\chi$  are the kinematic hardening parameters and  $\chi_0, \varepsilon_0^P$  are initial values, such as from pre-straining.

A simple approach towards including the Bauschinger effect, if cyclic tension-compression data are unavailable, is to assume that one of the two Voce rules in (3) is entirely kinematic. The motivation for such an assumption is that the rapid work hardening that appear

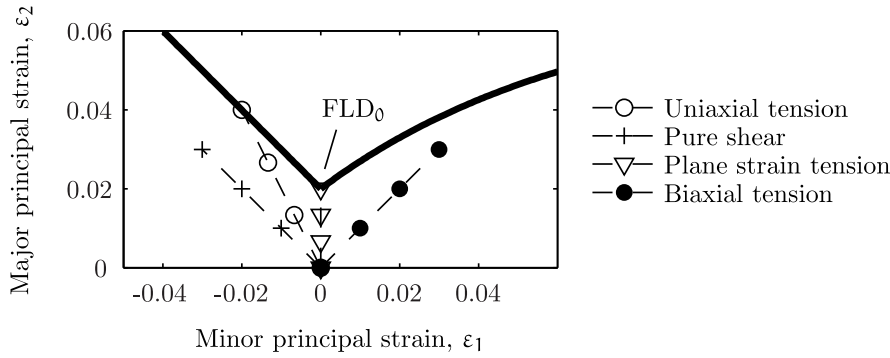


Figure 2: Schematic representation of an FLD

early in the straining can be explained by dislocation pile-up. Since this is a kinematic effect, the Voce rule that saturates first (i. e. has the highest  $\theta$  parameter) can be taken as kinematic hardening instead of isotropic.

### 2.1.3 Formability

The formability of sheet metals are commonly represented in a *forming limit diagram* (FLD). It is a representation of the failure limit of a material as a function of the in-plane strains, where the limit curve defines the onset of localized necking. While FLDs are of primary interest for forming simulations, they are also relevant for indicating material ductility in deformability and collapse analysis.

Figure 2 show the principle of an FLD and a typical failure curve, above which material failure is predicted. Different failure mechanisms are important in different areas of the FLD, and this thesis will focus on failure by strain localization. Therefore, only that curve is therefore outlined in this figure. A few stress states have also been included, where special attention should be paid to the uniaxial tension and plane strain tension paths. The lowest point of formability is denoted  $FLD_0$  and occurs in plane strain. This is exactly why plane strain tensile testing is relevant for the present work. Experimental determination of forming limit curves require considerable testing and was not considered possible in the scope of the present work. Therefore, by studying how bake hardening affect the lowest point of formability, the number of tests are limited to a reasonable amount while still giving an indication on the general trend.

Although the strain path of the uniaxial tensile test seem to give information about the formability as well, it should be noted that an actual uniaxial tensile test will undergo diffuse necking before localized necking. The triaxial state of stress inside the diffuse neck makes the strain path uncertain, and Lademo et al. has concluded that the uniaxial tensile test is unsuitable for failure predictions [24].

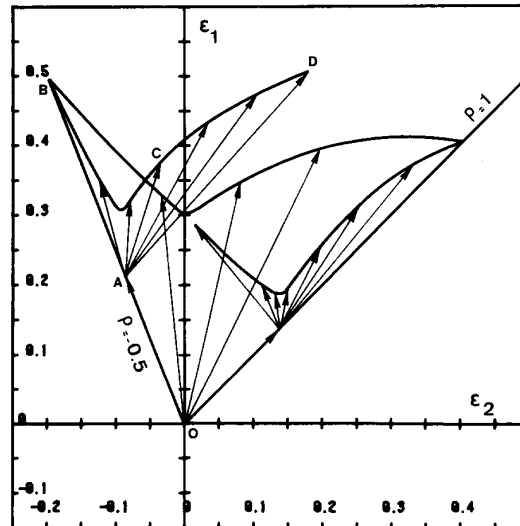


Figure 3: Experimental FLDs for Armco iron, after [6]

It is important to note that in the FLD will depend on the history of the material. Figure 3 show an example of how the forming limit curve can be affected by pre-straining, such as by the final temper rolling step in the production (close to plane strain) or from straining in a previous forming step. In the present work this has implications for the pre-straining of the plane strain tensile specimen. Ideally, the specimen should be pre-strained and tested in monotonic loading (i. e. pre-strained in plane strain) but this may not be suitable in practice. It was therefore judged that a reasonable indication of the lower limit of formability could be determined by pre-straining in uniaxial tension.

## 2.2 BAKE HARDENING

### 2.2.1 History

Conventional Bake Hardening (BH) steels were originally developed during the 1980's to offer an increased strength in cold formed sheet metal parts that require good formability [22]. By using a strengthening mechanism activated during the paint heat treatment, these steels permitted weight savings in the car body since the gauge thickness in exposed panels could be reduced without increased risk of denting. The strengthening was achieved by leaving a small amount of carbon in solid solution in the ferrite matrix, while minimizing the nitrogen content to avoid storage problems due to rapid room temperature aging [3].

In efforts to further reduce vehicle weight and maintain a high freedom in design, bake hardenable steel grades with more favorable combinations of formability and strength were developed. Notable

progress in this area are that of ultra low carbon (ULC) and interstitial free (IF) steels, of which Baker et al. [3] have done a comprehensive review. These steels show excellent formability during stretch forming [11] due to the very low concentration of interstitial elements (carbon and nitrogen) and have been used in exposed car body panels [29]. Metallurgically, however, they also belong to the “conventional” BH-steels, characterized by a single phase ferritic microstructure where grain size and grain shape are the main parameters [7].

Further demand for even higher strength levels have lead to the development of Advanced High Strength Steels (AHSS), a group of materials consisting of, among others, Martensitic, Dual Phase (DP), Complex Phase and Transformation Induced Plasticity (TRIP) steels [22]. Through a refined microstructure, these materials retain a relatively high ductility despite their very high strength. As an example, Dual Phase steels contain a soft and ductile ferritic matrix with fine dispersed grains of strong martensite, while TRIP steels utilize a plasticity-induced transformation of austenite to martensite to combine ductility and strength [8].

Figure 4 show a comparison of strength versus ductility for a few AHSS grades proposed for car body applications. This thesis concerns a dual phase steel and a martensitic steel, which are positioned in the lower right area of the above mentioned diagram (martensitic steels not shown). For formability reasons, dual phase and martensitic steels are suitable for structural components rather than visible panels. Door beams and bumper reinforcements are given by the manufacturer as typical applications [31, 30]. As illustrated in the figure, austenitic manganese steels are a promising recent development. The extent to which it has been applied to industrial products is however unknown to the author.

### 2.2.2 Phenomenology

Bake hardening steels are characterized by a significant increase in yield strength after pre-straining, such as due to forming operations, and subsequent baking. A typical material response in a uniaxial tension test after pre-straining and heat treatment is depicted in Figure 5, where the sharp yield point, the yield point elongation (yield plateau) and modified work hardening behavior are important characteristics. The increase in yield stress due to baking is commonly called  $\Delta\sigma_{BH}$  and this notation will also be used in this thesis. Note however that the response shown in Figure 5 is valid only for monotonic loading, i.e. when pre-straining and subsequent loading is in the same direction.

To study the bake hardening effect under non-monotonic loading, Ballarin et al. conducted a series of experiments on two low strength steels where the angle of straining before and after baking was var-

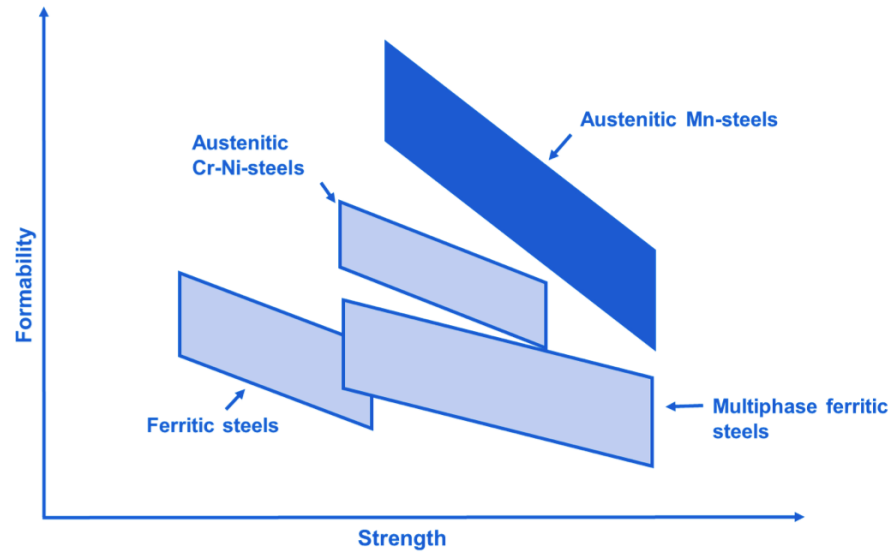


Figure 4: Strength and formability comparison of AHSS grades, after [7]

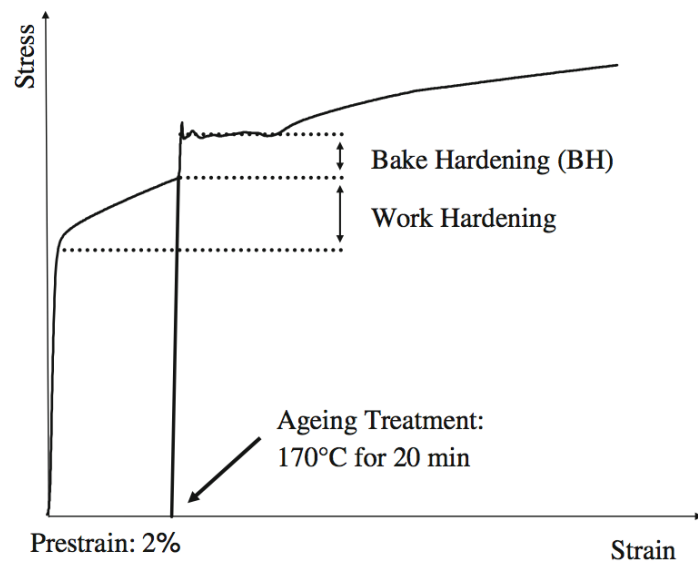


Figure 5: Schematic response of a bake hardening steel in uniaxial tension, after [5]

ied [4]. The steels showed significant strengthening in the standard testing sequence (uniaxial tension - uniaxial tension) and a slightly lower bake hardening response if the loading was reversed (i.e. uniaxial tension - uniaxial compression). For loading directions in between, such as uniaxial tension in the reference direction followed by uniaxial tension perpendicular to the reference direction, the bake hardening effect was dramatically reduced and even slightly negative. This confirmed previous investigations on similar materials, such as a study by [Hiwatashi and Yonemura \[19\]](#). The authors reported a significant Bauschinger effect in the steel after pre-straining, but the difference in yield strength was reduced during baking, rendering a positive bake hardening both in proportional reloading and in reversed loading.

The bake hardening effect in a number of Advanced High Strength Steels has previously been investigated by [Hagström and Ryde \[18\]](#). Generally, the bake hardening was manifested in a similar way as previously mentioned. A high bake hardening potential was found for all materials. However, special attention was paid to the bake hardened martensitic steels, which showed very low extension before failure in uniaxial tension. It was shown to be related to the test method, but the results still raise concern over whether the bake hardening of AHSS constitute a positive feature that should be exploited or a risk of unexpected failure that should be avoided.

Finally, the effect of bake hardening has also been studied for complex components. [Durrenberger et al.](#) studied the crash properties of a top-hat section manufactured from two different AHSS steels subjected to bake hardening. They found an increase in the mean crush force after baking for both materials, but the bake hardening had a smaller influence than the work hardening from forming operations.

To summarize, the phenomenology of bake hardening is quite involved, and significant considerations must be taken if a numerical model is to represent all of the above described phenomena. As already mentioned, and further outlined in [Section 2.2.6](#), the present work will be based on an isotropic description of the bake hardening effect. The above mentioned phenomena should however be kept in mind when interpreting the results of the present work.

### 2.2.3 Mechanisms

The increase in yield stress due to bake hardening has been attributed to a mechanism called static strain aging. It is a diffusion-governed process in which interstitial atoms such as carbon or nitrogen migrate to mobile dislocations that have been created through straining and *pin* them. By locking the existing mobile dislocations, the yield stress is increased and a discontinuous yielding behavior ap-

pear, since new mobile dislocations must be created in order to initialize plastic flow [7].

The governing kinetics of the dislocation pinning was first studied by Cottrell and Bilby in a commonly cited paper, [10]. Hence, the atmospheres that are formed around the dislocations are called Cottrell atmospheres. Wilson and Russel continued the work on strain aging, and established the following stages of aging in mild steels [32, 33, 34]:

- A. Stress induced ordering of interstitial atoms
- B. Dislocation locking by Cottrell atmospheres
- C. Solute cluster formation and precipitation

A number of physically based strain aging theories have been developed to account for the kinetics of the above mentioned processes. While a treatment of these are outside the scope of this thesis, it is worth mentioning that these theories are the basis of the constitutive modeling discussed in Section 2.2.6.

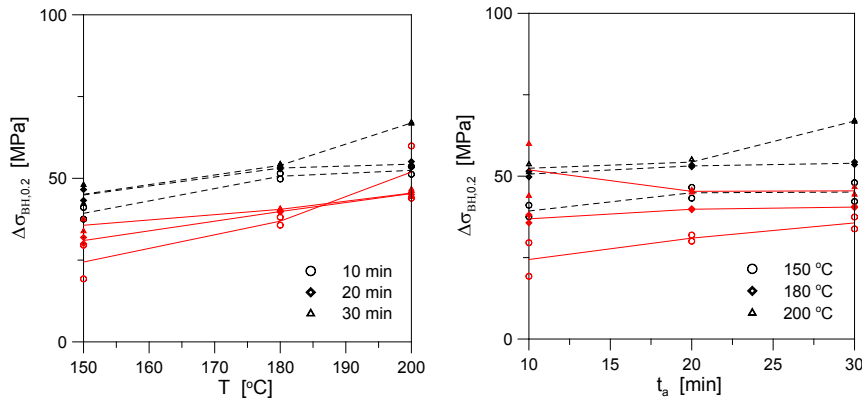
Since the baking process in automotive production lines is quite well defined with regards to time and temperature, the two latter mechanisms have been established as the ones relevant for the bake hardening of automotive steel [3]. Over long aging times, two distinct aging stages have been found. These are then explained by Cottrell locking and precipitation respectively, indicating that the Cottrell locking is a much faster hardening mechanism than the precipitation formation. The precipitation mechanism has however been questioned, since precipitates have been difficult to observe in the microstructure [3].

Bleck et al. has suggested a fourth mechanism for DP and TRIP steels with martensitic fractions, namely [8]:

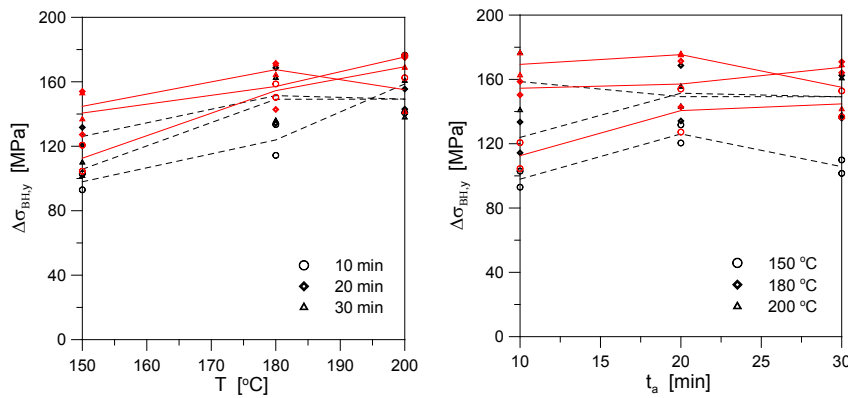
- D. Tempering of the martensitic phase

The mechanism is explained by the *geometrically necessary* dislocations that exist in a DP steel due to the change of lattice structure from BCC to FCC over the martensite-ferrite interfaces [8]. Tempering of the martensitic phase is suggested to result in a relief of local residual stresses, by which geometrically necessary dislocations become immobile or their quantity is reduced. This, in turn, gives higher yield stress. The authors also conclude that such local residual stresses, and shear stresses in the phase interfaces, are responsible for initiating plastic flow without discontinuous yielding.

Finally, it should be noted that while the discussion so far has concerned the increase in *yield stress* due to bake hardening, other parameters related to material strength are affected as well. As an example, the precipitation mechanism also lead to matrix hardening which increases the flow stress after yielding [3]. The details of these phenomena are however outside the scope of this thesis.



(a) Docol 600DP



(b) Docol 1200M

Figure 6: Influence of aging temperature, aging time and pre-strain level, after [21]. Black dashed lines signify the lower pre-strain level, while red solid lines correspond to the higher pre-strain level.

#### 2.2.4 Influence of temperature and time

A typical time- and temperature process window of the paint baking cycle in a car factory is 15-60 minutes and 160-190°C respectively [22]. In a study by Rashid [28], similar time- and temperature conditions leads to a saturation of the Cottrell locking mechanism (stage one) and onset of precipitation hardening (stage two). Similar results are indicated in the work by Ballarin et al.. However, since both Cottrell locking and precipitation are dependent on the chemical composition of the material, this conclusion can only be used as a guideline [3]. Generally, the carbon content and diffusion distances in AHSS are radically different than those of classic bake hardening steels [8].

A comprehensive study on the temperature and time influence on the bake hardening response of Docol 600DP and Docol 1200M has been carried out at SIMLab [21]. Figure 6 show the resulting increase in yield stress after bake hardening as a function of temperature and time. As seen,  $\Delta\sigma_{BH}$  varied by approximately 10-20 MPa for Docol

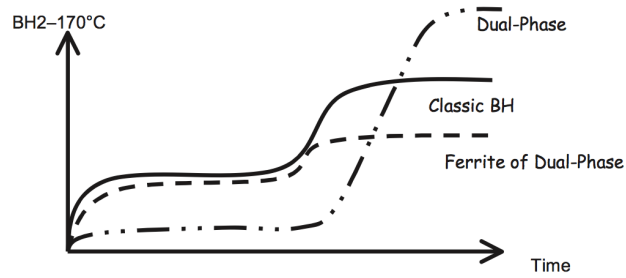


Figure 7: Schematic bake hardening kinetics over long aging times, after [8]

600DP and approximately 40-50 MPa for Docol 1200M in the studied temperature range. The authors concluded that the temperature had a more significant effect on the bake hardening than the aging time. The variations are significant, but not dramatic.

A schematic comparison of the hardening kinetics over long aging times for single phase and dual phase steel, after [8], is given in Figure 7. As seen, the maximum hardening is achieved for longer aging times than conventional bake hardening steels, and the hardening potential is greater. For the typical bake hardening treatment, 170°C for 20 min, of a prestrained DP 600 steel, Bleck et al. reports that the second stage of aging is started, but not completed. Maximum hardening was achieved after 60 minutes, and an overaging tendency is reported for very long aging times (>1000 minutes) [8].

#### 2.2.5 Influence of pre-straining

Generally, the results given in literature suggest that the yield stress increase due to Cottrell locking is highly dependent on existence of pre-strain, but not so dependent on the amount of pre-strain. De et al. studied the bake hardening of an Ultra Low Carbon bake hardening steel, and concluded that the maximum attainable increase in yield stress due to Cottrell locking was independent on the amount of pre-strain in the range 1-5% [11]. Baker et al. also refer to similar results [3].

In the study by Hopperstad et al. [21], a negative relation between the prestrain and the yield strength increase can be seen for Docol 600DP, cf. Figure 6. A similar relation is reported by Bleck et al. for a dual phase steel [8], as shown in Figure 8. Neither of the studies report dramatic changes. For Docol 1200M, the pre-strain dependence seem to be very weak.

The results presented above have implications for the experimental approach of this work, as well as possible structural component analysis using the framework presented in this report. Since the amount of pre-strain is relatively unimportant for the Cottrell locking phenomenon, a single pre-strain level is regarded as sufficient to study

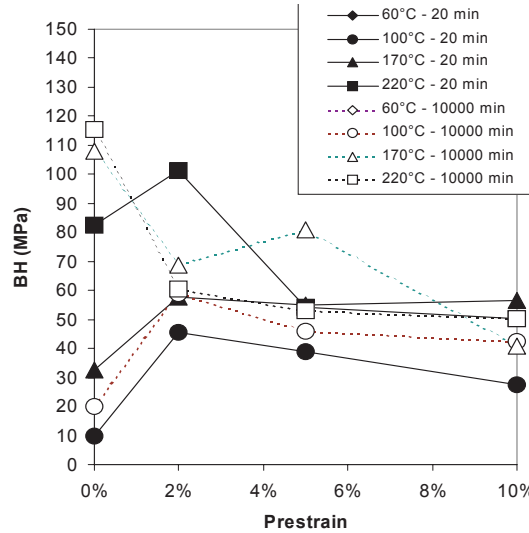


Figure 8: Evolution of  $\Delta\sigma_{BH}$  with pre-strain for a DP 600 steel, after [8]

the bake hardening effect. Furthermore, structural components can be modeled as having regions with pre-strain and regions without pre-strain. The actual levels of the pre-strain is therefore not necessary to include.

### 2.2.6 Constitutive modeling

Strain aging due to bake hardening can be modeled in two ways. A physical model strategy implies that the increase in yield stress and modified work hardening is expressed as a function of the physical mechanisms (diffusion of constituents causing Cottrell locking and precipitation). A phenomenological model, on the other hand, aim at modifying the constitutive model to account for the observed phenomena. This usually means adjusting the hardening curve by introducing additional constants that can be fitted to experimental data.

Ballarin et al. have proposed a phenomenological model consisting of an additional term in the isotropic plastic hardening function [5]. The resulting yield criterion can be expressed as

$$f = \sigma_{eq}(\sigma) - (\sigma_0 + R(p) + \sigma_{BH}) \leq 0$$

The overstress function  $\sigma_{BH}$  is expressed as a Voce term with a negative saturation value

$$\sigma_{BH} = R_{BH} + Q_{BH}(1 - e^{-\theta_{BH}/Q_{BH}(p-p_0)})$$

where  $p_0$  corresponds to the effective plastic pre-strain and  $R_{BH}$ ,  $Q_{BH} < 0$  and  $\theta_{BH}$  are constants for calibration.

The model was shown to reproduce a sharp yield point, a yield plateau due to the formation of Lüder bands and a modified hardening behavior, as observed in experiments [5]. Several studies have

since used a strain aging model on this form, for example [4] and [27] as well as the study by Hopperstad et al. on Docol 600DP and Docol 1200M [21]. This model will also be used in this thesis.

To simplify the treatment of the bake hardening addition in a generic constitutive framework, such as a library material model, the bake hardening addition can be rewritten using the previously derived Equation (4). All voce terms (work hardening and bake hardening) can then be written on the same form, namely

$$R_i(p) = Q_i \left( 1 - e^{-\frac{\theta_i}{Q_i} p^*} \right)$$

Thus, the pre-strain  $p_0$  does not need to be treated explicitly in the hardening formulation. Two options exists:

- A. Rewrite the work hardening Voce terms such that  $p^* = 0$  correspond to the pre-strained state. The actual bake hardening parameters as defined above can be used, since

$$Q_{BH} \left( 1 - e^{-\frac{\theta_{BH}}{Q_{BH}} (p^* + p_0 - p_0)} \right) = Q_{BH} \left( 1 - e^{-\frac{\theta_{BH}}{Q_{BH}} p^*} \right)$$

- B. Rewrite the bake hardening Voce term such that  $p^* = p_0$  correspond to the pre-strained state and initialize the plastic strain at this value. The bake hardening parameters are “extrapolated” such that they are valid from zero plastic strain, but the curve is never used in the extrapolated region.

Both procedures are used in this thesis and are most likely clarified by Figure 48a and 48b on page 76. They show the results of shifting the work hardening and bake hardening terms, respectively, as well as initializing the plastic strain at a defined pre-strain value.

### 2.3 CHARACTERIZATION METHODS

A standardized way of testing bake hardening response is to subject a sample to a certain amount of pre-strain (eg. 2%) representing the forming operation, and then an aging treatment at 170°C for 20 minutes (cf. standard EN10325 [1]). This treatment can be applied for different types of material tests. The ones relevant for the present work, the uniaxial and plane strain tension test, are presented in this section.

#### 2.3.1 Uniaxial tension test

The uniaxial tensile test is a standardized material test used for measuring many engineering properties of a broad range of materials. A typical specimen geometry is shown in Figure 9. One significant

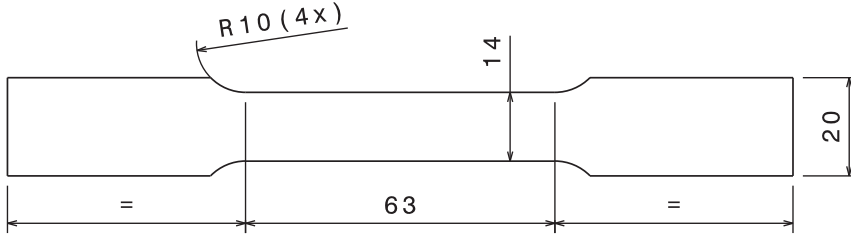


Figure 9: Example uniaxial test specimen geometry, after [27]

advantage of the test is that the measured quantities (force and elongation) is easily converted to the material response quantities (true stress and true strain). In addition, a single test gives information about modulus of elasticity, yield stress, elongation to failure and plastic hardening rate. If several tests are performed, it can also be used to characterize plastic anisotropy, if present.

The engineering stress and strain quantities, based on the initial cross section area and initial extensometer length respectively, are calculated from

$$s = \frac{F}{A_0}, \quad e = \frac{\Delta L}{L_0} \quad (6)$$

where  $\Delta L$  is the elongation of the extensometer. By assuming small elastic strains and plastic incompressibility, the following transformation can be used to calculate the corresponding true (Cauchy) stress and true (logarithmic) strain values in the plastic regime.

$$\sigma = \frac{F}{A} = s(1 + e), \quad \varepsilon = \ln\left(\frac{L}{L_0}\right) = \ln(1 + e) \quad (7)$$

However, this conversion from force-elongation to stress-strain is only valid as long as the elongation of the gauge section is *uniform*. After diffuse necking occurs, further plastic deformation only occurs within the neck. An engineering stress-strain curve will indicate a decreased stress with increasing strain, while in reality the stress is increased monotonically in the necking region while the area is decreased. This complicates measurement of the true strains. Inverse modeling through for example FE analysis is generally required for further data interpretation. For a circular specimen, a Bridgeman correction can be applied to account for the stress state, but inverse modeling can be used also in this case for improved accuracy.

According to the Considère criterion, diffuse necking occurs when the true stress and the work hardening rate are equal, viz.

$$\sigma = \frac{d\sigma}{d\varepsilon_p}$$

This can be shown to occur at the point of maximum force for a uniaxial test. Thus, a high stress level and a low work hardening

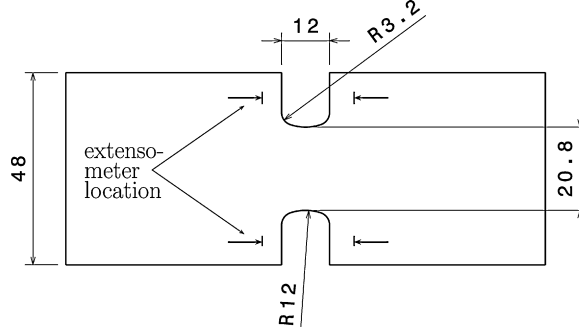


Figure 10: Typical PST specimen geometry, after [27]

rate will quickly lead to diffuse necking. As previously mentioned, this is in fact the case for bake hardened Docol 1200M in uniaxial tension [18]. Note, however, that this instability mode is specific for uniaxial tension tests. Other tests may trigger different failure modes, such as localized necking or ductile fracture.

Considering the early necking of previous tests, an inverse modeling strategy is adopted for the parameter identification in this thesis. This means that attempts will be made to compare experimental force-displacement data with corresponding data from a finite element model, and refine model parameters iteratively until a good fit is obtained. Although this is considerably more involved than a direct calibration of stress-strain data, it can prove necessary in situations where no uniform deformation takes place.

### 2.3.2 Plane strain tension test

A plane strain tensile (PST) test, also known as notched specimen tensile test, is a test where the specimen geometry is designed such that the strain in the width direction is restricted as much as possible. A typical specimen geometry is shown in Figure 10. The resulting state of strain can be summarized as

$$\boldsymbol{\varepsilon} = \begin{bmatrix} \varepsilon_{11} & 0 & 0 \\ 0 & \varepsilon_{22} \approx 0 & 0 \\ 0 & 0 & \varepsilon_{33} \end{bmatrix}$$

where, due to plastic incompressibility,  $\varepsilon_{33} \approx \varepsilon_{11}$ .

Although formability tests like MK bulge tests normally are used, PST test can be used to obtain the lowest failure strain in the forming limit diagram,  $FLD_0$ , if a sufficient degree of constraint can be obtained. Furthermore, it can be used to calibrate through-thickness shear instability criteria [24]. This will not be considered in the present work. Finally, plane strain tests give additional information about the

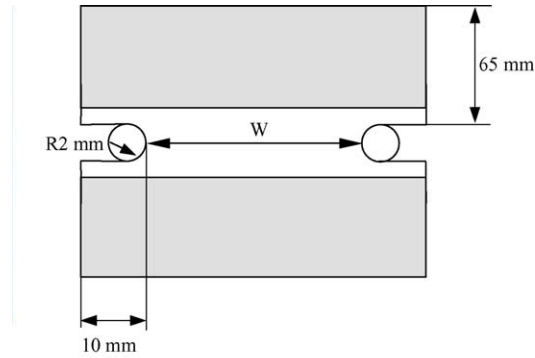


Figure 11: Alternative PST specimen geometry, after [2]

shape of the yield surface. According to the normality rule, the gradient to the yield surface determines the direction of plastic flow:

$$\dot{\epsilon}_p = \dot{\lambda} \frac{df}{d\sigma}$$

This means that if a numerical model that assumes  $J_2$  flow theory gives good representation of the PST test, one can conclude that the von Mises yield surface gives the correct gradient in plane strain. If not, a higher exponent model that predict a different stress state for the given direction of plastic flow can be evaluated.

The design of the PST specimen geometry is not as trivial as for a uniaxial tension test and can depend on the purpose of its use. A few examples from the literature serve to clarify this point, which in turn justifies the numerical study on PST geometry which was performed as part of the present work.

Larsson and Nilsson used plane strain tensile tests to find absolute values of two dynamic strain aging parameters for an austenitic stainless steel showing both SSA and DSA, as well as to determine work hardening parameters at high plastic strains [27]. The geometry shown in Figure 10 was used. Other authors have used a similar specimen geometry to *validate* a constitutive model calibration (see for example [25]). In these cases, the PST provided a strain path significantly different than uniaxial tension (cf. the FLD schematic in Figure 2), but did not necessarily represent *true* plane strain.

An et al. have proposed a methodology for PST tests where different sample widths were used to extrapolate test results into a “true” plane strain situation [2]. The geometry, which is somewhat different than the one used in the studies mentioned above, is shown in figure Figure 11. The authors went on to show how the proposed methodology can be used to measure plane strain work hardening, and also proposed a simplification that only results in a slight decrease in accuracy. The methodology has been successfully applied on a study on AA6016 aluminum by Dmitry [13], but the results of this study also

indicate that the specimen geometry proposed by [An et al.](#) may be susceptible to premature failure due to crack initiation in the notches.

As mentioned, one of the goals of this thesis is to determine the  $FLD_0$  of the considered materials. It will therefore be investigated, whether the geometry of [An et al.](#) can be adopted for the present study or if a “standard” specimen geometry is better suited.

## METHOD

---

This chapter explain the steps, procedures and calculations carried out in the course of the present work and provides definitions of relevant terminology.

### 3.1 EXPERIMENTAL STUDIES

#### 3.1.1 Uniaxial tension tests

The purpose of the uniaxial tensile tests were

- to study the deformation bands that were expected to occur for the aged material
- to calibrate the yield- and hardening parameters of the constitutive model

To obtain a bake hardened material, pre-straining is necessary, as previously discussed in [Section 2.2.5 Influence of pre-straining](#). To isolate the bake hardening effect from the pre-straining and other possible effects in the virgin material, three material states were considered: Virgin (as-rolled) material, material pre-strained to 20% of the *maximum uniform elongation* and material identically pre-strained and bake hardened at 170 °C for 20 min (according to standard EN10325 [1]).

The uniaxial tension tests will be denoted  $UT-XX-Y$ , where  $UT$  stands for uniaxial tension,  $XX$  represent the state of the material and  $Y$  is the specimen number.  $XX$  take the values  $V$  for Virgin (as-rolled) material,  $WH$  for 20% pre-strained (work hardened) material and  $WH+BH$  for 20% pre-strained and bake hardened material. Since only one level of pre-strain and one pre-strained and bake hardened condition is considered, the notation should be unambiguous.

The nominal test specimen geometry is shown in [Figure 12](#). For each of the two materials, six specimens were machined from the virgin plate. All raw material was taken from the same production

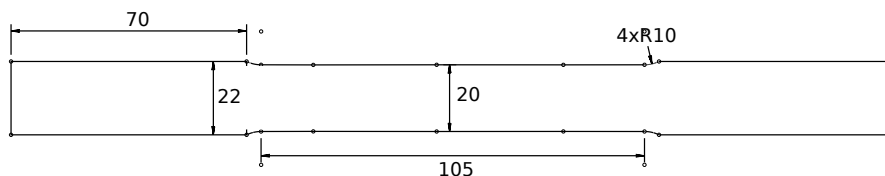


Figure 12: Uniaxial tension test specimen geometry

batch. Four of the specimens were then subjected a pre-straining corresponding to 20% of the maximum uniform elongation. Two of these pre-strained specimens were then subjected to artificial aging at 170 °C for 20 min. Thus, two repetitions of the same test was carried out for each material state.

The actual width and thickness of the tested specimens were measured at three cross sections along the gauge region. The results, along with the absolute value of the pre-straining, are given in [Table A.2](#) in [Appendix A](#). The geometric deviations were very small, but can be important for the location of the diffuse neck.

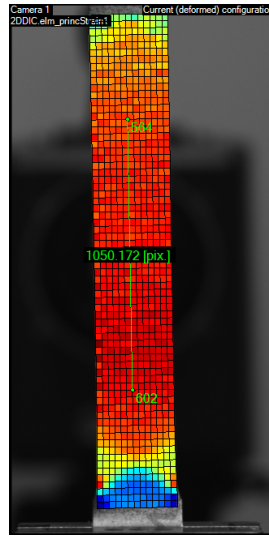


Figure 13: Example of node selection for the virtual extensometer

Two field measurement techniques, Digital Image Correlation (DIC) and Digital Image Thermography (DIT), were used to gather data for analysis of the deformation bands. The optical and thermographic cameras were placed in front of and behind the testing machine, respectively, facing each other. A FLIR SC7000 thermographic camera and a Prosilica optical camera with a 50 mm f/1.4 Nikon lens was used.

To enable field measurement, the specimens were painted matte black on the side facing the DIT camera and were given a very fine grained speckle pattern on the side facing the DIC camera by means of white paint followed by black stains. The paint was applied just before testing, to avoid cracking of the paint coat under straining. The specimens were then tested in an Instron servoelectric testing machine with a gripping capacity of 50 kN until failure. Force and displacement of the machine crosshead was measured in addition to DIC and DIT data. The testing speed was 6 mm/min in accordance with previous tests [21], corresponding to a strain rate of about  $1 \times 10^{-3}$ /s. One specimen was tested at 1.8 mm/min, but it was not discarded from the data set since the strain rate sensitivity of the ma-

material was assumed to be low. The frame rate of the image acquisition was adjusted according to the expected test length in order to get a reasonable amount of images for the DIC post-processing (about 200 frames). Details are given in Table A.1 in Appendix A.

An in-house DIC software developed at NTNU [15] was used for the image correlation and strain field calculations. Since the strain field in the entire specimen was calculated from the DIC data, no clip-on extensometer was used. Instead, the distance between two nodes in the DIC mesh was tracked over time, creating a virtual extensometer. Averaged value over multiple DIC nodes were used only in one case, namely in the data extraction and calculation of the plastic strain in the width- and thickness directions for Docol 1200M. In all other cases, the noise in the data was low and the accuracy was judged to be sufficient. The element size was chosen close to the suggested 25 x 25 pixels, but scaled to cover the entire specimen.

The nodes for the virtual extensometer were chosen sufficiently far from the ends of the specimen to avoid end effects, but a single consistent gauge length was not used throughout. Node numbering was not consistent between each DIC analysis, which made the process of finding corresponding nodes in each mesh tedious. The longitudinal gauge lengths used were in the range 60-98 mm. Details are given in Table A.1 in Appendix A.

Figure 13 show an example of a virtual extensometer node selection. For the actual analysis, both longitudinal and transverse extensometer was used, such that the plastic anisotropy could be checked. For an isotropic material, the plastic strain in the width and thickness direction of a uniaxial tension test should be equal due to plastic incompressibility. In case of anisotropy, the R-ratio given by

$$R = \frac{\varepsilon_w^p}{\varepsilon_t^p}$$

can be used to characterize the degree of anisotropy. It can be determined by a linear regression in an  $\varepsilon_w^p$ - $\varepsilon_t^p$  diagram. For the materials considered in this thesis the anisotropy was expected to be low, such that inspection of such a graph would be sufficient to verify the validity of an isotropic yield function.

To enable a straightforward comparison of all gathered data, the images from the thermographic camera were imported in the DIC software. Temporal and spatial scaling was used to align these images with the frames captured by the DIC camera. The temperature data was then interpolated to the nodes in the DIC mesh such that it could be treated in the same way as the strains calculated from DIC. To simplify the identification of moving deformation bands, the time derivative of the temperature and the strain fields were calculated by applying a moving average smoothing filter of the nodal data, followed by a central difference rate-of-change calculation in time.

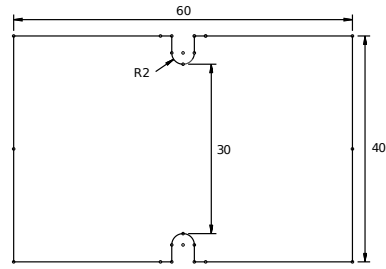


Figure 14: Plane strain tension test specimen geometry

The force and extensometer data were processed with the test data management tool *MatPrePost* developed at SIMLab/SINTEF. The processing involved calculating engineering properties from measured initial geometry, as well as calculating true stress and true plastic strain values based on the transformations presented in [Section 2.3.1](#). The plastic strains were computed using a combination of the Young's modulus found from linear regression of the engineering stress-strain curve and a prescribed value of 210 GPa.

### 3.1.2 Plane strain tension test

The purpose of the plane strain tensile tests were

- to estimate the point of lowest formability,  $FLD_0$ , before and after baking
- to validate the ability of the constitutive model to correctly represent strength and failure in a different region of the yield locus than the one for which it was calibrated

As for the uniaxial tension tests, three states of each material was chosen for plane strain testing: Virgin, pre-strained and pre-strained and bake hardened. However, all pre-strained samples were accidentally baked meaning that only as-rolled and bake hardened material was tested. Two repetitions of each test was chosen, since a low scatter in properties within the batch was anticipated. The tests will be denoted *PST-XX-Y*, where *XX* denote the material state and *Y* is the specimen number.

Six rectangular coupons of each material, with the long side parallel to the rolling direction, was cut out from a plate taken from the same batch as the uniaxial tension specimens. Four of the coupons were pre-strained to the same amount of plastic strain as the uniaxial tension test samples. All four samples were then baked at 170 °C for 20 min. The pre-straining was conducted in a low constraint mode, i. e. close to uniaxial tension. Finally, the geometry shown in [Figure 14](#) was machined from the plates using electric discharge machining.

The Docol 600DP samples were tested in an Instron servoelectric testing machine with clamps capable of 50 kN. Due to alignment is-

sues and high strength levels, the Docol 1200M samples were tested in an Instron servohydraulic testing machine capable of independent clamping. The capacity of the machine was 100 kN. All samples were tested with a crosshead speed of 1 mm/min until failure, corresponding roughly to a strain rate of  $1 \times 10^{-3}$ /s.

Optical and thermographic cameras were used also for these tests, with a similar test setup as previously. The test setup, with the two cameras positioned on each side of the testing machine, is shown in [Figure 15](#).

In the DIC analysis, the element size was set to the number of pixels corresponding to 0.5 mm (just over 20 pixels). Virtual extensometers were used to extract both the nominal displacement of the crosshead and the local strain in the necking region. For the former virtual extensometer, a gauge length of 8 mm was used. For the local strains, a gauge length of 1 mm was used. The reason for this choice is that the width of the localized neck is on the same order of magnitude as the sheet thickness [25]. Hence, the local strain at maximum force measured with this gauge length should be a good estimate of the true necking strain in plane strain condition. Nodes were chosen consistently across all tests, aligned with the vertical centerline of the sample and symmetric about the horizontal centerline. [Figure 16](#) show an example of the node selection close to the notch, halfway towards the center of the specimen and in the center of the specimen. Finally, the continuous major and minor principal strains were interpolated along the horizontal centerline of the specimen and exported.

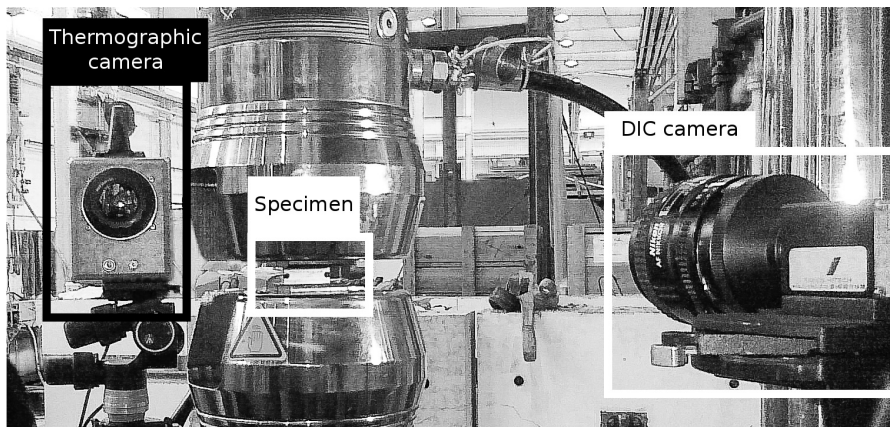


Figure 15: Plane strain tension test setup

### 3.2 MODELING APPROACH

The modeling approach taken in this thesis is based on the theory presented in [Chapter 2](#) and the available features of the SIMLab Metal Model, following the work by [Hopperstad et al.](#). The general-purpose FE software LS-DYNA was used in all numerical simulations, and

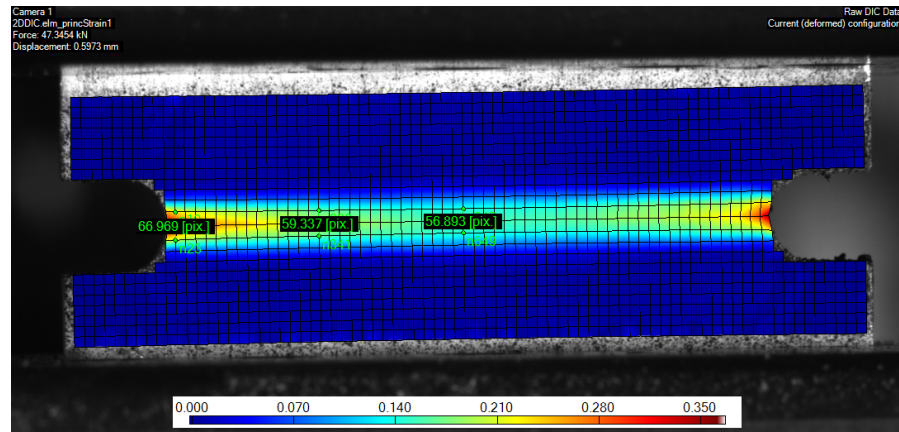


Figure 16: Local strain gauge node selection

the Metal Model was accessed as a user defined material model. For the constitutive model,  $J_2$  flow theory was assumed. A two component Voce rule was used to describe the hardening curve of the parent material, while the bake hardening was treated through an additional (third) Voce term. Initially, all hardening terms was assumed isotropic, but partly kinematic work hardening was used to enhance the description of Docol 600DP. Strain rate and temperature effects are neglected, as they are assumed to have little influence on the results within the considered ranges of temperature and strain rate.

At the time the present work was carried out, the SIMLab Metal Model was developed for explicit analysis only. Therefore, explicit time integration has been favored when possible. Time scaling has been employed, i. e. the applied velocity has been increased by about  $10^3$  while retaining the true density. The ratio of kinetic energy to internal energy has been carefully checked for all simulations to ensure that the loading conditions remained quasi-static ( $E_{kin} \ll E_{int}$ ).

Shell elements have been used throughout this thesis, both since the considered components are thin-walled and due to computational cost considerations. Low order reduced integration elements with an appropriate hourglass inhibitor has been used unless otherwise stated, also owing to reduced computational cost. To account for area reduction due to thickness stretch, the shell thickness update option has been used.

A characteristic element size of 0.5 mm was determined by parameter studies to give a good post-necking force prediction for uniaxial tension tests of Docol 600DP (see part on inverse modeling in the next section). This element size has been used throughout the present work, unless otherwise stated, to eliminate uncertainties related to mesh size.

### 3.3 PARAMETER IDENTIFICATION PROCEDURE

The parameters for the yield function and work hardening curve has been found through a combination of direct fitting of uniaxial tension test data up to diffuse necking and inverse modeling of the uniaxial tension specimen. Through inverse modeling, the data for large(r) plastic strains that occur after diffuse necking can be taken into account in the parameter identification. This approach is motivated by the fact that diffuse necking occurs relatively early in the uniaxial tension tests on Docol 1200M, while for Docol 600DP, sufficient uniform straining takes place. In particular, the parameters that account for the bake hardening effect in Docol 1200M were refined through inverse modeling.

Data from the present uniaxial tests, as well as from previously reported ones, has been used. The results for each case has been applied to the plane strain tension and plane strain bending simulations, respectively.

#### 3.3.1 Curve fitting

The two component Voce law of Equation (3) was calibrated from the uniaxial tensile tests on virgin material through a least-square curve fitting procedure in MatPrePost. To obtain parameters that correspond to pre-strained material, the calibrated curve was shifted as given by Equation (4). The amount of shifting was determined by the actual mean pre-strain level of the uniaxial tension specimen. For the pre-strained and bake hardened specimen, the bake hardening addition to the constitutive model was isolated by subtracting the predicted work hardening stress level from the actual(measured) total stress. The three bake hardening parameters ( $R_{BH}$ ,  $Q_{BH}$ ,  $C_{BH}$ ) were then calibrated to correspond to the overstress ( $\Delta\sigma_{BH}(p)$ ).

Due to discrepancies in the calculated material response between the present experimental work and previously reported data (cf. [Section 4.1.1](#)), previously reported parameter identifications has also been considered in this thesis. The parameters identified from the previous tests on virgin Docol 600DP has been shown to give good description of the material response when compared to results from experimental plane strain bending tests [26]. In the present study, the bending tests were reconsidered. Therefore, to avoid any unnecessary sources of error, the old uniaxial tension tests were considered to be more relevant to the plane strain bending tests than the new uniaxial tension tests.

The previously reported parameters for the virgin and bake hardened material states were adopted as presented in [21], but parameters for the pre-strained material has been calculated using Equa-

tion (4). In addition, the bake hardening parameters for Docol 600DP has been shifted “backwards”, as explained further in [Section 3.4.3](#).

### 3.3.2 Inverse modeling

In the parameter identification process for Docol 1200M described above, it was observed that the work hardening curve described by the two Voce components saturates very quickly. Although correct for small plastic strains, this may not reflect the behavior at large plastic strains. To try to improve the previously reported parameter identification of Docol 1200M, the extended numerical model of Equation (5) was considered. The parameter corresponding to the stress at 100% strain,  $\sigma_{100}$ , can be used independently of the Voce parameters to calibrate the stress at very large plastic strains.

For the inverse modeling, finite element models of the relevant specimens were created and run with the initial parameters given in [21]. The virgin Docol 600DP specimens were taken as a reference case and a sensitivity study was performed to ensure that the model was able to describe a case for which the parameters are well calibrated. Time integration method and mesh sensitivity was considered. The final mesh of two of the analysis models used in the inverse modeling are shown in [Figure 17](#). To extract the “extensometer” displacement of the analysis models, nodes that corresponded to the location of the extensometer in the experiment were used. An LS-DYNA library material model (\*MAT\_103) was used in all inverse modeling simulations, since implicit analysis was not available in the SIMLab Metal Model when these simulations were carried out. The underlying theory is however the same (in fact, the LS-DYNA material is based upon work by some of the authors of the SIMLab Metal Model).

Once the numerical model was able to describe the post-necking behavior of Docol 600DP, the simulation model was run with the initial parameters of Docol 1200M. Attempts were then made to improve the correspondence in force-displacement behavior after necking by adjusting  $\sigma_{100}$ . Similarly, the model for the bake hardened specimens were run with the initial bake hardening parameters. These parameters were then adjusted iteratively to improve correspondence in force-displacement behavior after necking. The implicit-explicit switching feature of LS-DYNA was used in order to overcome the highly nonlinear dislocation unpinning at incipient yielding by explicit time integration. The formulation was then switched to implicit time integration to correctly follow the post-necking equilibrium path. The inverse modeling study was performed for the specimens used in the previously reported study on bake hardening. Force-displacement recordings from the uniaxial tension tests were kindly provided by [Hopperstad et al. \[21\]](#).

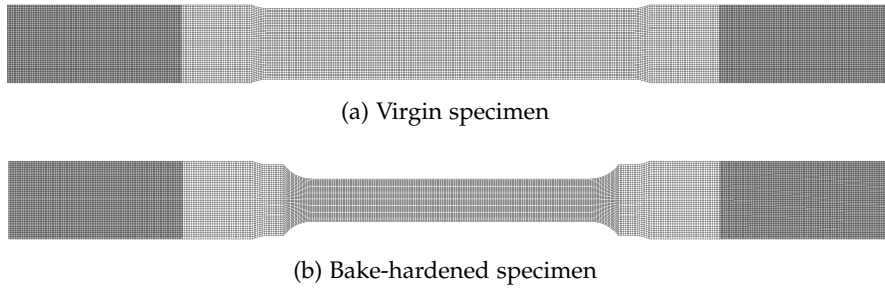


Figure 17: FEM models used for inverse modeling of the uniaxial tensile tests in previous work [21]; Gray parts modeled as rigid

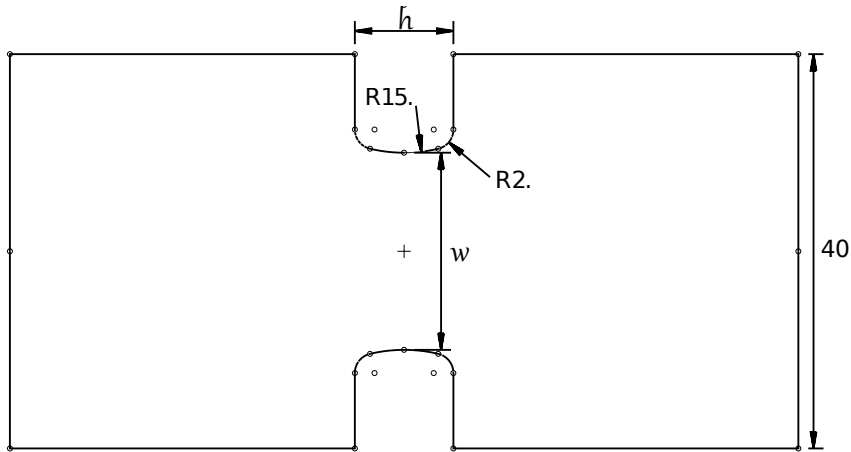


Figure 18: Reference geometry for the plane strain tensile specimen

### 3.4 NUMERICAL SIMULATIONS

#### 3.4.1 PST geometry

As previously discussed in [Section 2.3.2](#), the geometry of a plane strain tensile (PST) specimen can be varied to some extent depending on the purpose of the study. In the present work, the main purpose of the plane strain testing was to study how bake hardening affects the lower limit of structural deformability,  $FLD_0$ . It was therefore judged important to verify that the PST specimen geometry achieve a high degree of constraint. Furthermore, the maximum specimen width was limited by the width of the available clamping grips. It was investigated whether a sufficient constraint can be achieved with a relatively narrow specimen width (compared to the one used by [An et al.](#)). Limiting the width of the specimen was also beneficial for the force needed for pre-straining, due to the high strength of the materials.

Several finite element models were set up for a geometry comparison. Starting from the reference geometry depicted in [Figure 18](#), the two parameters  $w$  and  $h$  were varied in four and two steps, respec-

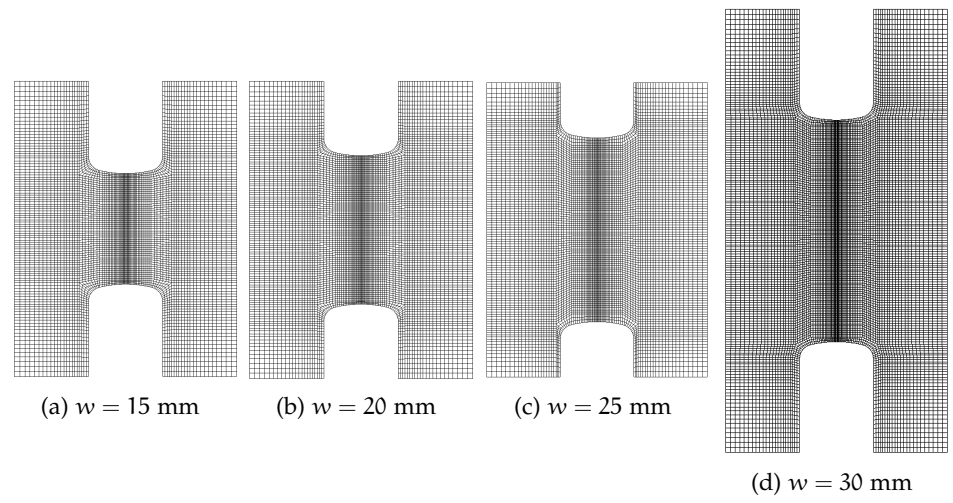


Figure 19: Mirrored meshes of the PST geometry variation – changes in notch width; Corresponding results shown in [Figure 51a](#)

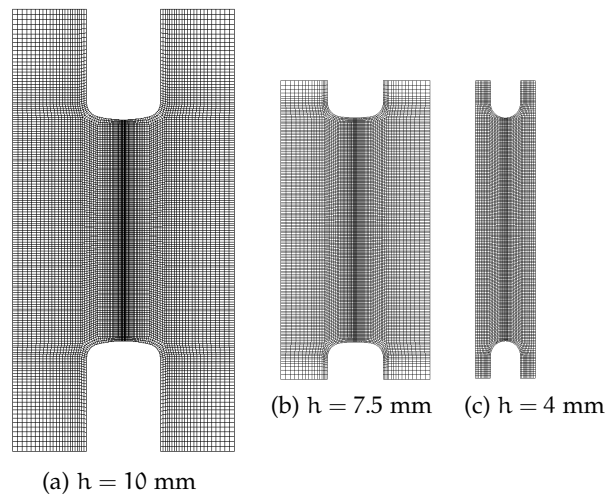


Figure 20: Mirrored meshes of the PST geometry variation – changes in notch height; Corresponding results shown in [Figure 51b](#)

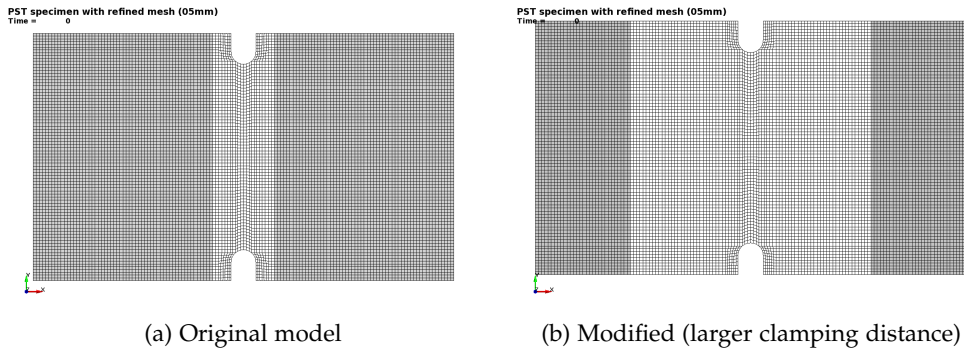


Figure 21: Finite element models of plane strain tension test; Gray parts modeled as rigid

tively. The outer width of the specimen was set to 40 mm in all but one case. One extremity of the variations correspond to a narrow version of the “standard” PST geometry, while the other extremity correspond to a geometry adopted from [2], i. e. with a sharp notch and a short distance between the clamping and the notch. One quarter of the specimen was modeled and the hardening parameters for the material model were adopted from a previous calibration of Docol 600DP in [21].

The mirrored meshes of all tested geometries are shown in Figure 19 – 20. The characteristic element size in the center of the specimen was 0.2 mm. The shell thickness stretch option was used, but non-local treatment of history variables were not used. Hence, the data after (through-thickness) localized necking are inaccurate.

### 3.4.2 Plane strain tension test

The plane strain tension test was used to check the validity of the constitutive model that describe the material behavior. The test was designed to be influenced as little as possible by geometry and therefore closely represent the material response in plane strain. If the constitutive model is able to predict hardening behavior and tensile strength (failure point) of the test, one can conclude that the yield surface and hardening rule is correctly described and is likely to give good predictions also in other load cases.

The mesh of the FE models used for the validation simulation is shown in Figure 21. Initially, only the model in 21a was considered. However, it was later found to be unclear whether the portion of the specimen inserted into the grips were homogeneously clamped during the experimental tests. To investigate the sensitivity to the clamping distance, the model shown in Figure 21b was run with parameters for virgin Docol 600DP calibrated from the uniaxial tensile tests of the present work. In this model, the clamping distance was increased to

approximately the length where clear clamping markings could be seen on the specimens after testing.

The FE models followed the general layout described in [Section 3.2](#). A simulation time of 30 ms was used initially and nodes with identical location as the DIC nodes from experiments were used to calculate the nominal displacement. The work hardening curves calibrated from the uniaxial tensile tests of the present work were used.

Due to the large time scaling implied by the short simulation time, numerical instabilities caused problems with the simulations of Docol 1200M samples with increased clamping distance. Although kinetic energy was low compared to internal energy, the instabilities were most likely caused by dynamic effects. Attempts were made to increase simulation time, but due to the small critical time step imposed by the mesh size this approach quickly led to very long computation time (>60 min on multi-cpu) and possible loss of accuracy. Therefore, the SIMLab Metal Model was abandoned and the LS-DYNA library material model \*MAT\_103 was used. Implicit-explicit switching, similar to the inverse modeling procedure, was used to overcome the material nonlinearities while at the same time reducing computational cost. The longest computation time with this approach was on par with fully explicit analyses of the original model.

Finally, a novel feature of the in-house DIC code by [Fagerholt](#) was used to calculate cross-sectional forces directly from strains measured by DIC. The DIC mesh is used as a finite element discretization of the specimen and the element strains calculated by image correlation is fed directly to the SIMLab Metal Model constitutive driver. Using the calibrated constitutive parameters, the driver returns stresses which are integrated over an arbitrary cross section of the specimen, provided that the entire cross section is covered with elements. The cross section force can then be compared to experimental measurement. The feature provides an excellent tool in this case, since it eliminates the need to calculate strains that already are known from the experiment. The DIC data were filtered using a moving average in time and a Gauss filter in space before input to the constitutive model.

### 3.4.3 *Plane strain bending test*

The previous experimental programme carried out at SIMLab did, as previously mentioned, include plane strain bending tests of the steels considered in this thesis. Data from these tests, as well as a numerical model of the test, has kindly been made available by the authors [26]. In the present work, the aim is to use this experimental data to further verify the ability of the SIMLab Metal Model to represent the bake hardening effect through the adopted modeling concept (according to [Ballarin et al.](#)).

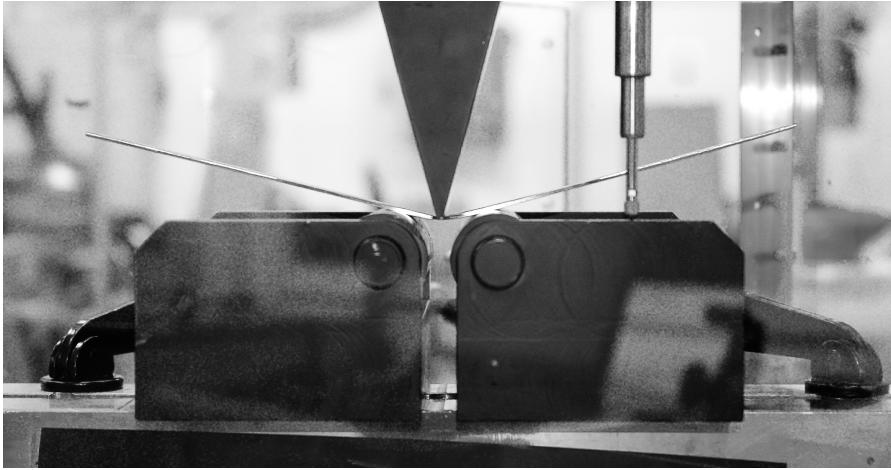


Figure 22: Test setup of the plane strain bending test, after [26]

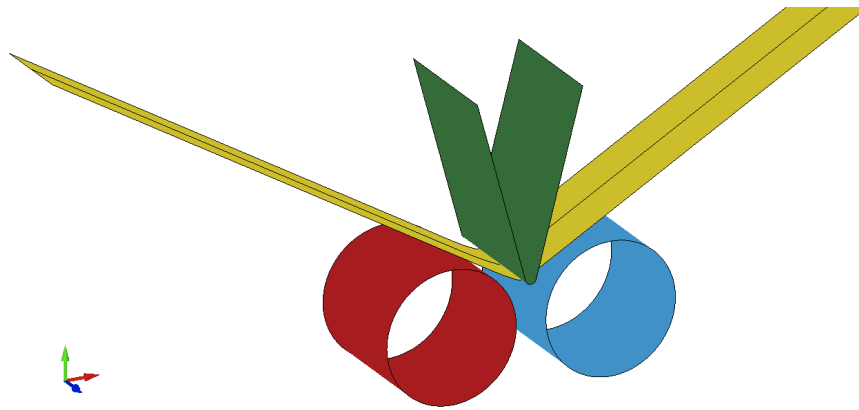


Figure 23: Analysis model of the plane strain bending test;  
Test specimen, rigid punch and rigid rollers shown

The test setup for the plane strain bending tests are shown in [Figure 22](#). This type of test is commonly denoted a Daimler-Chrysler bending test and consists of a strip specimen supported by rollers and deformed by a punch. The samples were tested in virgin (denoted V) and pre-strained and bake hardened (denoted WH+BH) condition [26]. Two pre-strain levels were considered: A pre-strain corresponding to 20% of the strain at diffuse necking in uniaxial tension, and a pre-strain corresponding to 60% of the strain at diffuse necking. Tests of samples that had been subjected to baking without pre-strain were also performed, but these are not considered in the present work.

The numerical model is shown in [Figure 23](#), and consists of support rollers and punch modeled as rigid shell elements and a sample specimen modeled with fully integrated shell elements (type 16) with 9 integration points through the thickness and a characteristic element size of 0.5 mm in the deformation zone. The model was set up for implicit analysis.

At the time the present work was carried out, the latest version of the SIMLab Metal Model lacked a consistent tangent stiffness operator. Therefore the numerical model needed to be converted from implicit to explicit time integration. To avoid dynamic effects from the parts of the specimen protruding beyond the rollers, all elements not involved in roller contact were eliminated from the model. Time scaling was used, such that the rigid punch completed its motion in 30 ms. A smooth velocity increase was used. Furthermore, the contact type was changed and attempts to use reduced integration (ELFORM=2) were made.

To model the prestrain, different approaches were chosen for the two materials. For Docol 1200M, the shifted hardening curve discussed in [Section 3.3](#) were used in the simulations of the pre-strained and bake hardened bending specimen. This is an effective solution if the work hardening can be assumed isotropic such that no distinction need to be made between the upper and lower fibers in the plane strain bending test.

For Docol 600DP, kinematic hardening was expected to have a significant impact on the plane strain bending results due to the imposed pre-strain. To properly account for this, the numerical model had to take into account the different hardening behaviors of the upper and lower fibers. As this information is stored in the history variables of the numerical model, an approach were chosen where history variables from a pre-strained element is mapped onto the plane strain bending specimen prior to simulation.

To perform the pre-strain, a separate analysis model consisting of a single simply supported shell element (identical to the ones used in the bending simulation) was set up. This element was loaded by a prescribed motion and unloaded to zero stress such that a plastic strain identical to the specimen pre-strain was obtained. All history variables pertinent to the pre-straining was then written to file through the \*INTERFACE\_SPRINGBACK card. The SIMLab Metal Model was used, with hardening parameters as calibrated for the virgin material. In one case, completely isotropic hardening was assumed. In a second case, the voce rule with the highest initial slope was assumed to be entirely kinematic (cf. discussion in [Section 2.1.2](#)). This second pre-straining case will henceforth be denoted *kinematic work hardening (WH)*.

To verify the that the pre-straining approach worked correctly, a cyclic tension-compression test of the single element was performed.

For the plane strain bending simulation including pre-strain, the history variables from the single element files were mapped onto the specimen prior to simulation through an \*INITIAL\_STRESS\_SHELL card. Identical material cards as the ones used for the pre-straining were used. In case of the pre-strained and baked material, the parameters ( $R_{BH}$ ,  $Q_{BH}$ ,  $C_{BH}$ ) calibrated from uniaxial tensile tests were

shifted according to Equation (4) and included in the material card as isotropic Voce parameters. This means that the simulations of pre-stained and bake hardened Docol 600DP includes isotropic work hardening plus isotropic bake hardening in one case and partly kinematic work hardening plus isotropic bake hardening in the other case. In other words, no kinematic bake hardening is considered, and only part of the work hardening is assumed kinematic.

To properly compare the results of the bending simulations with experimental data, the reaction forces given by the numerical and experimental tests were recast as a fictive engineering stress. By considering the elastic stress in a specimen subjected to three point bending, the maximum stress (which occurs in the outer fibers of the specimen) can be calculated as

$$\sigma_{\max} = \frac{M_{\max}}{I} z_{\max} = \frac{FL}{4 \frac{wt^3}{12}} \frac{t}{2} = \frac{3FL}{2wt^2}$$

where  $L$  is the length between the initial contact points of the roller supports,  $w$  and  $t$  are the width and thickness of the specimen, respectively, and  $F$  is the force exerted by the punch. This formula is obviously only valid up to the point of first yielding, after which the stress is no longer linearly varying over the thickness. The scaling does however, to some extent, remove the dependency on the test geometry, such as the roller distance and the specimen thickness. Thus, the fictive stress is more representative of the actual material loading than the force alone.

During post-processing of the numerical bending simulations, a low pass SAE filter was used to filter the reaction force. This is common practice for explicit dynamic simulations [16] and is in this case used to remove oscillations that are due to the contact formulation. By using a corresponding implicit analysis, it was verified that the force obtained from explicit analysis oscillates around the equilibrium curve and that the filtering extracts the desired information. A filtering cutoff frequency of 600 Hz was selected. Indeed, a smoother but much more expensive contact formulation (using the MORTAR option in LS-DYNA) could have been used, but the filtering was judged to not reduce the accuracy of the simulations significantly.



## RESULTS AND ANALYSIS

---

This chapter presents and discusses the results of the work outlined in the previous chapter. To enhance text readability, all figures have been placed separately starting on [page 57](#). PDF readers are advised to use the hyperlinks to the figures given in the text and the (*back*) links in the figure legends to navigate the document.

### 4.1 EXPERIMENTAL STUDIES

#### 4.1.1 *Uniaxial tensile tests*

The results for the uniaxial test series related to the present work are presented in [Figure 26 – 40](#). In [Figure 26](#), stress versus plastic strain curves are shown for the virgin, pre-strained and pre-strained and baked material. Corresponding curves for 1200M are shown in [Figure 27](#). The results from the DIT measurements are mainly presented as spatiotemporal graphs in [Figure 35 – 38](#). Some further results and comparison with DIC measurements are presented in [Figure 39, 40, 30](#) and [31](#). The fractured specimens from the first test series are shown in [Figure 24](#).

For 600DP, all specimens undergo quite large uniform deformation until diffuse necking occurs (cf. [Figure 24](#)). The work hardening behavior for the pre-strained material is virtually identical to that of the virgin material, as expected. The material show a significant bake hardening effect with a clear offset from the hardening curve of the virgin material. The shape of the hardening curve after baking seem to be very similar to that of the virgin material up to the point of diffuse necking, but a slight tendency for fading with plastic strain, as reported in [\[21\]](#), can be seen.

For 1200M, relatively small plastic strains are observed even for the virgin material until diffuse necking occurs. The virgin and pre-strained curves differ significantly, which indicates that some strain aging has occurred in the pre-strained material. Please see further discussion below. The artificially aged specimens show distinct bake hardening, with a sharp yield point and a very short elongation until necking and ultimate failure, as previously reported.

[Figure 28](#) and [29](#) compare data from the present experimental work with data presented in [\[21\]](#). Although the test conditions were similar and the material were taken from the same batch, distinct differences can be seen. The tests conducted in the present work show consistently lower flow stresses, on the order of 5-10 %. On the other hand,

the offset due to the bake hardening seem to be more or less constant. Whether scatter on this order of magnitude can be expected *within* a batch remains to be confirmed. The difference could possibly be attributed to property variations across the width of the batch plate since the position of the specimens within the batch are unknown.

In the DIT results for Docol 600DP shown in [Figure 36](#), no Lüder's bands were observed in any of the tests. This indicates that no dislocation unpinning takes place during deformation of the bake hardened specimen, which supports the conclusion of [Hopperstad et al. \[21\]](#): *The bake hardening effect of Docol 600DP seem to be dominated by formation of precipitates* (i. e. not by dislocation pinning). Another explanation of the smoothly initiated plastic flow, presented by [Bleck et al.](#), is that local residual stresses at phase boundaries initiate a smooth yielding (cf. [Section 2.2.3](#)).

For Docol 1200M, smooth and even yielding along the specimen length was expected for the virgin and pre-strained material states due to the smooth and initially high work hardening of the parent material as revealed by the stress-strain curve. However, as shown by the spatiotemporal graphs ([Figure 38a](#) and [38b](#)) and further detailed in time series in [Figure 39](#) and [40](#), the strain seemed to localize in regions of inclined bands after just a small amount of plastic strain.

In case of the virgin material, no moving deformation bands were observed, but the strain seem to have developed progressively in inclined regions where the plastic flow was initiated. The zone of temperature increase (dissipation zone) was initially large, but shrank towards the region of diffuse necking as the plastic strain increased. Since the plastic strain was quite non-uniform over the gauge length of the specimen, the stress-strain curve calculated from extensometer displacements does not give an accurate description of the stress and strain experienced by the local material elements. By averaging over a longer distance than the actual length of deformation, the calculated plastic strain will be smaller than the true local value. This leads to a Voce calibration that saturate too early. The severity of the problem is of course related to how local the deformation is compared to the averaging length. It is difficult to extract a good measure of the plastic strain in any other way than through an extensometer, since only the cross sectional force is known (and not the stresses corresponding to the strains given by DIC). The parameter identification in the present work is therefore done according to common practice.

By contrast to the virgin material, the pre-strained material showed clear deformation banding just after the plastic flow had been initialized. The strains were too small to be measured accurately with DIC, but the thermographic images revealed how the region of heat production (dissipation) was initiated at the lower end of the specimen and traveled upwards somewhat irregularly before stabilizing at the point where the diffuse necking occurred. The non-uniform

initialization of plastic flow and the discrepancy between the virgin and pre-strained material indicate that some aging process has occurred between pre-straining and testing of the specimen. The inherent problem of using an average extensometer to calculate the stress-strain curve is present also in this case. Comparison of the virgin and pre-strained material response is somewhat complicated by the fact that the virtual extensometer gauge lengths were not identical (cf. Table A.1)

Similar stress-strain curves as the ones shown in Figure 27 are reported by Hopperstad et al., who noted that necking occurred directly after yielding for all work hardened material [20], also those that were not artificially aged. The field measurements in the present study show that the reason for the work hardened material to deviate from the virgin is that room temperature strain aging has taken place. Presumably, the mechanism is dislocation pinning that occur for aging times longer than 20 min, as no room temperature aging was reported for this aging time in [21].

The bake hardened Docol 1200M showed no apparent deformation bands when observing the entire DIC field as presented in Figure 38c. A closer inspection of the necking region did however reveal a slight band tendency. A time series of strain rate and temperature change close to the lower end of the specimen is shown in Figure 30. At incipient yielding, the strain rate and dissipation localized immediately in an inclined band at the lower end of the specimen gauge region. Before final rupture, however, the strain rate was diffused slightly and the region of dissipation split in two parts moving in opposite direction. Finally, the strain rate and dissipation intensified once again and localized necking occurred.

In Figure 31, a similar behavior is shown as a time series with frames taken before maximum stress was reached. After initialization of plastic flow, the strain rate and region of dissipation is split in two parts, followed by localized necking.

The observed events could represent the transient unpinning of dislocations that were expected to take place in the bake hardened material. The unpinning was however immediately followed by localized necking, rather than the expected propagation of the unpinning front in form of a Lüders band. This indicates that after baking, the conditions of localized necking are fulfilled already at incipient yielding. Apparently, the stress level is raised so much by the Cottrell locking that once the atmospheres are unpinned, there is no possibility for work hardening and possible precipitate strengthening to support the load. The only option is that a localized neck appear in the region that has been unpinned, as seen in the experiments. By this explanation, a similar behavior should be seen in the plane strain tension test.

Figure 33 show a thermographic image of a Docol 1200M bake hardened specimen at incipient yielding. The dislocation unpinning

is transient, almost momentary. The lower specimen temperature compared to the room temperature is explained by cooldown during elastic expansion of the atom lattice.

From the length- and width extensometers taken from DIC data, the plastic strains in the width and thickness directions were calculated under the assumption of plastic incompressibility. Figure 34 show these quantities plotted for all tensile tests of Docol 600DP and 1200M, respectively. The data contain some noise due to the small strains in the width direction, but the trend is clearly that the slope is very close to unity for Docol 600DP and slightly less than unity for Docol 1200M. The R-ratios have not been calculated explicitly in this work, but have previously been reported to be 1.04 for Docol 600DP and 0.63 for Docol 1200M in the rolling direction [18]. Although this indicate plastic anisotropy for Docol 1200M, it is not believed to be of primary importance for this thesis to account for the anisotropy in the simulations.

#### 4.1.2 Plane strain tension tests

The results of the plane strain tension tests are presented in Figure 41 – 47. The engineering stress versus normalized displacement curves for the two materials are shown in Figure 41a and 41b, respectively. The nominal displacements measured by DIC has been shifted such that the elastic stiffness closely resembles the numerical tests to simplify comparison. These figures also include curves of the corresponding numerical analyses of the tests. Figure 41a show results from simulations using the original geometry, Figure 42a correspond to the model with longer clamping distance and Figure 43a correspond to the DIC analysis. Corresponding simulations for Docol 1200M are shown in Figure 41b, 42b and 43b, respectively. Figure 44a and 44b show the major and minor strain paths traveled by the local virtual extensometers during the test. The strains at maximum force are marked by a red dot. Please note that the logarithmic strain is used, calculated from the engineering strain values through the transformation

$$\varepsilon_{\alpha}^{L_0} = \ln \left( 1 + \frac{\Delta L}{L_0} \right) \quad \alpha = 1, 2$$

where the initial length,  $L_0$ , of 1 mm was selected.

Figure 41a show that the stress level and hardening behavior of Docol 600DP is quite different between the virgin and the pre-strained and bake hardened test specimens. The maximum nominal displacement is however very similar in all tests. Likewise, as shown in Figure 44a, the local strains at maximum force is very similar for the two material states when the pre-straining is included. The reason for these results are obvious from Figure 45a and 45b; the specimens do not fail due to localized necking in the plane strain region of the

specimen, but due to crack propagation starting from the notches. Hence, the strains at maximum force do not correspond to the necking strain. By comparison, the strains are also much too small; the data sheet report an  $FLD_0$  of approximately 0.2 [mm/mm] [31].

The stress-nominal displacement curves from the simulations of the original model of the plane strain tension test show poor correspondence with the experimental data (cf. Figure 41a). While the yield point is acceptably predicted for the virgin material, the stress is grossly over-predicted at larger displacements. Qualitatively, the shape of the hardening curve is also unexpected. The shape and height of the curve as predicted by simulations did however turn out to be highly dependent on the clamping distance in the numerical model. As shown in Figure 42a, much better correspondence is seen between the modified numerical model (cf. Figure 21) and experimental data for the virgin condition. This indicate that the clamping force was applied primarily to the far end of the specimen, rather than the entire area enclosed by the grips. The actual imposed clamping distance remain uncertain and seem to have affected the results but from the consistency of the experimental test results there is no reason to believe that the clamping distance varied between the tests. Comparison between the two material states should therefore not be problematic.

The cross sectional force as calculated by coupling the DIC code to the SIMLab Metal Model is shown in Figure 43a. By contrast to the finite element models, these analyses utilize the experimentally measured strains to calculate stresses through the constitutive model. Hence, the uncertainty in the clamping distance does not affect the accuracy of the force calculation, which in turn simplifies evaluation of the constitutive model.

From the DIC calculations, a slight overprediction of the virgin material curve is seen. It can be attributed to the assumption of von Mises plasticity. A higher exponent model may have been even more accurate in plane strain conditions, but the results are acceptable. A similar behavior is expected for the pre-strained and bake hardened specimens. Yet, the assumption of isotropic bake hardening clearly gives an overprediction of the stress. The match between experimental data and the curve with neglected bake hardening indicate that the bake hardening effect in non-proportional loading is on the same order of magnitude as the error introduced by assuming von Mises plasticity. It is therefore difficult to justify inclusion of bake hardening unless a very accurate plasticity model can be determined first.

Regarding all simulations that included a bake hardening term, it can be concluded that the yield point and flow stress is over-predicted by the isotropic work and bake hardening rule. The unwanted failure mode of the tests and the uncertainty regarding the specimen clamping is not believed to invalidate this conclusion. This support

the hypothesis presented in literature, which suggest that the bake hardening effect diminishes under non-proportional loading. Hence, assuming an isotropic bake hardening effect can be expected to over-predict the strength under non-proportional loading. Still, it is surprising that the experimental curve more or less coincides with the numerical model that only included pre-straining. The expected result would be that the experimental curve fell somewhere in between the two simulations. Unfortunately, pre-strained samples alone were not tested, and hence it is difficult to conclude that the bake hardening had no effect compared to pre-straining alone. From a modeling perspective, however, this seems to be a plausible assumption.

The results from the tests on Docol 1200M are rather different than for Docol 600DP, as seen in [Figure 41b](#). The virgin material shows some plastic deformation before localized necking but the pre-strained and baked material undergo localized necking directly after yielding. The behavior is similar to the uniaxial tension tests and [Figure 45c](#) and [45d](#) confirm that the failure mode in fact is localized necking in the plane strain region of the specimen. The yield stress of the pre-strained and baked samples is higher than what is predicted by simulations considering pre-straining alone, which indicates an increase in yield stress that can be explained by dislocation pinning.

The observations indicate that bake hardening has a significant impact on the yield point and material ductility also in plane strain conditions and that no residual deformability after pre-straining and bake hardening exists. In turn, this can have implications for the applicability of the material in components where pre-straining from forming operations can be located in regions of subsequent uniform plane strain- or uniaxial tension. The question will be further discussed in the next chapter.

[Figure 41b](#) also compares the numerical simulations of the plane strain tension test with experimental data. It is apparent that the stress levels predicted by the original model are completely erroneous for most of the test duration. The modified model shown in [Figure 42b](#) shows significant improvement. The yield point seems to be accurately predicted for the virgin material. The point of strain localization is slightly early in the numerical model, but still acceptable considering that no non-local plastic thinning was used. Good correspondence is also seen for the work and bake hardened material by assuming isotropic bake hardening. The post-necking force drops too quickly as is common for explicit analyses, but the immediate necking seen in experiments is well represented. The stress analysis using DIC strains, shown in [Figure 43b](#), further confirms that the material model is well calibrated for small strains of the virgin material. Isotropic work and bake hardening is also shown to give good prediction of experimental data for the work and bake hardened specimen.

Please note, however, that simulations shown in [Figure 41b](#) and [42b](#) were not run with the SIMLab Metal Model.

The strain distribution at maximum force for all specimens is shown in [Figure 46](#). As seen, the minor strain is very small over most of the gauge region, which indicates that the strain state is close to plane strain. Interestingly, the virgin specimens show larger strains close to the notches than the bake hardened ones, but quite similar strains in the center of the gauge region. This is particularly true for the Docol 1200M-samples. Apparently, the higher normalized displacement at maximum force of the virgin 1200M-samples is due to increased stretching of the material close to the notches, rather than of the entire gauge region. This can be verified by comparing the strains at maximum force shown in [Figure 44b](#) – the virgin and bake hardened specimens both have very similar (and extremely low) strain-to-necking in the center, but the difference is large at the notch.

The strain to necking for the virgin material given in [Figure 44b](#) is easily compared with the Forming Limit Diagram given in the datasheet for Docol 1200M [30]. The results from the plane strain tension tests indicate that the necking strain in plane strain conditions is approximately 1%. Such small strains are on the limit of what can be measured by DIC, cf. [Figure 40](#). The  $FLD_0$  given in the datasheet, on the other hand, is about 10%. It seems that the plane strain tension test provide a very poor estimate of formability, compared to the pure formability tests that most likely are the basis of the FLD presented in the datasheet. The reason for this is unclear. While the test geometry is fundamentally different, the goal of the tests is the same: To stretch the material until failure at conditions as close to plane strain as possible. The explanation could possibly be found in the way that the failure strains are calculated in a formability test, but as this is beyond the scope of this thesis it is left for further work. Another possibility is that strain rate effects have lowered the strain-to-failure, but as shown in [Figure 47](#) the strain rate is in the vicinity of the predicted  $1 \times 10^{-3}/s$  in most parts of the specimen.

Finally, it should be noted that no material tests have been performed on material subjected solely to bake hardening, or to pre-straining alone. This study has therefore by no means covered all aspects of the bake hardening effect in plane strain conditions. The study should have however covered the two most interesting scenarios from a structural ductility point of view and it should be possible to draw some general conclusions from the observations.

The following summarize the results of the plane strain tension test. For Docol 600DP, a smooth yielding behavior was seen for all specimens and no obvious effect of the baking, neither positive nor negative, could be observed. The specimens failed prematurely due to crack initiation in the notches, but up to this point, no decrease in ductility was found. For Docol 1200M, the specimens from virgin

material did undergo some plastic deformation before onset of localized necking and showed a similar hardening behavior as in uniaxial tension. It was noted that almost none of this deformation occurred in the gauge region between the notches. The pre-strained and baked specimens showed rapid localization directly after the yield point. The numerical models assuming isotropic bake hardening all over-predicted the strength increase.

#### 4.2 PARAMETER IDENTIFICATION

The parameters of the work hardening curve calibrated in MatPrePost is given in [Table 1](#). The parameter identification of the present work, as well as that of [\[21\]](#), is plotted against the respective experimental curves in [Figure 48](#). Due to the fact that the parameters for Docol 600DP from [\[21\]](#) is used in an analysis where the pre-strain is given explicitly in the numerical model, no shifted work hardening parameters have been calculated. Please confer [Section 3.4.3](#), where the plane strain bending analysis is outlined. The corresponding curves for Docol 1200M are given in [Figure 49](#).

The force-displacement curves given by the parameter study on the uniaxial tension test of Docol 600DP is given in [Figure 50a](#). As expected, all curves followed the experimental data for which it was calibrated very well up to the point of necking. The simulations using explicit time integration then showed a very rapid, unphysical drop in the force. It was observed that the deformation had localized to a single inclined row of elements, which led to a rapid reduction in area in these elements. The ability to represent the physical neck decreased even more with mesh refinement, since the single row of elements that received all deformation became even more narrow. Since the purpose of the inverse modeling was to try to improve parameters by considering the post-necking behavior, explicit time integration was quickly abandoned.

By using implicit time integration, a much better qualitative reproduction of the physical diffuse necking was obtained. At a characteristic element size of 0.5 mm, the mesh was considered fine enough to accurately represent the experimental force-displacement curve. Since no apparent mesh convergence had been reached yet, it was decided to calibrate the constitutive model parameters for a given mesh size and use this throughout the rest of the analyses in the thesis. At 0.5 mm, the element size was rather small, but this was judged necessary both for the inverse modeling of the Docol 1200M samples and for the simulation of the plane strain tension test (due to a small notch radius).

[Figure 50b](#) show the simulation of the Docol 1200M uniaxial tension test on the virgin material with the original parameters of [\[21\]](#). Since the post-necking behavior was rather well captured with the

original parameters, the parameters were left unchanged. Using the additional parameter,  $\sigma_{100}$ , only raised the post-necking force further.

Figure 50c show the simulations of the pre-strained and bake hardened specimen of Docol 1200M. In this case, the original parameters after Hopperstad et al. did not give the immediate localized necking seen in experiments but gave a Lüder's plateau followed by a small amount of hardening before diffuse necking. In addition, the force at first yielding was lower than observed in experiments. The three bake hardening parameters were therefore adjusted iteratively such that localized necking occurred directly after yielding, that the peak force was correctly predicted and that the post-necking force resembled the one seen in experiments as closely as possible.

### 4.3 NUMERICAL SIMULATIONS

#### 4.3.1 Plane strain tension test

Please note that the results of the plane strain tension simulations are presented together with the experimental results in Section 4.1.2. The following text concerns the influence of geometry on the plane strain tension test.

The results from the variation of parameter  $w$  is shown in Figure 51a. The transversal-to-longitudinal strain ratio in the center of the specimen is plotted along the width of the gauge region. The symmetric part of the curves are omitted for clarity. Clearly, the *distribution* of the constraint is more or less insensitive to the width of the specimen, which is favorable since the extrapolation method of An et al. can be used. However, it can be concluded from the constraint ratio that a much wider specimen than the ones tested here must be used in order to resemble a true plane strain situation ( $\varepsilon_{22} \ll \varepsilon_{11}$ ).

The results from the alternative geometry adopted from [2], and the variation of the height,  $h$ , is shown in Figure 51b. The alternative geometry show a much higher constraint ratio over the width of the specimen compared to both the baseline version and the modified version of the reference geometry. The difference is even more pronounced after some plastic straining (dashed lines). If we require that  $\varepsilon_{22}/\varepsilon_{11} < 0.1$  over the majority of the specimen width, it can be concluded that only the alternative geometry is acceptable for the purposes of this study.

#### 4.3.2 Plane strain bending test

Figure 52 presents results of the plane strain bending tests previously reported in [26]. The results of the plane strain bending simulations in the present work are then shown in Figure 53 – 57. The measured

punch force has been scaled to represent the maximum stress in the outer fibers with respect to the initial configuration:

$$s = \frac{3FL}{2wt^2}$$

where  $L$  is the length between the initial contact points of the roller supports,  $w$  and  $t$  are the width and thickness of the specimen, respectively, and  $F$  is the force exerted by the punch.

Some major conclusions of the previous experimental study are that samples of Docol 600DP show a small but significant increase in flow stress after pre-straining and baking (cf. [Figure 52a](#)). For Docol 1200M, however, no significant trend in the punch force was observed between the virgin and pre-strained and baked samples (cf. [Figure 52b](#)). This was true irrespective of pre-strain level – all curves fell in approximately the same scatter band. The reader is referred to the previous report for a more thorough interpretation of the experimental bending results. For the purpose of this discussion it is sufficient to note that there is a possible bake hardening effect in Docol 600DP, while no effect of pre-straining and bake hardening is seen for Docol 1200M.

[Figure 53](#) show a comparison between experimental data and the numerical simulations for Docol 600DP. The simulations using parameters of the virgin material show excellent agreement with experimental data. However, as shown in [Figure 53a](#), it is clear that the assumption of isotropic work and bake hardening leads to an over-prediction of the stress for the pre-strained samples. Even if the Voce term that constitute the bake hardening is neglected, the stress at incipient yielding is over-predicted.

The results from identical simulations, but with part of the hardening assumed kinematic, is shown in [Figure 53b](#). The results from simulations show much better agreement with the experimental data. Quantitatively, the stress is still over-predicted by the full numerical model. However, if the bake hardening is neglected, as demonstrated by the curve labeled “20”, the stress level matches the experimental data well. Very similar results are given for the 60 % pre-strained and baked samples, as shown in [Figure 53c](#), when the same assumption of partly kinematic work hardening is applied.

These observations again support the hypothesis of vanishing bake hardening effect under non-proportional loading. To fully verify that this hypothesis is valid also for the materials considered here, it would have been beneficial to study the effect of pre-straining alone on the plane strain bending results. However, it can still be concluded that an isotropic bake hardening addition, such as the one used in these simulations, is inappropriate from a modeling point of view.

Notably, some oscillations in the stress curve given by the simulations are seen after some deformation despite filtering of the curve. This is probably due to the dynamics of the part of the specimen pro-

truding beyond the roller contact points, which becomes longer and longer as the contact point moves inwards along the rollers. The oscillations are not seen in implicit analysis, but they are relatively small and not expected to alter results significantly.

For Docol 1200M, the bending simulations using parameters for the virgin material show reasonable agreement with experimental data in the beginning of the deformation. However, for large punch displacement, the stress is grossly over-predicted and the point of maximum stress is inaccurately predicted. When pre-straining and bake hardening is taken into account, the point of initial yielding is also over-predicted. Although the error in the first part of the curve is not larger than the scatter in the experimental data, it is worth noting that the assumption of isotropic bake hardening seem to provide an insufficient description of the physical strengthening mechanism.

An explanation to the poor stress prediction in case of Docol 1200M could be the small range of plastic strains for which the hardening curve was calibrated. In addition, the non-uniform yielding of the uniaxial tension test that was revealed by the DIC measurement can have a contribution to errors in the model calibration. Since failure did not occur in the bending tests, large plastic strains developed in a relatively small region of the bending specimen. The numerical simulations predicted plastic strains of about one order of magnitude larger than the strain to necking in uniaxial tension. By contrast, the hardening curve is calibrated at small strains, averaged over a comparably large distance. Hence, it is no surprise that the present calibration fail to correctly predict the bending test. A more correct description could in this case be obtained by for example in-plane shear tests, where the hardening rate at large plastic strains can be obtained without risk of localized necking [24].

Another, albeit more far-fetched, explanation is that excessive deformation of the elements lead to erroneous forces at large punch displacements. Figure 57 show the deformed mesh at a quite large punch displacement of the Docol 600DP-simulation and as seen, only a few elements receive almost all plastic deformation. In the simulations on Docol 1200M, the deformation was even more concentrated. Since only linear shells (shell elements lacking out-of-plane curvature) are available in LS-DYNA, the mesh could impose a restriction of the model's ability to represent the real test. This effect is however not believed to be the major factor causing the large deviations from experimental data. A rerun with a finer mesh, where each element was split into four, gave no sign of the force-displacement curve having any different shape.

Figure 55 show the tension-compression test of the single element model that was used for pre-straining the Docol 600DP bending model. As seen, the kinematic hardening curve (curve B in Figure 55a) has a lower yield stress in compression. The pre-strained kinematic harden-

ing curve (curve C in [Figure 55a](#)) has an initially high yield stress in reloading in tension, but in compression the yield stress is identical to the virgin kinematic hardening curve. The behavior seen in [Figure 55b](#) confirms that the desired overall hardening curve is obtained, also for the pre-strained material.

Results from the small sensitivity study performed for the bending simulations on Docol 600DP is shown in [Figure 56](#). The curve derived from implicit time integration does not exhibit the small oscillations seen in the (filtered) explicit time integration curve, but the deviations are very small. The curve derived from explicit time integration using reduced integration shell elements, on the other hand, show very peculiar results, especially at incipient yielding. One explanation could be that a warping hourglassing mode has been triggered, which is difficult to see by inspection of the model. It is otherwise difficult to explain the poor results of these elements. The high frequency oscillations are due to the contact force, and could have been filtered away, as it has been in all other explicit analyses.

Summarizing the results, it is noted that for Docol 600DP samples, flow stresses are accurately predicted by numerical models assuming only work hardening. It can be assumed, then, that bake hardening give no strength increase and hence little hope for extra energy absorption in bending modes. As concluded by [Hagström and Ryde](#), the Bauschinger effect makes it difficult to benefit from strengthening by bake hardening. Because the yield strength in reversed loading is much lower, the bending samples deform in compression rather than symmetric tension-compression, which lead to negligible increase in strength.

The samples of Docol 1200M showed no effect of pre-straining and bake hardening at all [\[26\]](#). No increase in yield point was observed despite the fact that the Bauschinger effect is expected to be lower for this single phase material. No failure initiation was observed. A plausible explanation that yielding mainly occur in compression also in this case, since this side has significantly lower yield stress. Due to low work hardening, the stress in the material fibers on the compression side never reach the yield stress of the fibers on the tension side.

## DISCUSSION

---

In this chapter, the results of the present work are discussed in a broader context. The fulfillment of the objectives are addressed and the contribution of the study is discussed, followed by a conclusion and suggestions for further work on the subject. In the introductory chapter, the objectives were presented as

- A. To investigate and document the characteristics of deformation bands, strain localization and failure of material tests of Docol 600DP and Docol 1200M.
- B. To evaluate the existing model concept with respect to its accuracy in representing the response and structural ductility of simple and complex (though generic) components.

In the following, the work is divided into parts of experimental nature and parts of modeling nature and each objective is discussed separately, followed by a summary and some final conclusions.

### 5.1 CHARACTERISTICS OF BAKE HARDENING

The characteristics of the bake hardening effect in dual-phase and martensitic steels have been thoroughly studied and reported in previous work, most notably [18] and [20, 21]. In the present work, sophisticated field measurement techniques have been used to study the details of the deformation and failure patterns that are outlined in previous work. In addition, the most relevant aspects of the bake hardening effect in plane strain tension has been studied.

The results of the present uniaxial tension tests have shown the fundamental difference between the yielding behavior of dual-phase and martensitic steels, both in virgin as well as pre-strained and bake hardened condition. Through the use of DIC, it was documented that the deformation of Docol 600DP was smooth in time and evenly distributed over the test specimen. This was true also for the bake hardened state. By contrast, the deformation of Docol 1200M showed spatial non-uniformity and, in the case of pre-strained and baked material, a rapid sequence of events that are best explained by unpinning of dislocations followed by immediate localized necking. No actual Lüder's bands were observed for the pre-strained and baked material. The uniaxial tension tests did however reveal unexpected aging and Lüders behavior of the pre-strained Docol 1200M.

The plane strain tension tests in the present work have contributed to an increased insight in how the strain localization and failure in

plane strain is affected by baking. Generally, the material behavior was similar to that observed in uniaxial tension, meaning smooth yielding and no obvious deterioration of ductility for bake hardened Docol 600DP and rapid localized necking for bake hardened Docol 1200M. Specimens subjected solely to pre-strain were unfortunately not tested. It is also questionable whether plane strain tension tests are applicable for estimating the actual  $FLD_0$ , since the necking strains are far below what is found in datasheets, even for virgin material. The trends with regard to strain localization and failure are nevertheless quite clear.

Summarizing the results of the uniaxial and plane strain tension tests, one can conclude that the good elongation properties of Docol 600DP is pertinent also in plane strain tension, but that the strength increase was smaller than predicted by isotropic bake hardening when non-proportional reloading was used. Furthermore, the poor elongation properties of Docol 1200M also pertains to the plane strain tension situations. Hence, it is not simply connected to the test method but should rather be considered a state of the material.

It can be argued that the choice to perform the pre-straining of the plane strain specimen in a different mode than the reloading after baking was unwise. Based on previous knowledge, non-proportional reloading render the bake hardening less effective and hence, the tests done in the present work did not correspond to a "worst case" scenario. The results of the tests, however, show that early necking instability occur even under non-proportional loading for Docol 1200M, which serve as an even stronger indication on the importance of investigating the relevance of these results for engineering applications.

Upon discussing the results of the present work in relation to structural components, the obvious should initially be stated: The test specimens studied in the present work are far from representative for common states of stress and strain in a component. On the contrary, test specimens are designed to, as far as possible, isolate the material response from geometrical influence. The first question to consider is therefore if strength increase or early strain localization of material tests are at all relevant for component behavior.

For the sake of discussion, the plane strain bending tests serve as a good example of an intermediary between pure material tests and component tests. The stress state in a bending specimen is relatively simple, yet there is possibility of interaction between the hardening behavior in tension and compression as well as failure initiation on either side of the specimen. As already mentioned in the last chapter, the bending tests were completely insensitive to baking, which could be explained by the possibility of all the yielding to take place in compression. Can the insensitivity to baking be generalized to all components in which there are mixed modes of loading?

The fact that fracture criteria are calibrated from plane strain tension tests [24] are of course a strong argument in favor of the relevance of material tests. Furthermore, there are examples of situations that could resemble a uniaxial or plane strain tension situation closer than the bending test. One example of a situation where, for example, yielding in compression is not an option could be bending of a hollow cross section beam where the tension flange has been subjected to sufficient pre-straining (e.g. through forming of stiffening grooves) and baking. Conceivably, the stress state in the flange could be similar to the one in the plane strain specimen. As a result, localized (through-thickness) necking could lead to rapid failure of such a component if a martensitic steel is used. Similarly, an increase in strength and energy absorption could be the outcome if a dual-phase steel is used. Case studies like this are not trivially resolved and could be an interesting continuation of the present work. As mentioned in [Chapter 2](#), some studies documenting increased energy absorption in dual phase steels after baking already exist in the literature. Despite this, it is the author's view that the field is not exhausted and more work is needed to document what combinations of design and load cases that evoke the same strengthening/failure mechanisms that are seen in the idealized tests presented in this work.

## 5.2 EVALUATION OF CONSTITUTIVE MODEL CONCEPT

As part of the evaluation of the bake hardening modeling concept, this work has included sensitivity studies with regards to mesh size, time integration method and element formulation, as well as comparison of simulations of plane strain tension and bending tests with experimental data. Based on the sensitivity study, a characteristic element size of 0.5 mm was used throughout all simulations. As the success of the modeling concept differ between the two studied materials, they will be discussed separately.

The results for Docol 600DP have shown that the constitutive model give excellent prediction of the virgin and pre-strained states in uniaxial tension, plane strain tension and plane strain bending, provided a sufficiently fine mesh and consideration of kinematic hardening effects. The treatment of bake hardening does however lead to overpredicted forces in both plane strain tension and plane strain bending tests. A better approximation is seen by simply neglecting bake hardening in the constitutive model. It is difficult to draw any conclusion on the model's ability to predict failure, due to unexpected failure of experimental tests and uncertainty regarding clamping distance of PST tests. It should however be clear that a better description of the changes in the yield surface due to bake hardening is needed if the strength increase is to be accounted for with confidence.

For Docol 1200M, the parameter identification for the virgin material has proven to be non-trivial and the standard calibration procedure is believed to introduce errors due to non-uniform yielding in uniaxial tension. For this reason, the success in representing the virgin and pre-strained states has been mixed. The response of the plane strain tension specimen is acceptably represented, but results from plane strain bending simulations are unsatisfactory. In situations where large strains occur, it is likely that a fundamentally different parameter identification procedure is needed, in view of the previously described difficulty to improve parameters by inverse modeling of the uniaxial tension test. Inverse modeling of in-plane shear tests is one possibility for parameter identification at large strains. Another interesting approach, which is under development at NTNU as a continuation of the work by [Fagerholt](#), is to use optimization software together with the DIC and constitutive driver to fit material parameters directly from DIC measurements of material tests. Such a procedure could improve parameter identification significantly.

The numerical representation of bake hardening yielded promising results with respect to failure prediction for Docol 1200M, since the point of strain localization of the work and bake hardened plane strain tension specimen was well captured. Note however that prediction of strain localization require a sufficiently fine mesh; in this study a characteristic length of 5 mm was used. The constitutive model predicted no failure in the plane strain bending simulations, which is also in accordance with experimental observations. The assumption of isotropic bake hardening did not seem to exaggerate forces as clearly as for Docol 600DP. The only drawback of the current modeling concept, when applied to Docol 1200M, was computational cost.

Due to the explicit nature of the SIMLab Metal Model, computational cost for the small models considered in this work was largely determined by the number of time steps required to reach a given simulation time, since the mesh size was fixed. The high strength of Docol 1200M meant that the elastic region was large, leading to long simulation times before any plastic deformation. In addition, numerical instabilities were observed in the plane strain tension simulations due to the imposed time scaling, implying that much longer simulation times would have had to be used. Instead, to limit the computation time, a LS-DYNA library material model with implicit features was chosen. The implicit-explicit switching feature of LS-DYNA improved computation time significantly. An implicit feature of the SIMLab Metal Model had given analysts greater freedom with respect to solution method and should be considered in future releases.

## CONCLUDING REMARKS

---

The main conclusions of the present work and possible continuations can be summarized as follows.

### 6.1 SUMMARY AND CONCLUSION

An experimental test programme has been conducted and the results has revealed more details regarding the deformation and failure mechanisms in dual-phase and martensitic high-strength steels subjected to bake hardening. In particular, DIC and thermographic images have proved to be very useful tools for material test analyses. Test results show that bake hardening has a dramatic influence on material behavior in some cases, while in other cases no effect is seen.

Docol 600DP has shown a smooth yielding behavior in all material tests, also after pre-straining and baking and no indication on deterioration of ductility has been found. A strength increase in proportional reloading after baking is seen, but has not been observed to the same extent in other modes of loading, indicating the path dependence on the hardening effect. Precipitation is believed to be the main strengthening mechanism and the smooth yielding after baking can be attributed to the dual-phase nature of the material. These conclusions are in agreement with literature.

Docol 1200M has exhibited a tendency of non-uniform yielding in virgin condition and strong response to both room-temperature and artificial aging. Very low elongation values before failure was observed in both plane stress and plane strain tensile conditions of work and bake hardened specimen. Previous work have shown that no failure occurs in bending, underlining the strong dependence on mode of loading.

A modeling concept proposed in literature has been used for numerical simulation of material tests. The constitutive model was proved to be well suited for describing the virgin dual-phase steel, provided that the Bauschinger effect is considered, but the bake hardening effect is not treated accurately under the proposed assumptions. In cases of non-proportional loading and general stress states, strength increase from bake hardening is exaggerated. It can therefore not be recommended to include bake hardening in its current formulation in component studies of dual-phase steel.

Regarding the martensitic steel, uncertainties still remain regarding the numerical representation of the virgin material at large strains.

Despite this, the modeling concept and the current treatment of bake hardening show promising results for use in studies related to component failure. If plastic strains are limited to moderate levels and a sufficiently fine mesh is used, a good representation of the strength and ductility of material tests have been found.

## 6.2 RECOMMENDATIONS FOR FURTHER WORK

In view of the results and conclusions presented in this report, the following topics could be considered as starting points for further work:

- Improve the constitutive representation of bake hardening for dual-phase steels. Other means of modifying the yield surface in a physically sound manner should be surveyed
- Evaluate the applicability of the modeling concept to larger-scale component studies
- Consider alternative parameter identification procedures for the martensitic steel if large plastic strains are to be modeled
- Extend the bake hardening modeling concept to other types of advanced high-strength steel, if possible
- Implement implicit analysis features in the SIMLab Metal Model, as this significantly reduces computational cost of simulations of martensitic steel components with fine mesh resolution

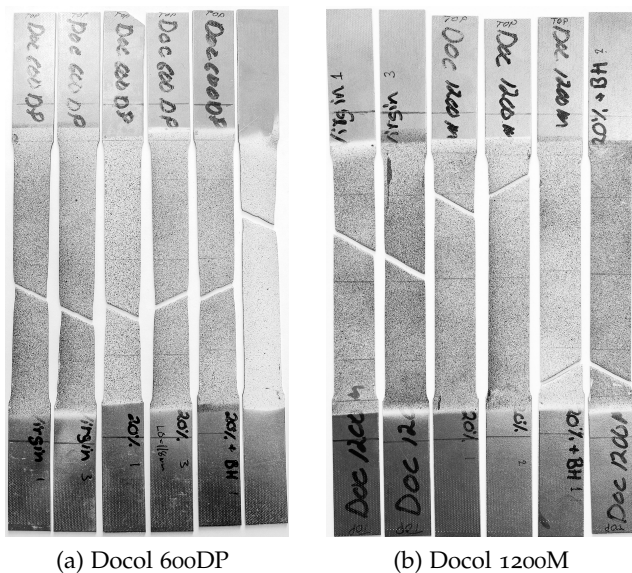


Figure 24: Fractured uniaxial tension specimens, oriented in the direction of testing

*(back)*

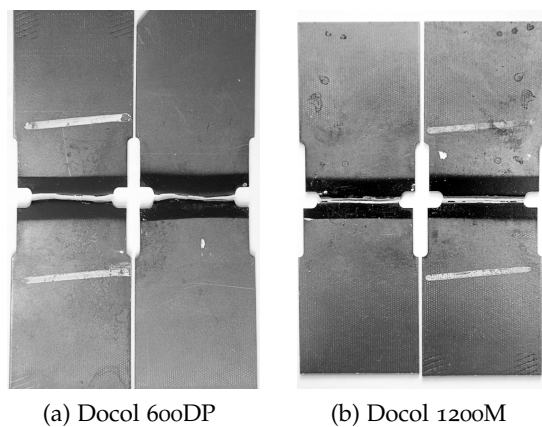


Figure 25: Fractured plane strain tension specimens

*(back)*

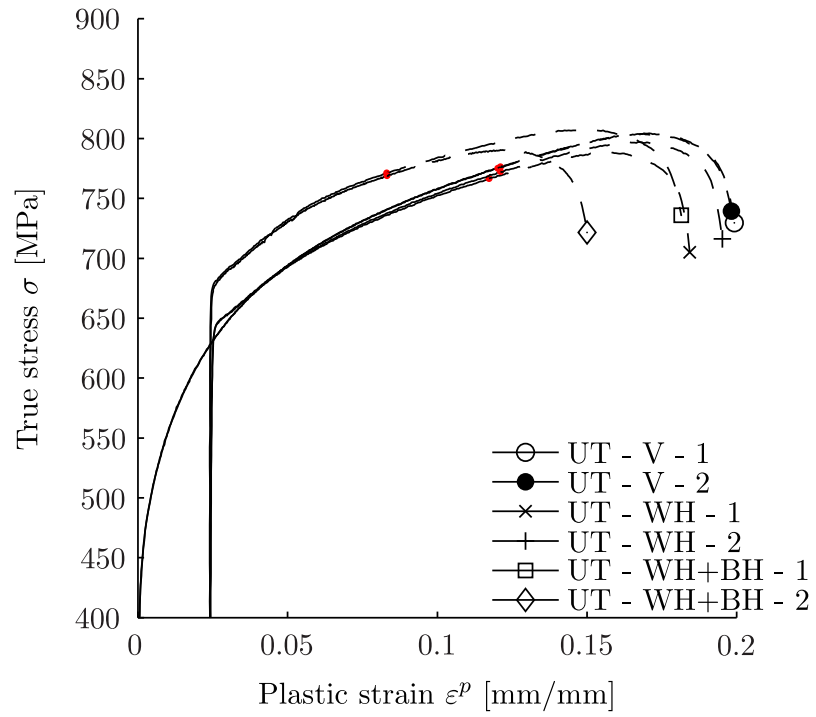


Figure 26: Uniaxial tensile tests, 600DP

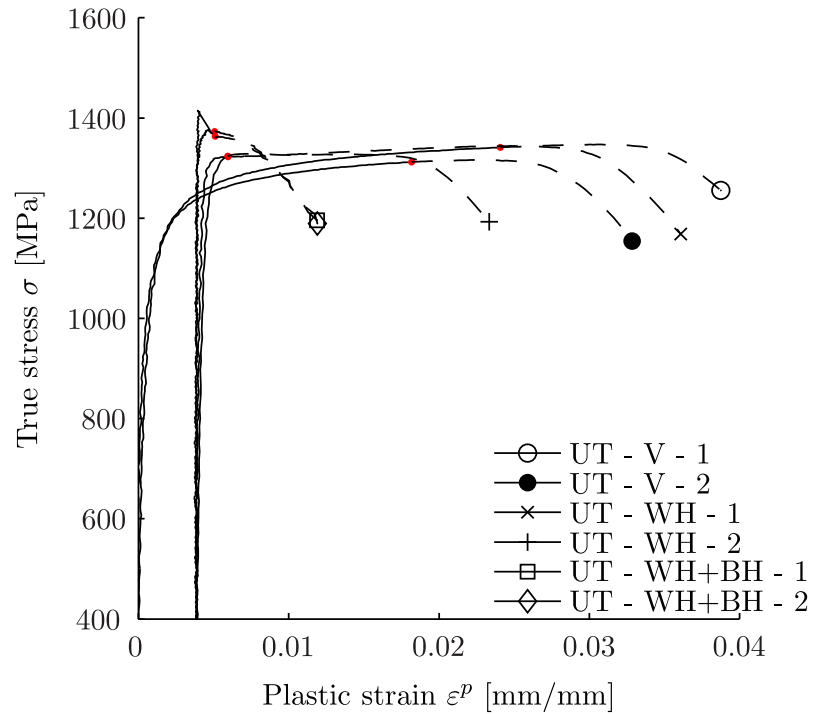
*(back)*

Figure 27: Uniaxial tensile tests, 1200M

*(back)*

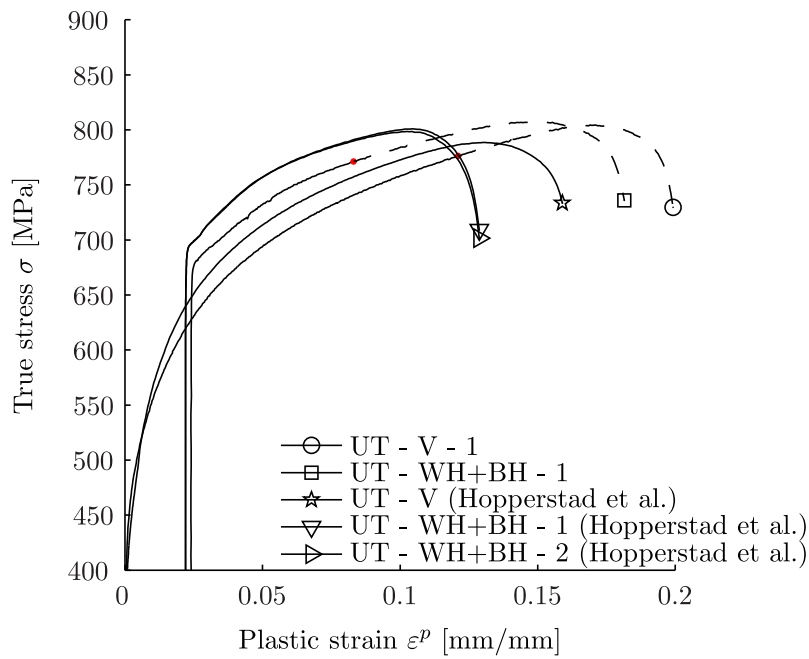


Figure 28: Uniaxial tensile test from present work, as well as from [21]; Do-col 600DP

(back)

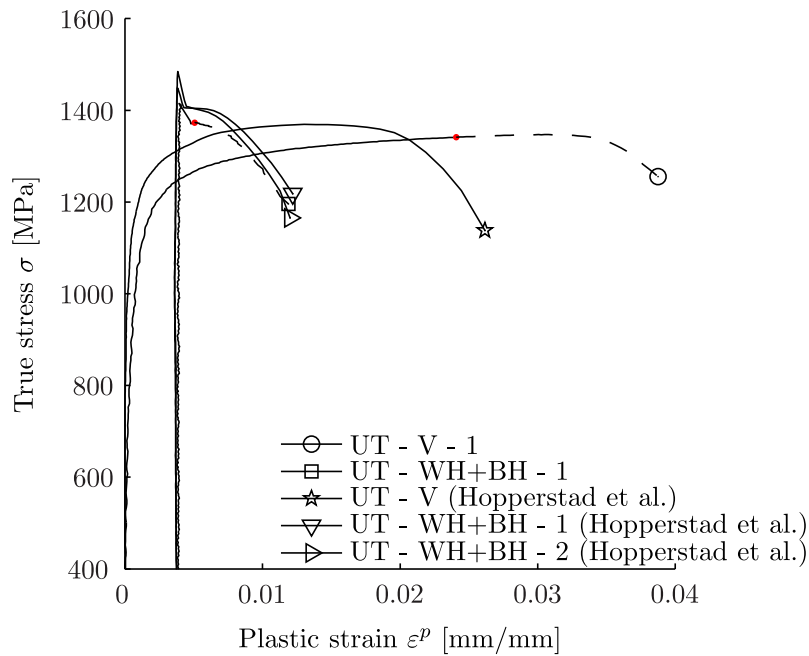


Figure 29: Uniaxial tensile test from present work, as well as from [21]; Do-col 1200M

(back)

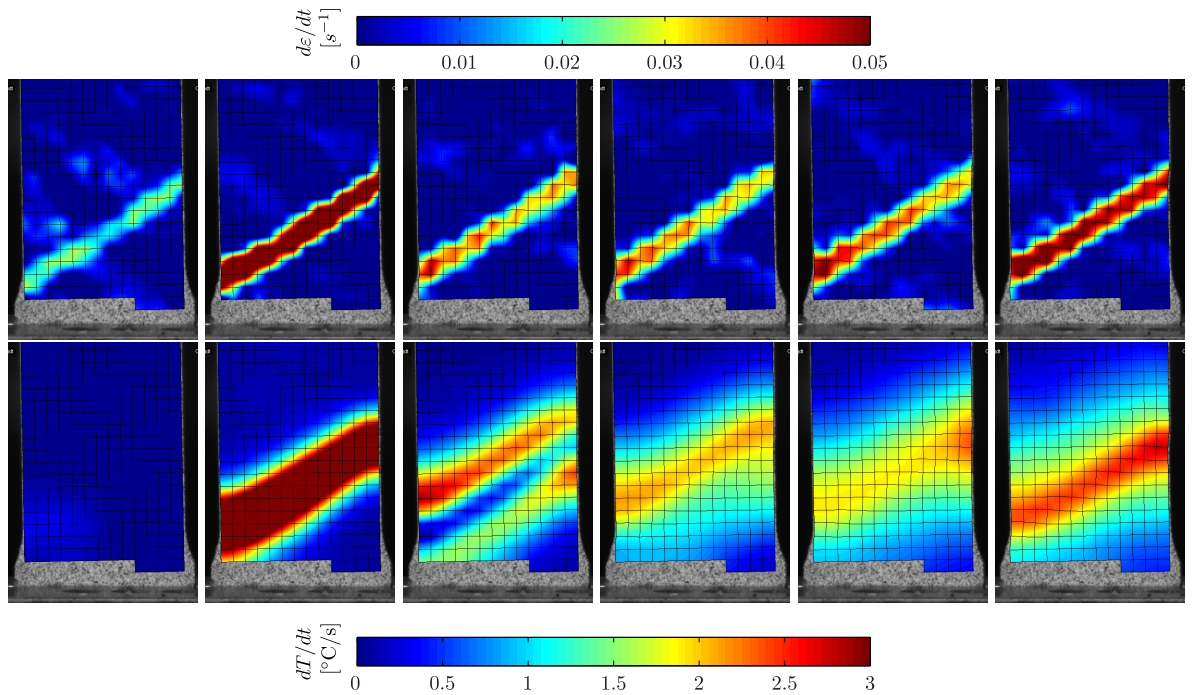


Figure 30: Details of field measurement, Docol 1200M bake hardened;  
Strain rate (top) and rate of temperature change (bottom);  
Not corrected for heat conduction;  
 $\Delta t = 0.5s$ , cf. Figure 32c

*(back)*

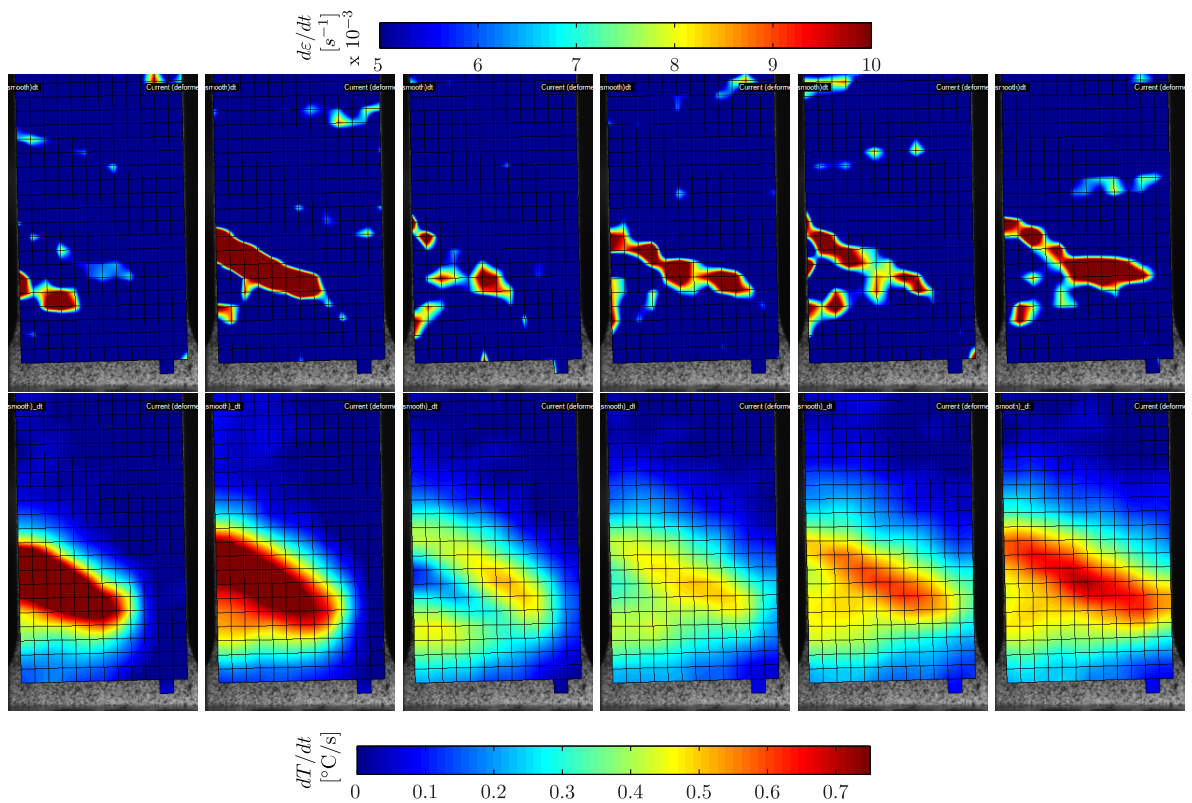


Figure 31: Details of field measurement, Docol 1200M UT-BH-2;  
Strain rate (top) and rate of temperature change (bottom);  
Not corrected for heat conduction;  
 $\Delta t = 0.5s$ , cf. Figure 32d

*(back)*

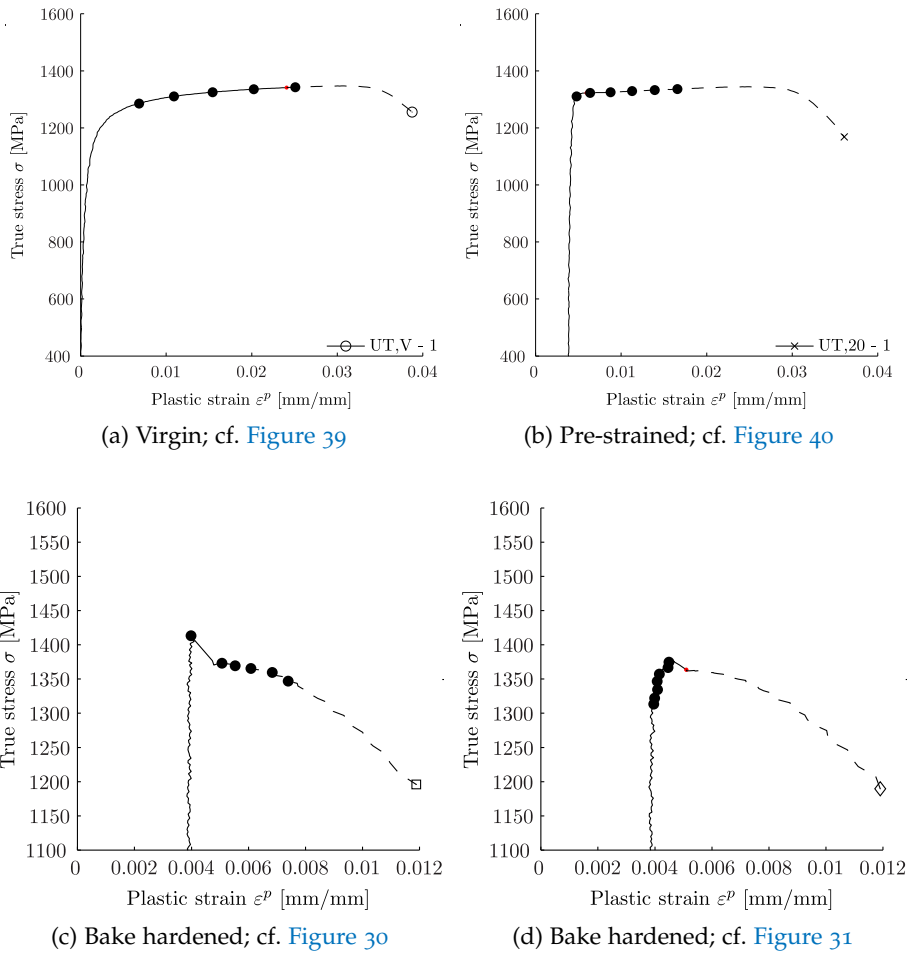


Figure 32: Location of time instants on stress-strain curve corresponding to frames in the detailed time series

(back)

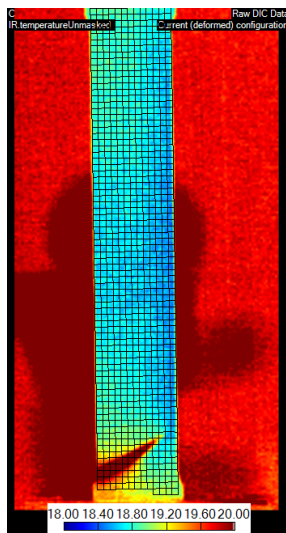
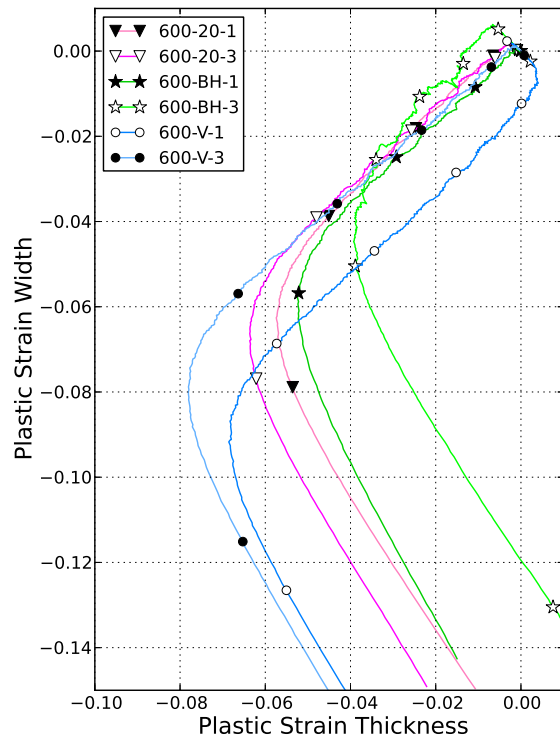
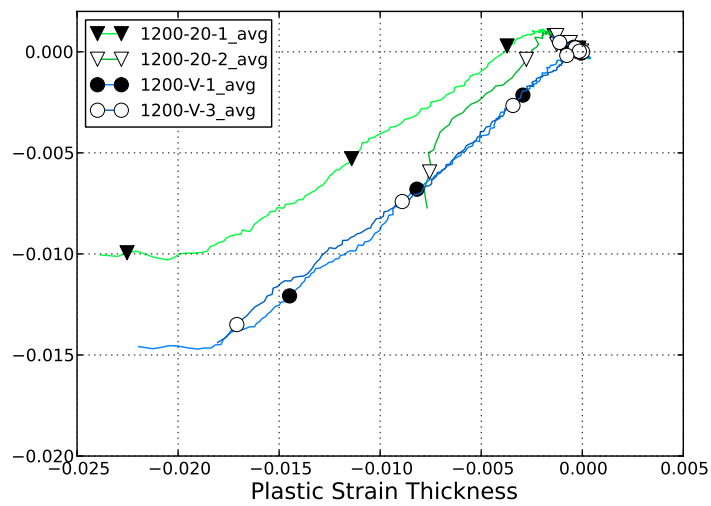


Figure 33: Thermographic image of incipient yielding of Docol 1200M; Colorbar show temperature in °C



(a) Docol 600DP



(b) Docol 1200M

Figure 34: Direction of plastic strain under uniaxial tension;  
Plastic anisotropy (R-value) is deduced by determining the slope  
of the curves

*(back)*

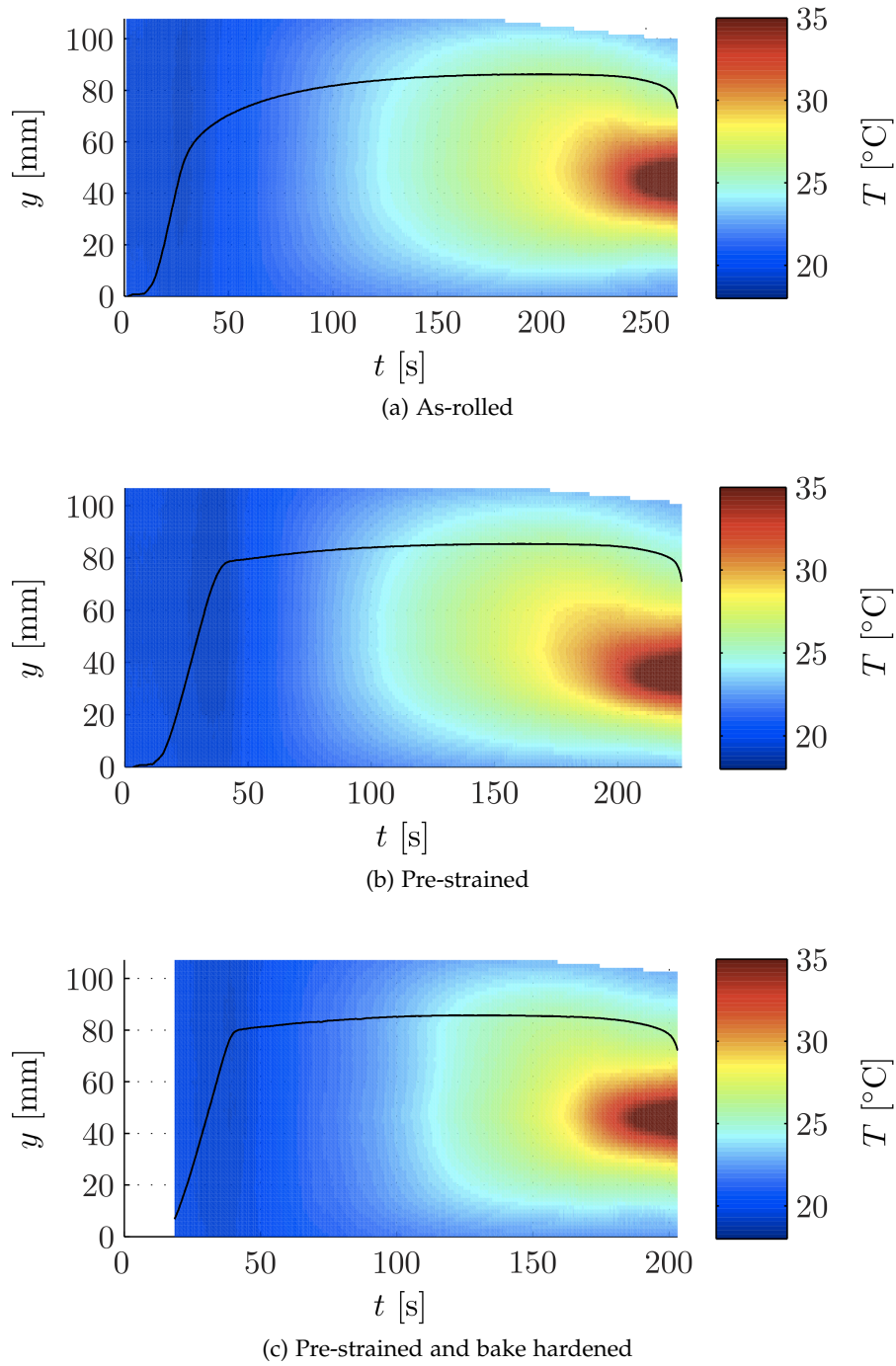


Figure 35: Time series of temperature along midline of specimen with superimposed force-time curve;  
 Spatial coordinates refer to initial configuration

*(back)*

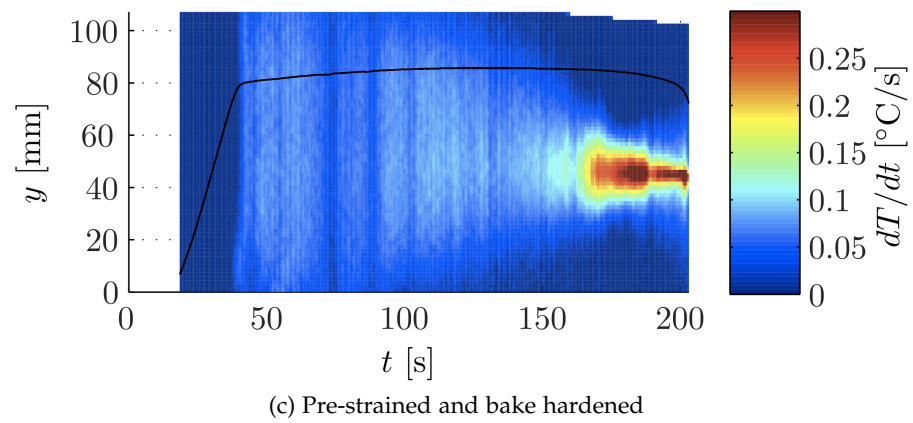
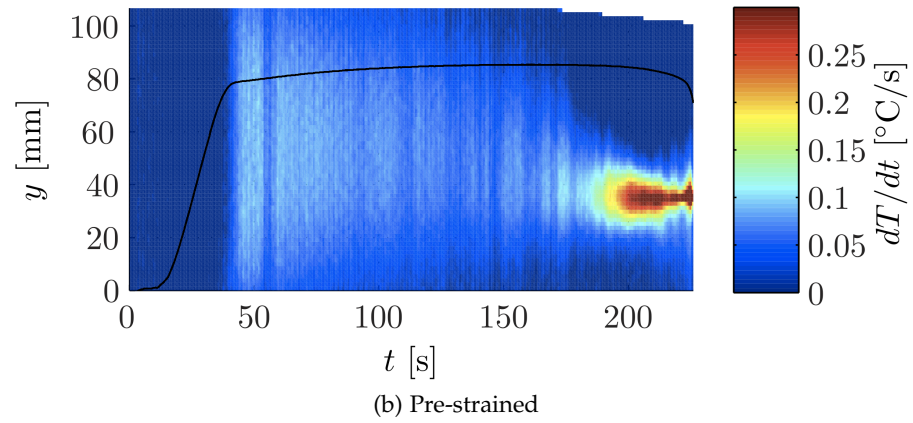
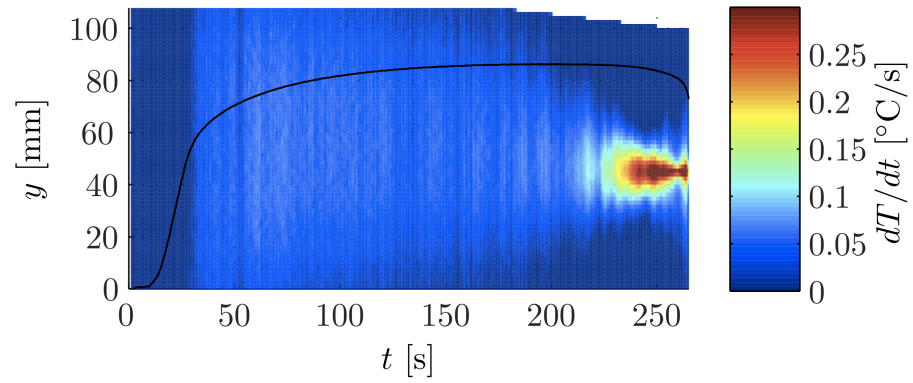


Figure 36: Time series of time derivative of temperature along midline of specimen with superimposed force-time curve; Spatial coordinates refer to initial configuration

*(back)*

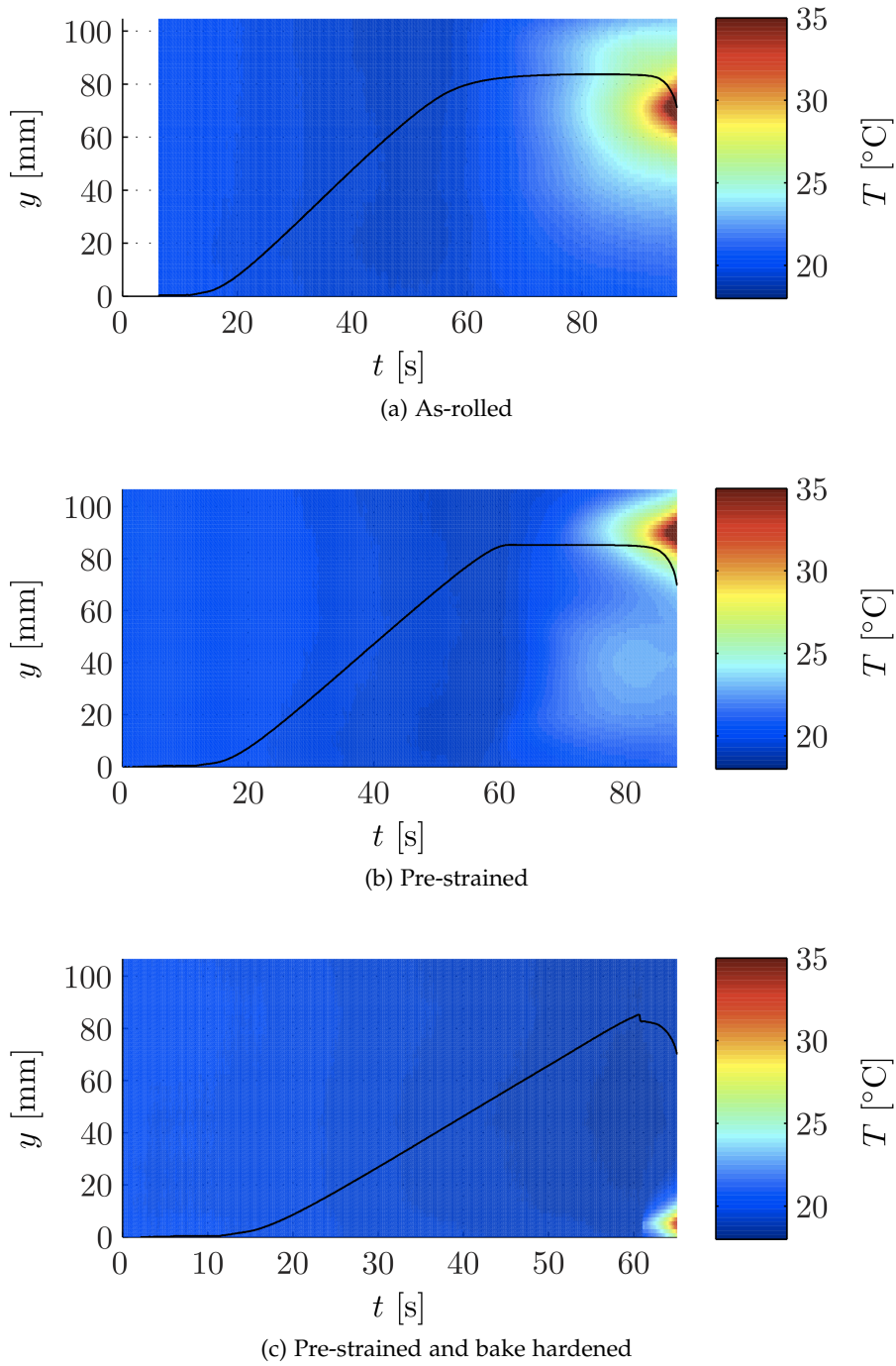


Figure 37: Time series of temperature along midline of specimen with superimposed force-time curve; Spatial coordinates refer to initial configuration

*(back)*

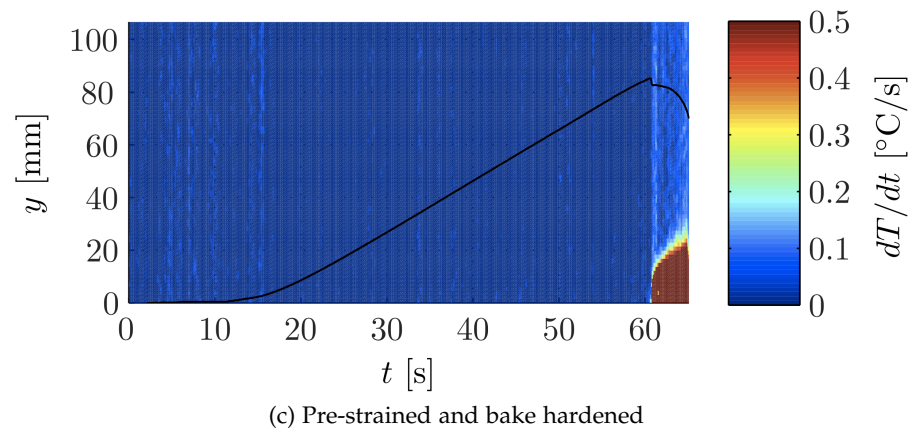
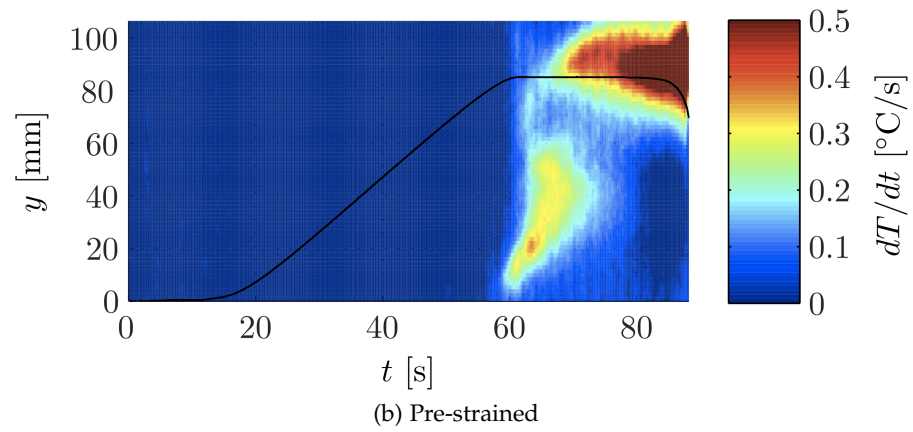
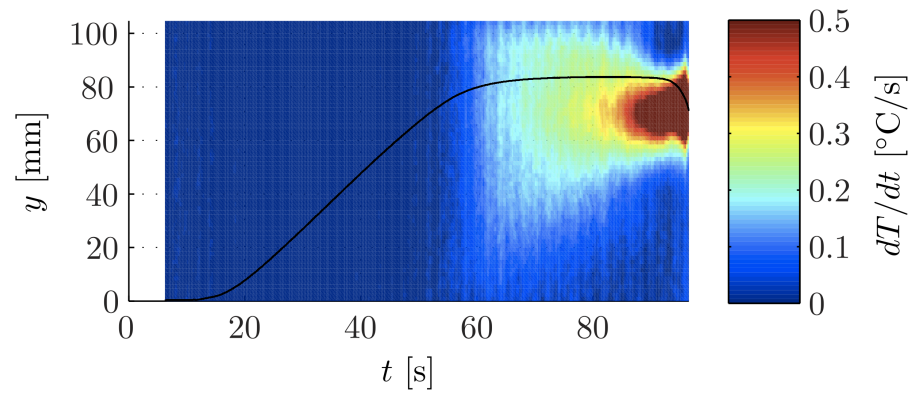


Figure 38: Time series of time derivative of temperature along midline of specimen with superimposed force-time curve; Spatial coordinates refer to initial configuration

*(back)*

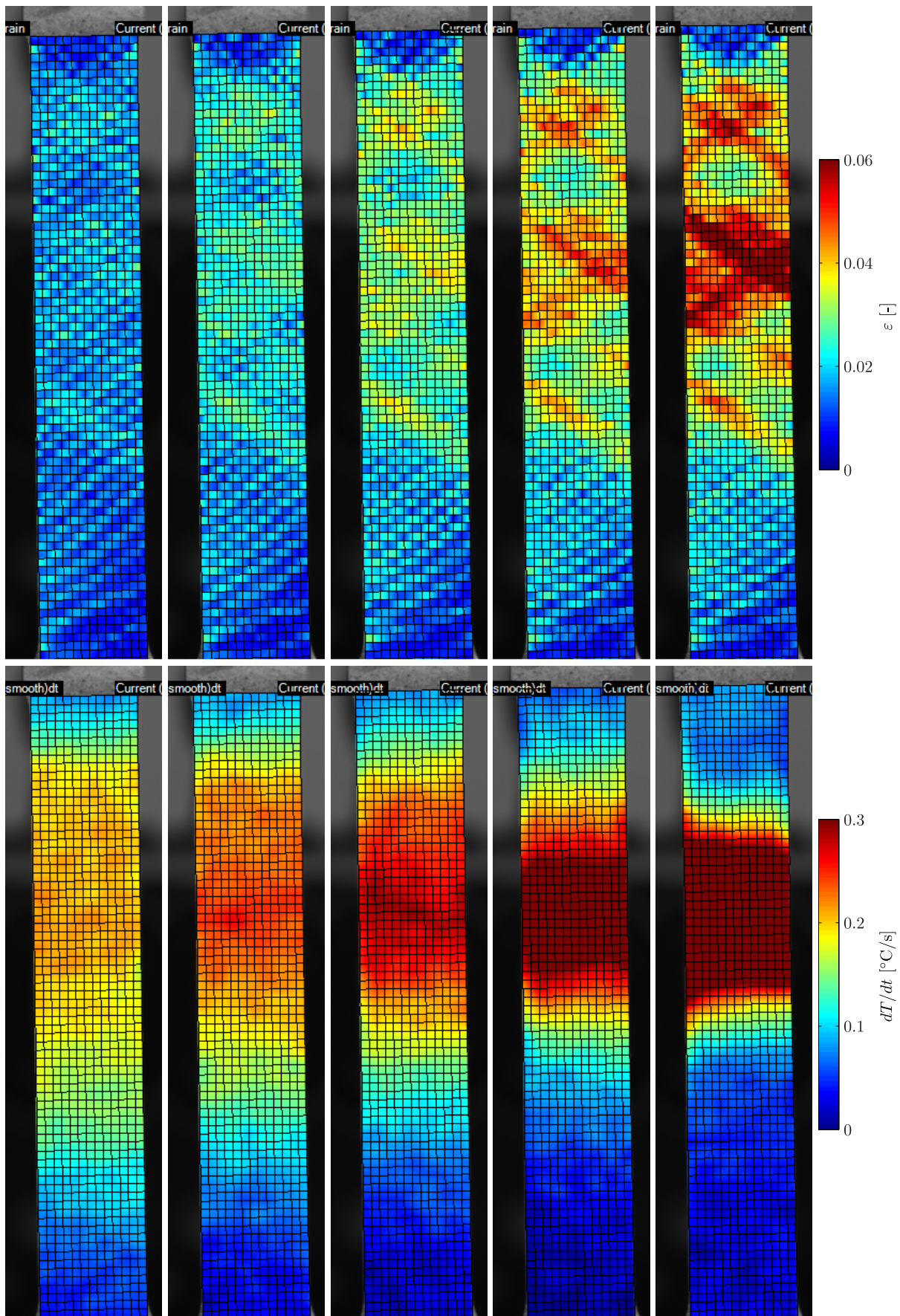


Figure 39: Details of field measurement, Docol 1200M as-rolled;  
 Total strain (top) and rate of temperature change (bottom);  
 Not corrected for heat conduction;  
 $\Delta t = 5s$ , cf. [Figure 32a](#)

*(back)*

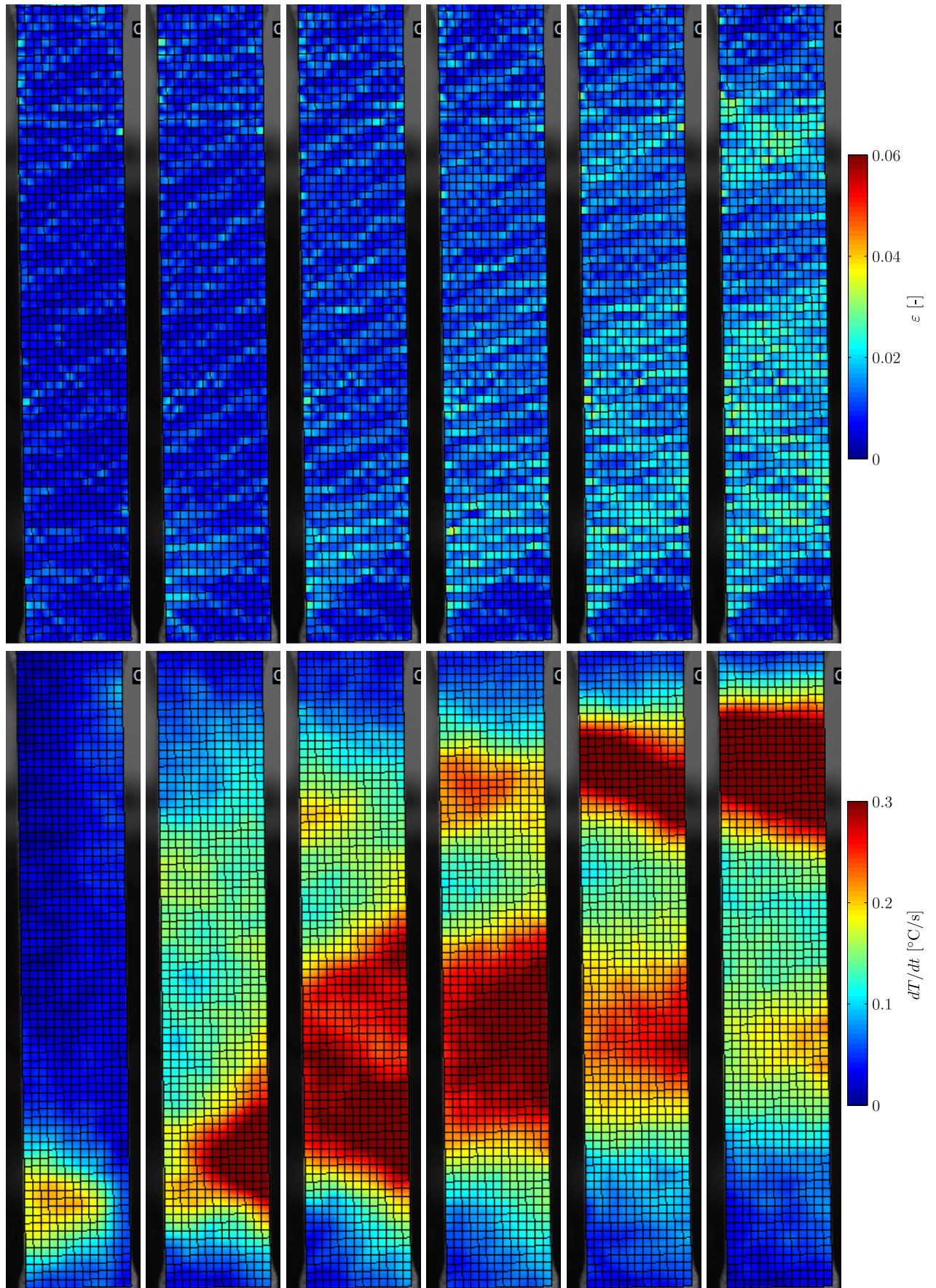


Figure 40: Details of field measurement, Docol 1200M pre-strained;  
 Total strain (top) and rate of temperature change (bottom);  
 Not corrected for heat conduction;  
 $\Delta t = 2.5s$ , cf. Figure 32b

*(back)*

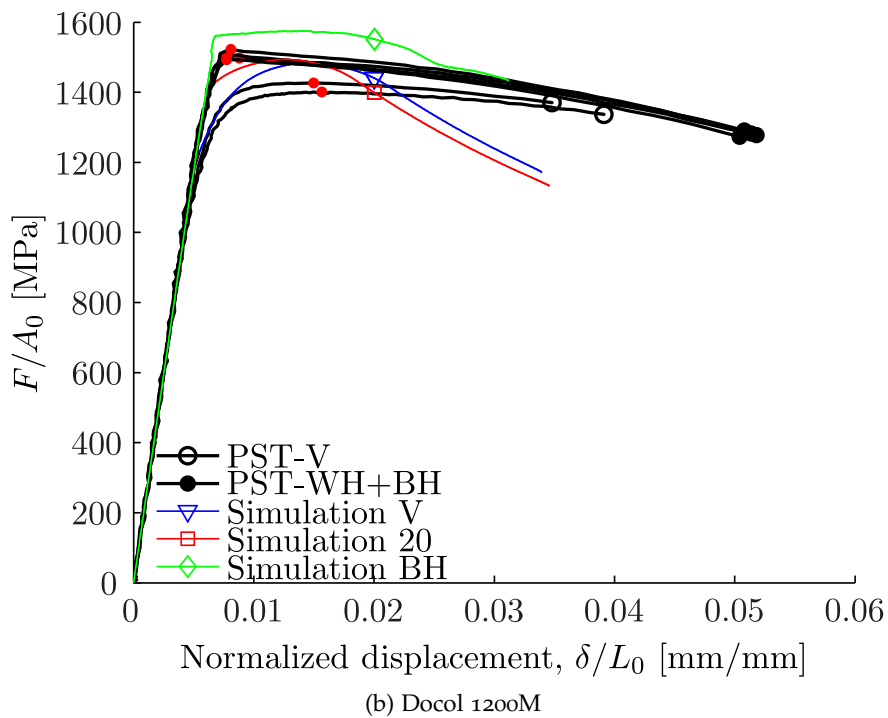
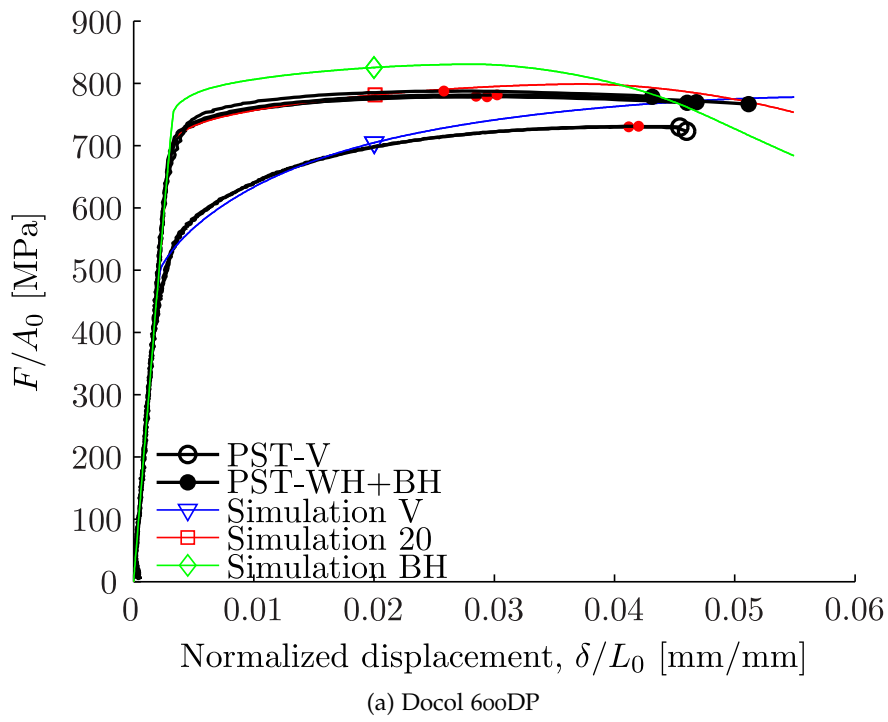


Figure 41: Experiment and numerical simulation of the plane strain tension test, original geometry;  
 LS-DYNA library material model used for simulations  
*(back)*

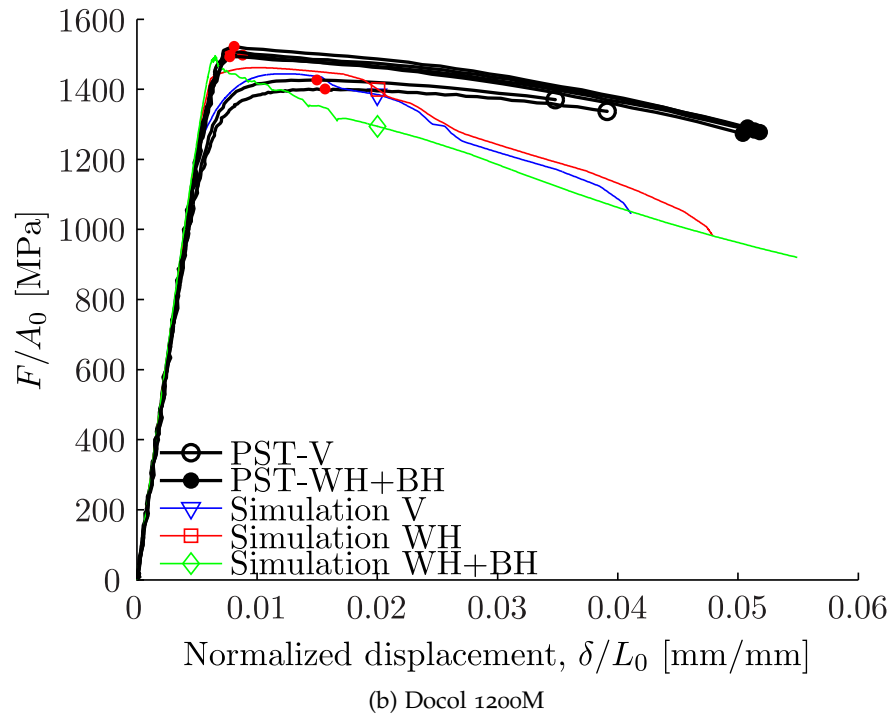
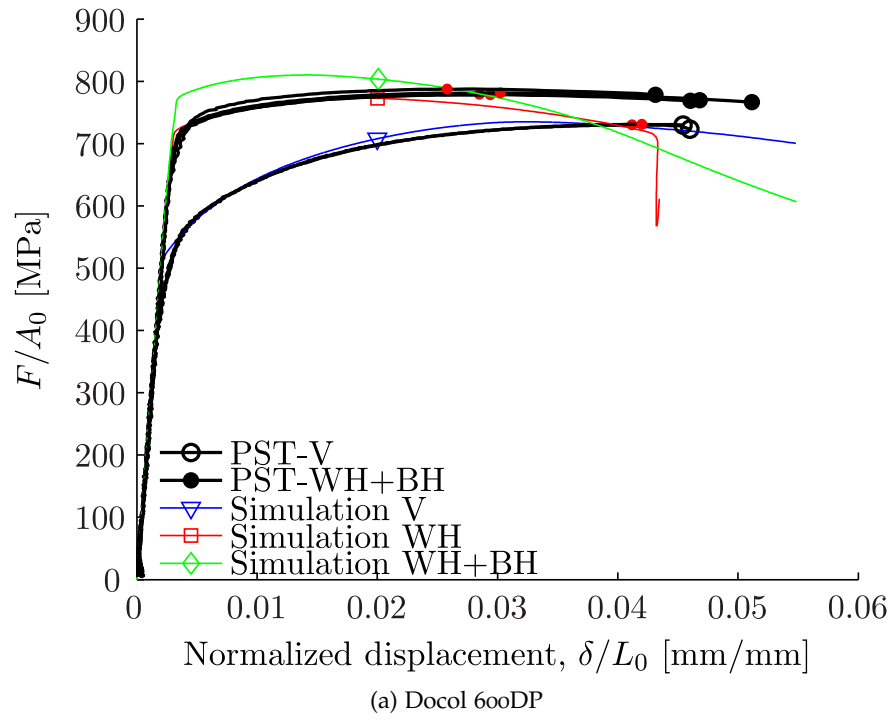


Figure 42: Numerical simulation of the plane strain tension test;  
 Updated model with increased clamping distance;  
 LS-DYNA library material model used for simulations  
*(back)*

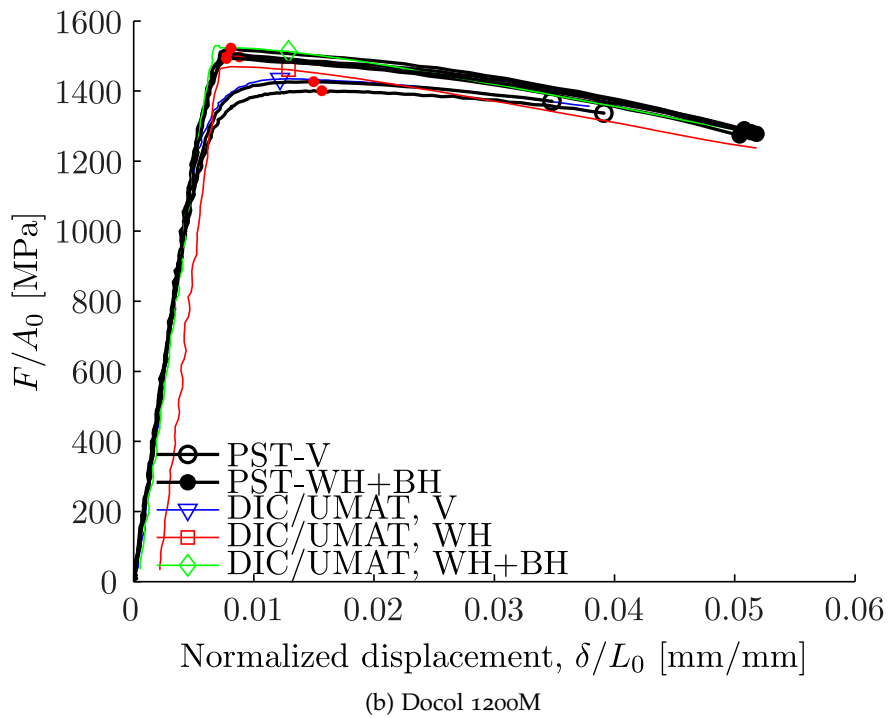
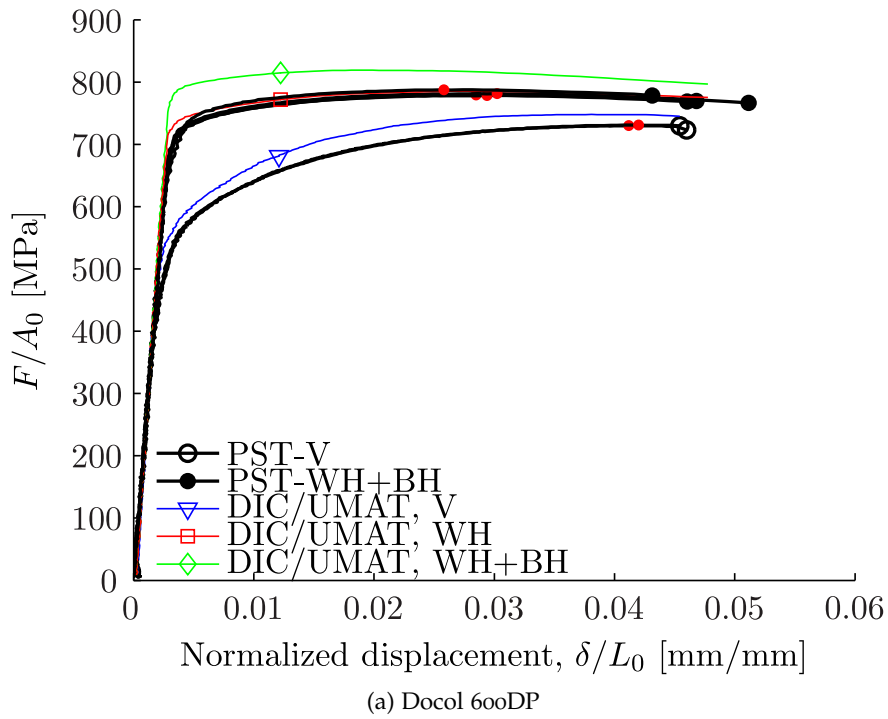


Figure 43: Analysis of the plane strain tension test using DIC strains as input to the SIMLab Metal Model constitutive driver

*(back)*

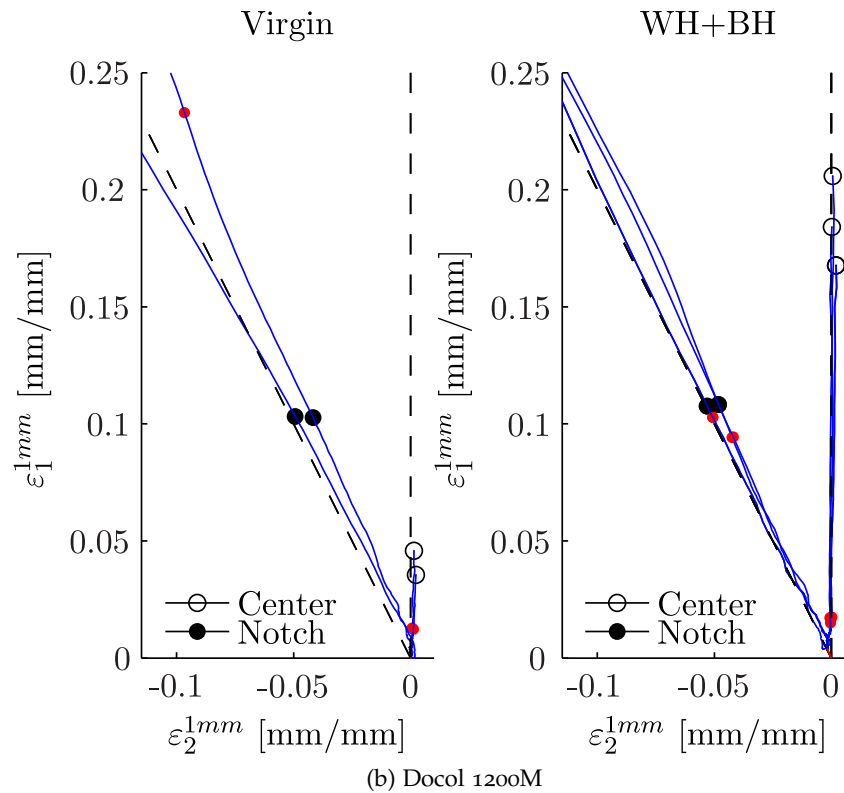
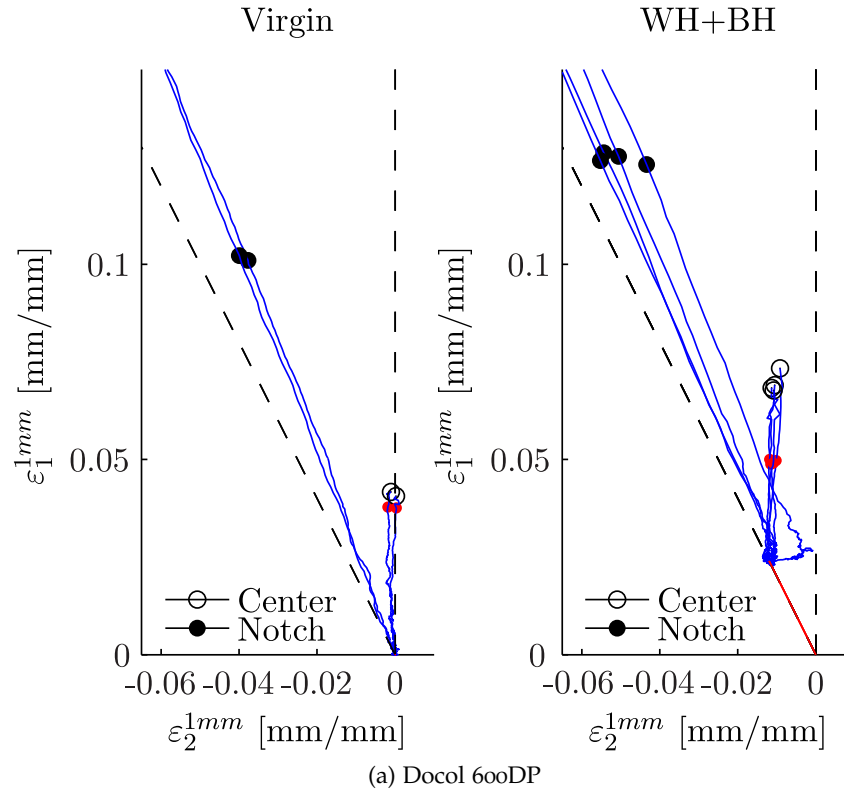


Figure 44: Major and minor strain paths, failure strains and fracture strains;  
Smoothed by moving average

(back)

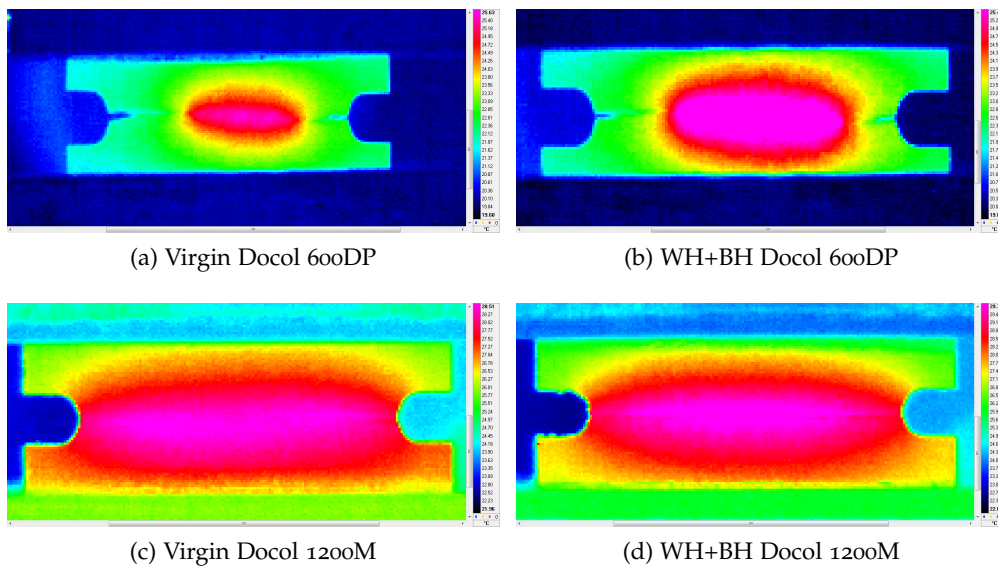


Figure 45: Last frame captured by thermographic camera before final rupture of PST specimen

(back)

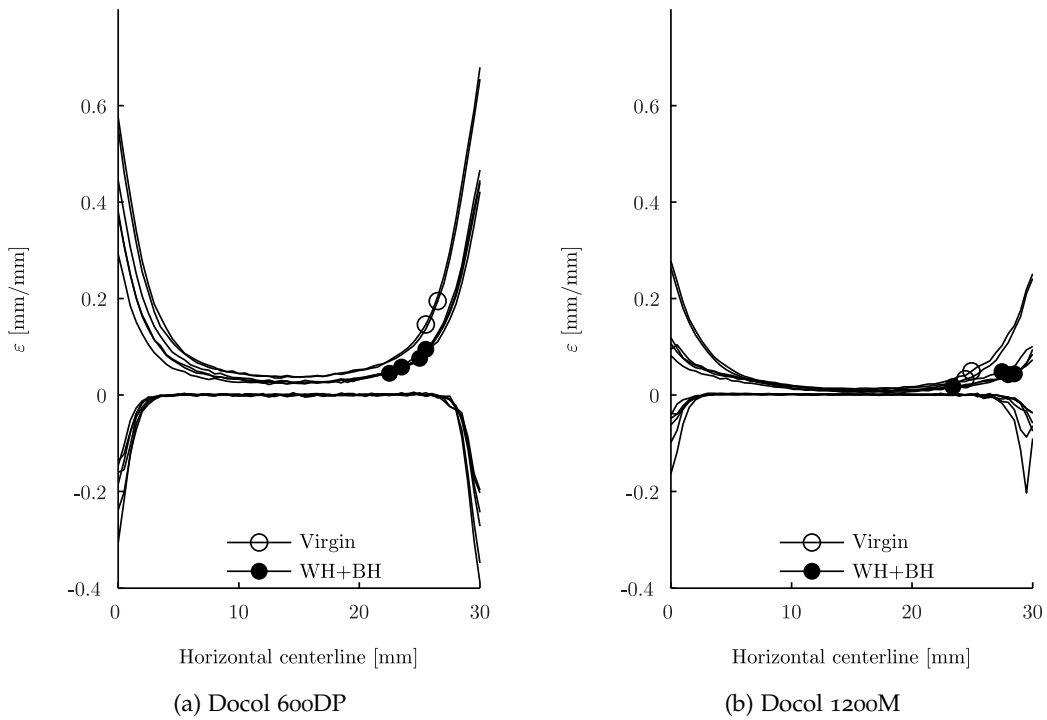


Figure 46: Strain distribution over horizontal centerline of PST specimen; Major and minor principal strains at maximum force

(back)

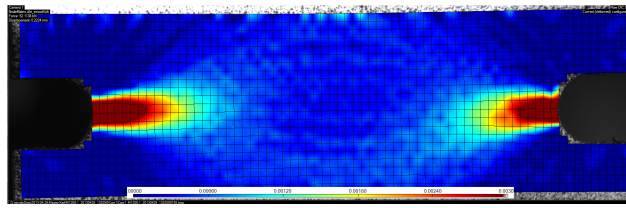


Figure 47: Total strain rate in a PST test of Docol 1200M after some plastic deformation; Colorbar range:  $(0, 3 \times 10^{-3}/s)$

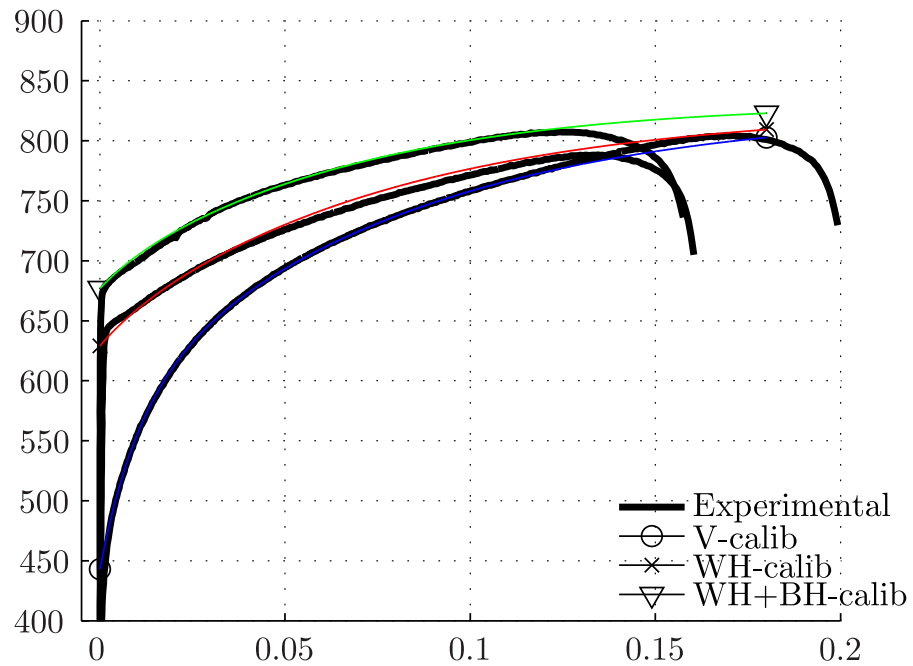
Table 1: Identified parameters of work hardening and bake hardening

		Present work							
		$\sigma_0$	$Q_1$	$\theta_1$	$Q_2$	$\theta_2$	$R_{BH}$	$Q_{BH}$	$\theta_{BH}$
		[MPa]	[MPa]	[-]	[MPa]	[-]	[MPa]	[MPa]	[-]
600DP	V	443	255	3334	129	12634			
	WH	629 <sup>(1)</sup>	186 <sup>(1)</sup>	2431 <sup>(1)</sup>	12 <sup>(1)</sup>	1185			
	WH + BH	629	186	2431	12	1185	48	-48	336
1200M	V	1052	117	11129	184	107430			
	WH	1255	80	7607	17.8	10400			
	WH+BH	1255	80	7607	17.8	10400	175	-125	62500
		After Hopperstad et al. [21]							
		$\sigma_0$	$Q_1$	$\theta_1$	$Q_2$	$\theta_2$	$R_{BH}$	$Q_{BH}$	$\theta_{BH}$
600DP	V	373	248	4811	186	30132			
	WH	-- (pre-strain used directly) --							
	WH+BH	-- (pre-strain used directly) --					54 <sup>(2)</sup>	-54 <sup>(2)</sup>	270 <sup>(2)</sup>
1200M	V	815	354	1086800	203	66381			
	WH	1311	60.5	19800					
	WH+BH	1311	60.5	19800			125	-50	150000

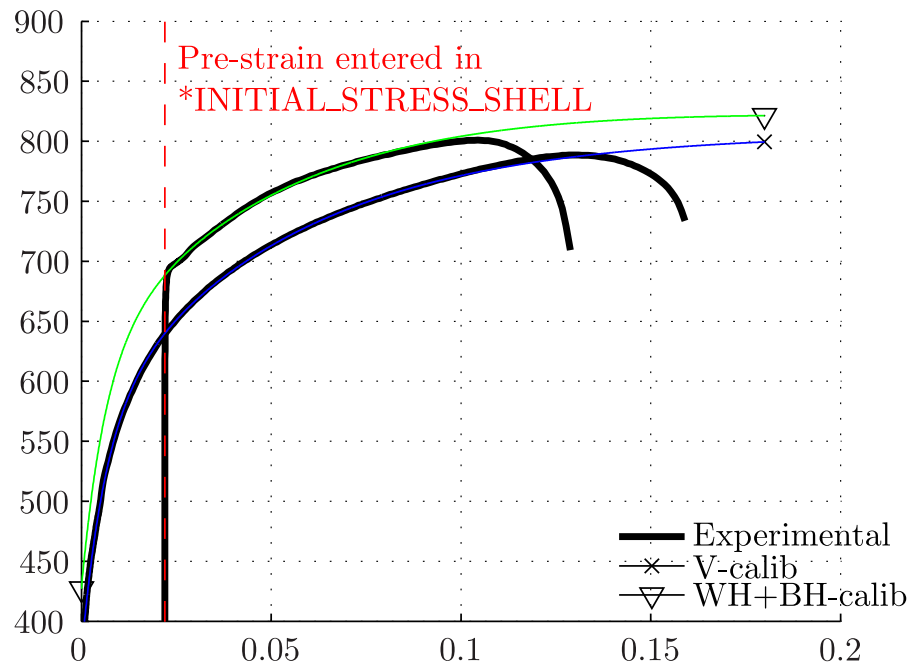
<sup>1</sup> Parameters obtained by shifting the calibrated virgin curve

<sup>2</sup> Original parameters have been extrapolated to zero plastic strain

(back)



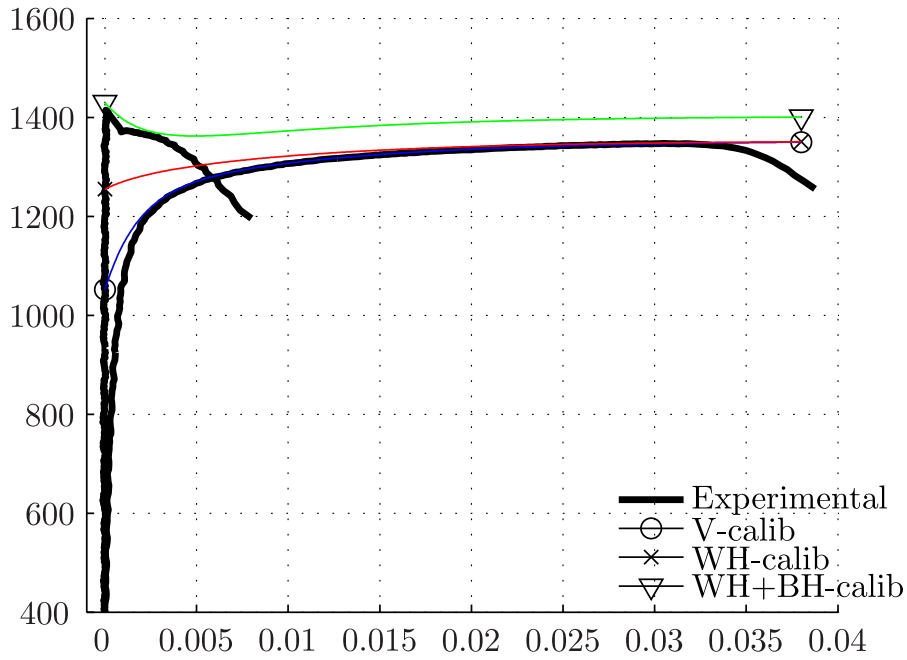
(a) Present work; Work hardening parameters for pre-strained material obtained by shifting the virgin curve



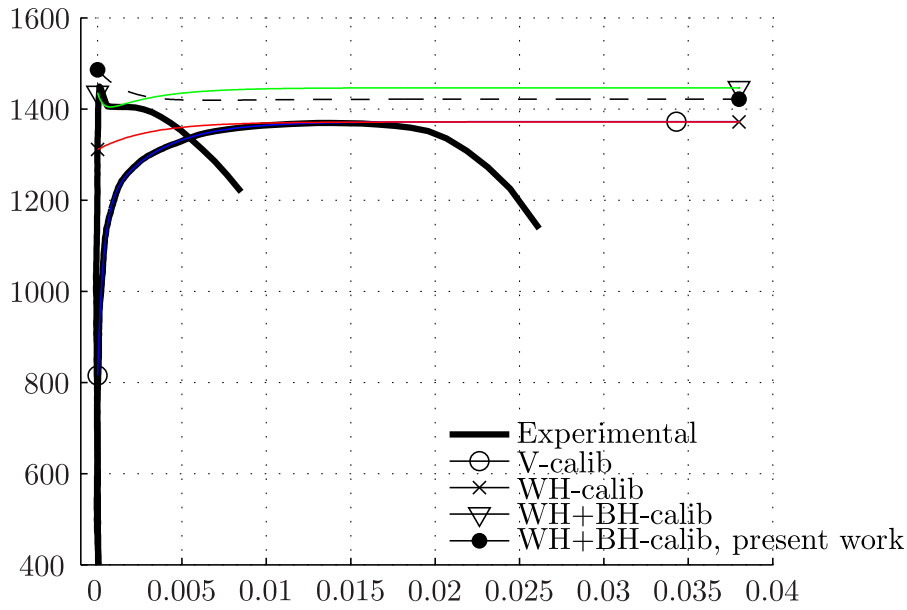
(b) Previous work; Bake hardening curve extrapolated to zero plastic strain

Figure 48: Calibration of hardening models, Docol 600DP

(back)



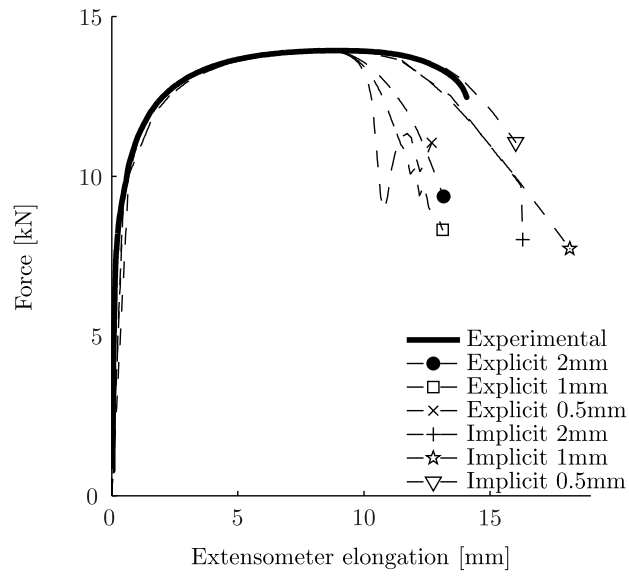
(a) Present work



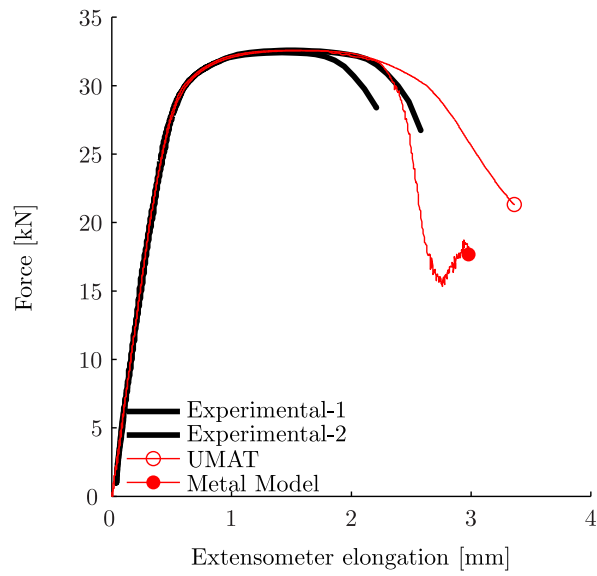
(b) Previous work

Figure 49: Calibration of hardening models, Docol 1200M;  
 Work hardening parameters for the pre-strained material obtained by shifting the virgin curve

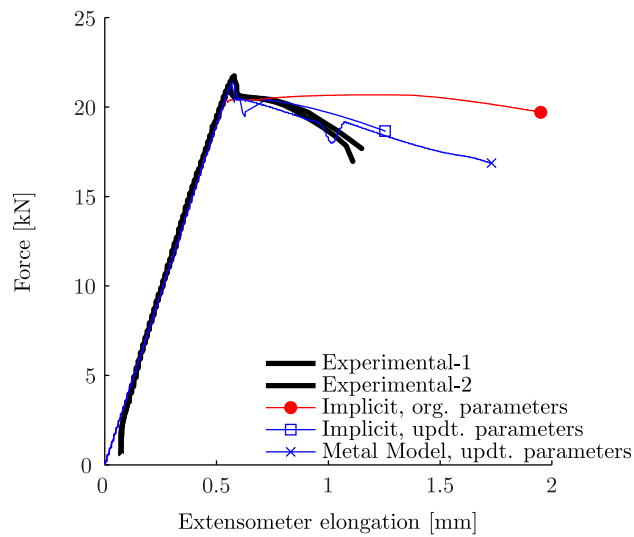
(back)



(a) Sensitivity study, virgin Docol 600DP



(b) Simulation, virgin Docol 1200M



(c) Simulation, WH+BH Docol 1200M

Figure 50: Sensitivity study, simulation and parameter identification of uni-axial tension test;  
 Experimental curves after [21]

(back)

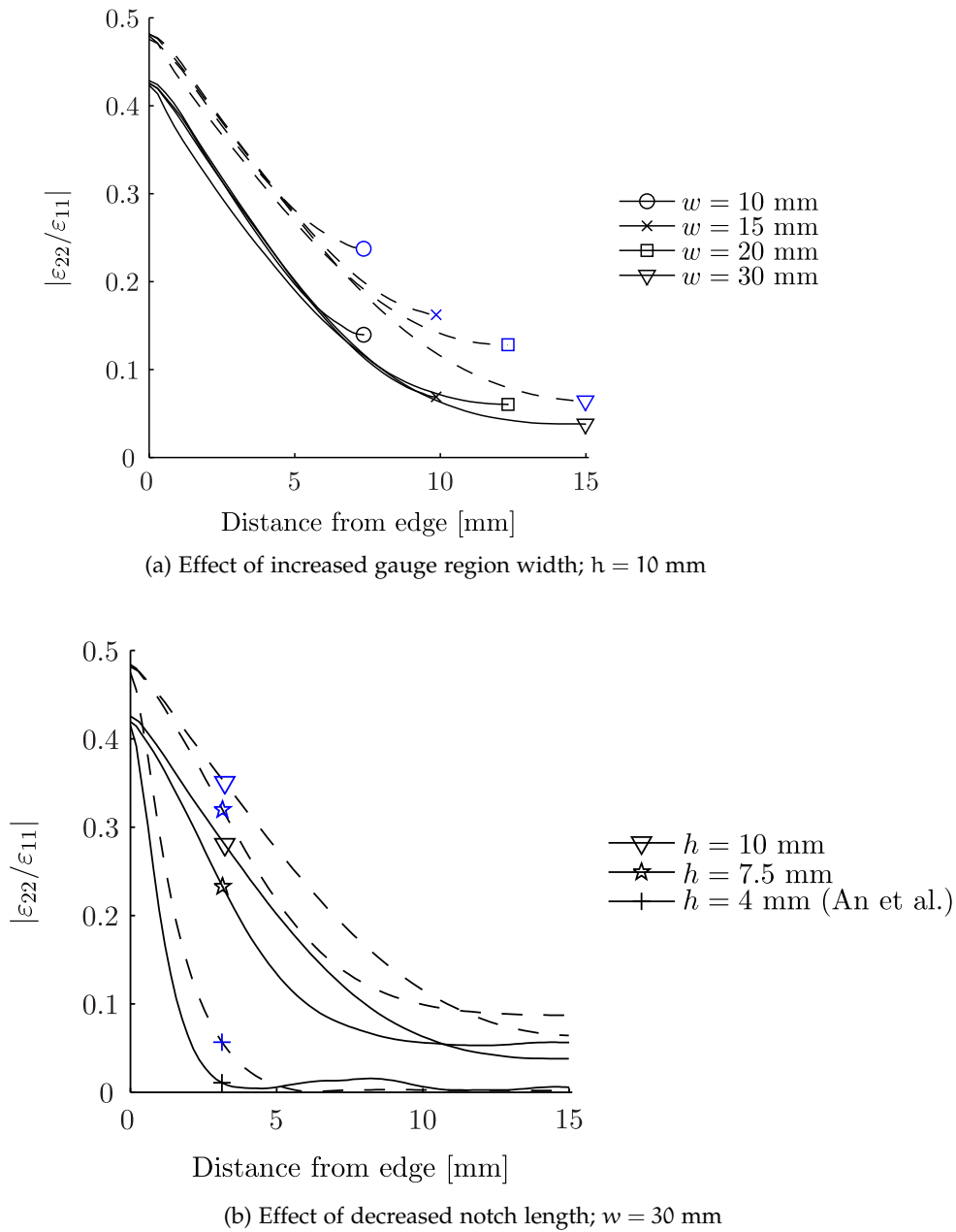


Figure 51: Strain distribution across gauge region due to variations of PST geometry;  
 Solid and dashed lines indicate strain distribution at incipient yielding of entire gauge region and after some uniform straining, respectively;  
 Corresponding geometry shown in [Figure 19 – 20](#)

*(back)*

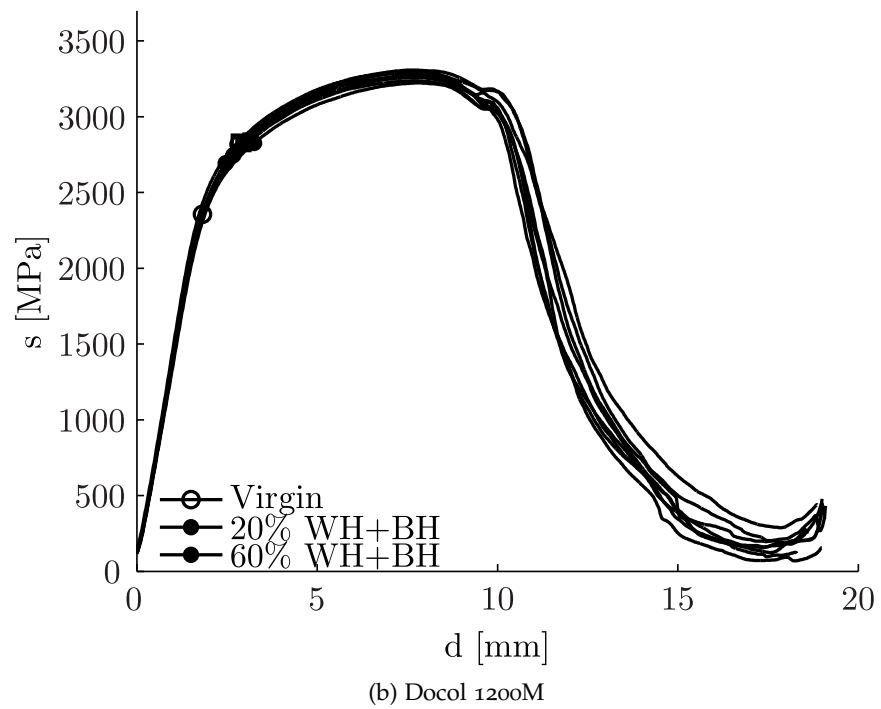
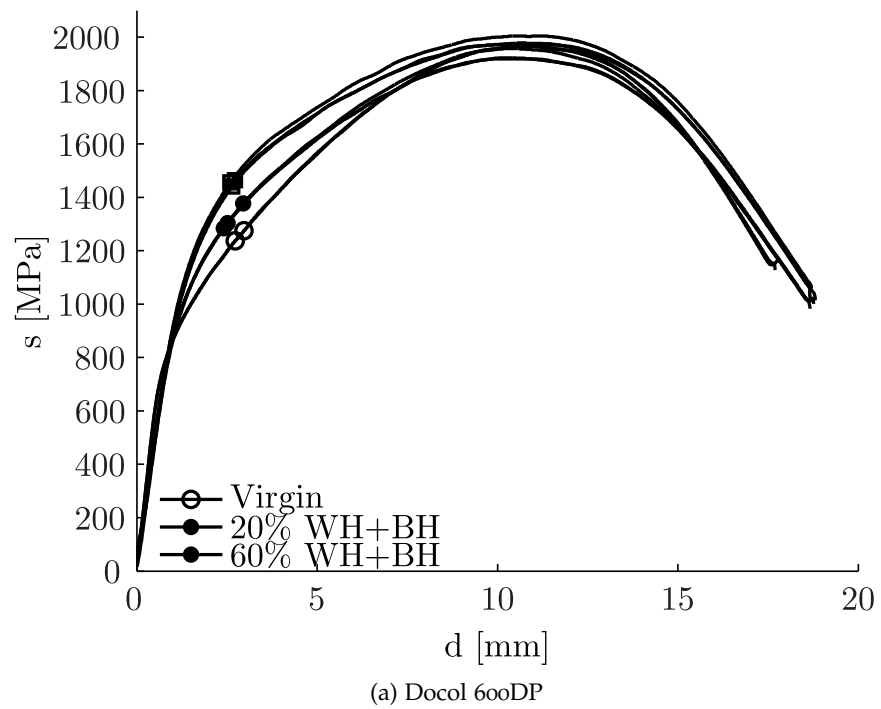
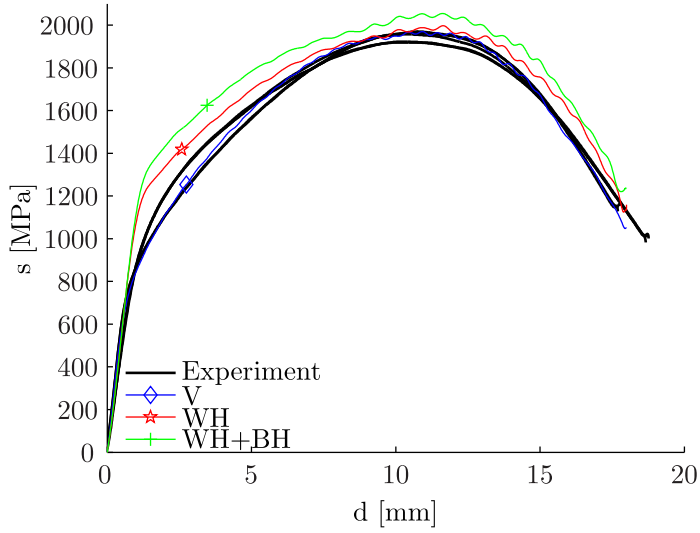
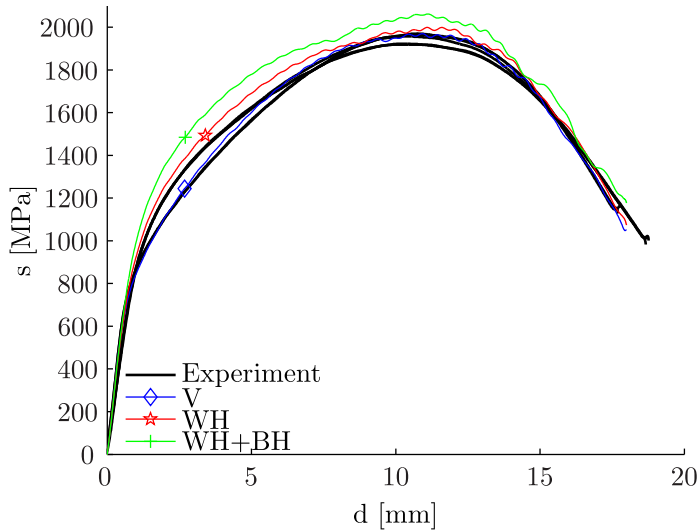


Figure 52: Results of previous experimental bending tests [26]

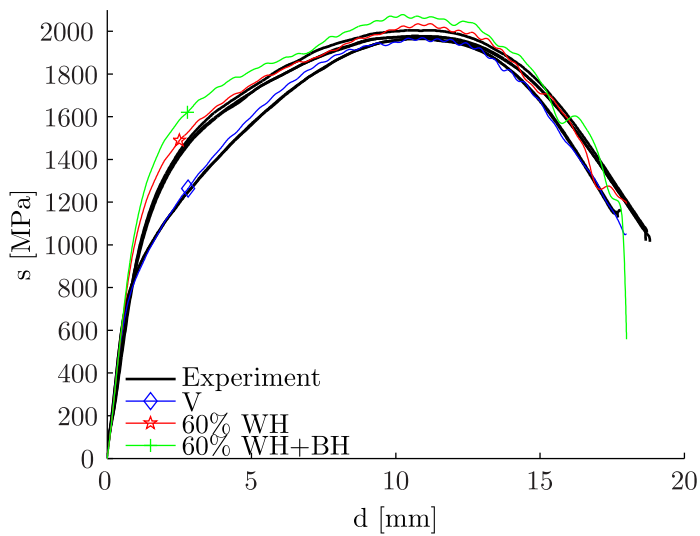
*(back)*



(a) Simulations with isotropic WH and isotropic BH



(b) Simulations with partly kinematic WH and isotropic BH



(c) Simulations with partly kinematic 60% WH and isotropic BH

Figure 53: Results of numerical simulations of the plane strain bending test; Docol 600DP

(back)

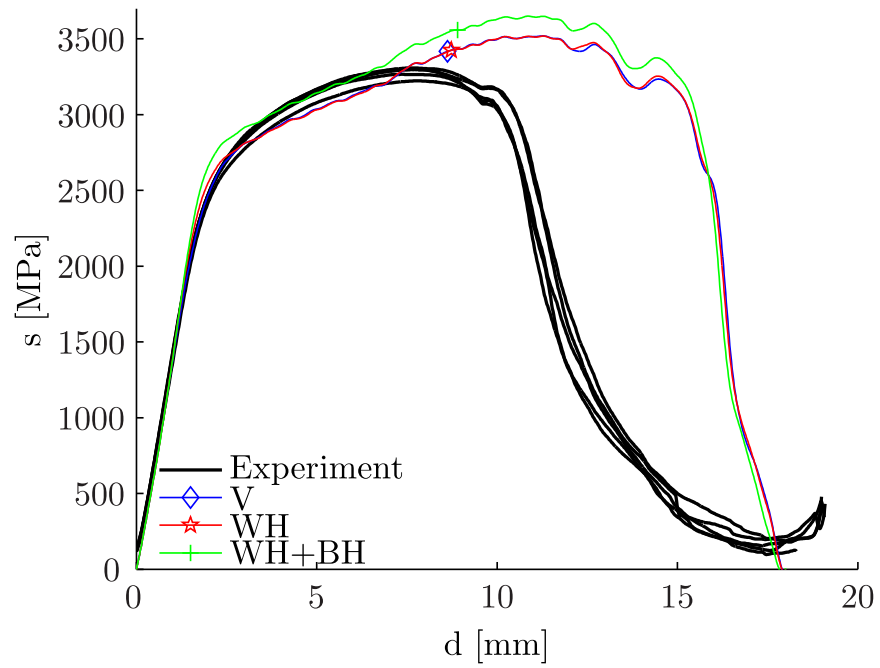


Figure 54: Results of numerical simulations of the plane strain bending test, Docol 1200M; Isotropic work and bake hardening assumed  
(back)

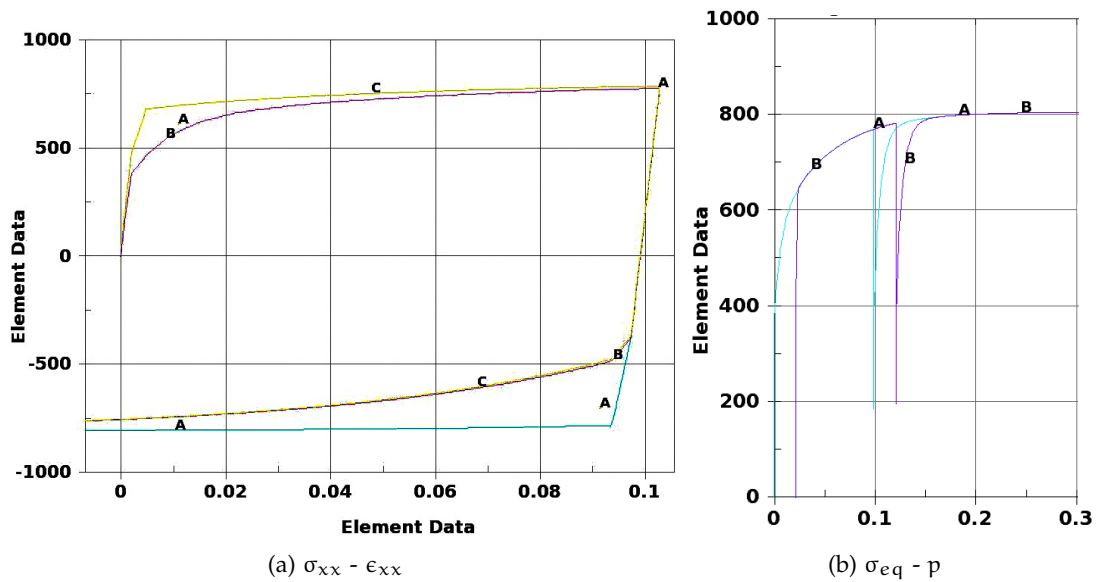


Figure 55: Cyclic tension-compression test of the single element model  
(back)

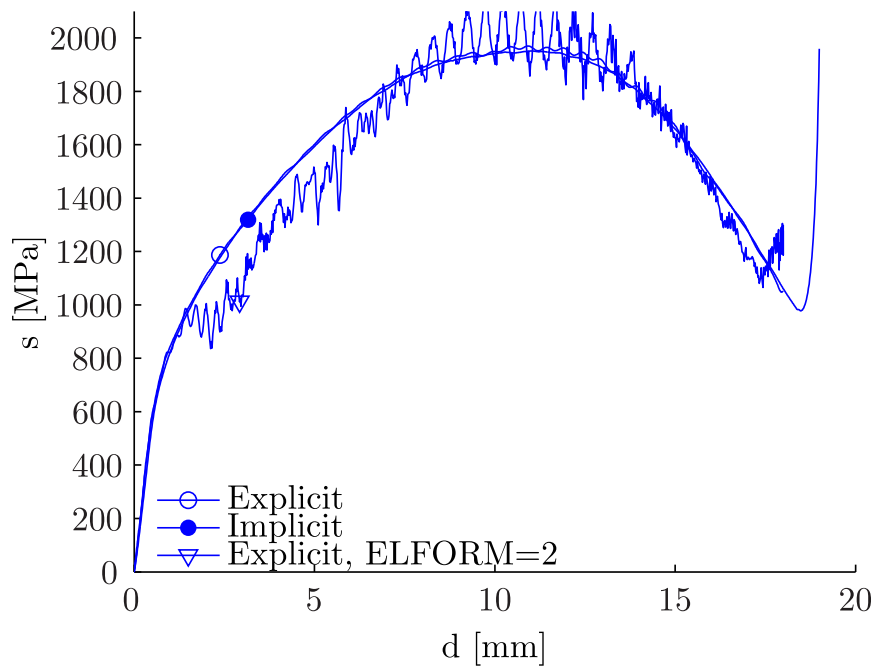


Figure 56: Sensitivity to time integration method and element formulation  
*(back)*

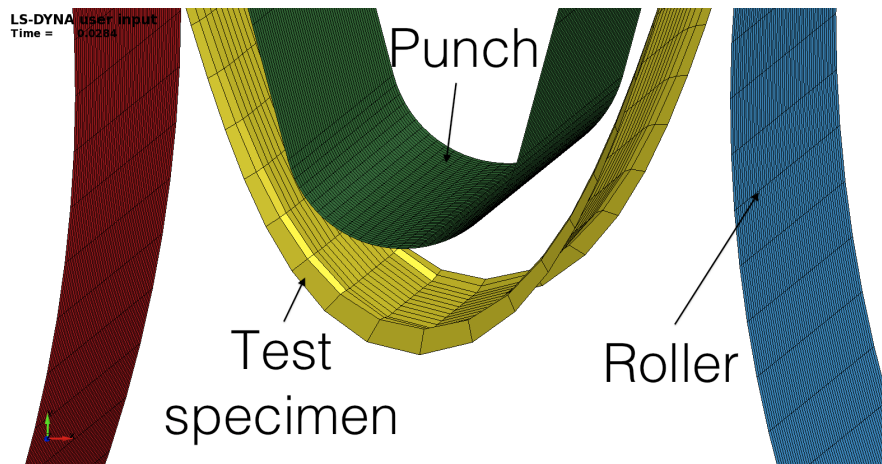


Figure 57: Close-up of deformation zone in plane strain bending simulation, showing the majority of the deformation taking place in a small number of elements

*(back)*



## DETAILS OF THE EXPERIMENTAL TESTS

---

### A.1 UNIAXIAL TENSION TEST

Table A.1: Details of the experimental uniaxial tension tests

Material	State	Specimen no.	Speed [mm/min]	Frame rate [1/s]	Extensometer length [mm]
600DP	V	1	6	2	70.8
	V	2	6	2	66.7
	WH	1	6	2	80.5
	WH	2	6	2	73.5
	WH+BH	1	6	2	61.7
	WH+BH	2	1.8	1	81.2
1200M	V	1	6	4	95.2
	V	2	6	4	89.8
	WH	1	6	4	86.7
	WH	2	6	2	98.3
	WH+BH	1	6	10	97.4
	WH+BH	2	6	10	100.3

Table A.2: Measured geometry and pre-strain level of the uniaxial tension test specimens; units in *mm* and % respectively

		Docol 600DP						Docol 1200M					
		V		WH		WH+BH		V		WH		WH+BH	
		1	2	1	2	1	2	1	2	1	2	1	2
Width	mean	19.99	20.01	19.74	19.75	19.75	19.75	19.94	19.97	19.95	19.96	19.96	19.93
	std. dev.	0.017	0.002	0.023	0.018	0.024	0.005	0.024	0.0130	0.016	0.019	0.016	0.013
Thickness	mean	1.19	1.19	1.18	1.18	1.18	1.18	1.24	1.24	1.24	1.24	1.24	1.24
	std. dev.	0.001	0.003	0.002	0.002	0.001	0.002	0.001	0.00?	0.003	0.002	0.002	0.002
R <sub>80</sub>		0	0	2.27	2.45	2.42	2.43	0	0	0.39	0.38	0.40	0.40

## A.2 PLANE STRAIN TENSION TEST

Table A.3: Details of the experimental plane strain tension tests

Material	State	Specimen no.	Speed [mm/min]	Frame rate [1/s]	Gauge region thickness [mm]
600DP	V	1	1	2	1.190
	V	2	1	1	1.195
	WH+BH	4	1	1	1.189
	WH+BH	5	1	1	1.185
	WH+BH	7	1	1	1.185
	WH+BH	8	1	1	1.181
1200M	V	1	1	1	1.237
	V	2	1	1	1.244
	WH+BH	4	1	1	1.246
	WH+BH	5	1	1	1.237
	WH+BH	7	1	1	1.237
	WH+BH	8	1	1	1.237

NOTE: Gauge region width was measured at approx 29.9 mm



## BIBLIOGRAPHY

---

- [1] Steel - determination of yield strength increase by the effect of heat treatment (bake-hardening-index). *Standard SS-EN 10325:2006-10*, 2006.
- [2] Y.G. An, H. Vegter, and L. Elliott. A novel and simple method for the measurement of plane strain work hardening. *Journal of Materials Processing Technology*, 155-156(1-3):1616–1622, 2004.
- [3] L. J. Baker, S. R. Daniel, and J. D. Parker. Metallurgy and processing of ultralow carbon bake hardening steels. *Materials Science and Technology*, 18(4):355–368, April 2002.
- [4] V. Ballarin, A. Perlade, X. Lemoine, O. Bouaziz, and S. Forest. Mechanisms and Modeling of Bake-Hardening Steels: Part II. Complex Loading Paths. *Metallurgical and Materials Transactions A*, 40A:1375–1382, June 2009.
- [5] V. Ballarin, M. Soler, A. Perlade, X. Lemoine, and S. Forest. Mechanisms and Modeling of Bake-Hardening Steels: Part I. Uniaxial Tension. *Metallurgical and Materials Transactions A*, 40A:1367–1374, June 2009.
- [6] A. Barata da Rocha, F. Barlat, and J. M. Jalinier. Prediction of the Forming Limit Diagrams of Anisotropic Sheets in Linear and Non-linear Loading. *Materials Science and Engineering*, 68:151–164, 1985.
- [7] W. Bleck. Trends in Automotive Steel Development. *Asia Steel International Conference Proceedings*, September 2012.
- [8] W. Bleck, S. Brühl, T. Gerber, A. Katsamas, R. Ottaviani, L. Samek, and S. Traint. Control and exploitation of the bake-hardening effect in multi-phase high-strength steels. Technical Report EUR 22448 EN, ISBN: 978-92-79-04608-7, Office for Official Publications of the European Communities, 2007.
- [9] J. Chakrabarty. *Theory of plasticity*. McGraw-Hill Ryerson, Limited, third edition edition, 2006.
- [10] A. H. Cottrell and B. A. Bilby. Dislocation Theory of Yielding and Strain Ageing of Iron. *Proceedings of the Physical Society*, 62: 49–62, 1949.
- [11] A.K. De, S. Vandeputte, and B.C. De Cooman. Static Strain Aging Behavior of Ultra Low Carbon Bake Hardening Steel. *Scripta Materialia*, 41(8):831–837, 1999.

- [12] SIMLab Metal Model development team. Theory manual: SIMLab Metal Model. Technical Report Rev. Fall 2012, CRI SIMLab, Norwegian University of Science and Technology, 2012.
- [13] V. Dmitry. Unpublished dissertation draft. Norwegian University of Science and Technology, 2013.
- [14] L. Durrenberger, X. Lemoine, and A. Molinari. Effects of pre-strain and bake-hardening on the crash properties of a top-hat section. *Journal of Materials Processing Technology*, 211(12):1937–1947, 2011.
- [15] E. Fagerholt. *Field measurements in mechanical testing using close-range photogrammetry and digital image analysis*, 2012:95. PhD thesis, Norwegian University of Science and Technology, 2012.
- [16] E. L. Fasanella and K. E. Jackson. Best Practices for Crash Modeling and Simulation. Technical Report NASA/TM-2002-211944, ARL-TR-2849, NASA, 2002.
- [17] G. Gruben. *Ductile fracture in dual-phase steel*. PhD thesis, Norwegian University of Science and Technology, 2012.
- [18] J. Hagström and L. Ryde. Bake Hardening in Dual Phase and Martensitic High Strength Steels. Technical Report KIMAB-2008-101, Swerea KIMAB, 2008.
- [19] S. Hiwatashi and S. Yonemura. Anisotropic increase in yield strength by straining and baking of bake-hardenable steel. *Materials Science Forum*, Vols. 495-497:1485–1492, 2005.
- [20] O. S. Hopperstad, O-G. Lademo, and A. Benallal. The bake-hardening effect in high-strength steels – Phase I: Preliminary considerations. Draft Report, 2009.
- [21] O. S. Hopperstad, O-G. Lademo, J. Larsson, and A. Benallal. The bake-hardening effect in high-strength steels – Phase II: Literature review, experiments and modelling. Draft Report, 2009.
- [22] Heike Kantereit. Bake hardening behavior of advanced high strength steels under manufacturing conditions. Technical Report 2011-01-1053, SAE International, April 2011. URL <http://dx.doi.org/10.4271/2011-01-1053>.
- [23] O.-G. Lademo. *Engineering Models of Elastoplasticity and Fracture for Aluminium Alloys*. PhD thesis, Norwegian University of Science and Technology, 1999.
- [24] O.-G. Lademo, M. Eriksson, Aa. Reyes, O.S. Hopperstad, and M. Langseth. Characterisation of failure and identification of failure related parameters. Technical Report STF80MK Fo6083, SINTEF Materials and Chemistry, 02 2006.

- [25] O.-G. Lademo, O. Engler, S. Keller, T. Berstad, K. O. Pedersen, and O. S. Hopperstad. Identification and validation of constitutive model and fracture criterion for AlMgSi alloy with application to sheet forming. *Materials and Design*, 30:3005–3019, 2009.
- [26] O.-G. Lademo, J. Larsson, O. S. Hopperstad, T. Berstad, and A. Benallal. Experimental and numerical study on bake hardening in dual-phase and martensitic steels. Workshop presentation, 2010.
- [27] R. Larsson and L. Nilsson. On the modelling of strain ageing in a metastable austenitic stainless steel. *Journal of Materials Processing Technology*, 212(1):46–58, 2012.
- [28] M. S. Rashid. *Transactions of the Metallurgical society of AIME*, 7: 498, 1949.
- [29] S. Siriram, B. Yan, and M. Huang. Characterization of press formability of Advanced High Strength Steels using laboratory tests. Technical Report 2004-01-0506, SAE Technical Paper Series, 2004.
- [30] SSAB. Docol M Cold reduced martensitic steels. Technical report, Swedish Steel AB, Accessed 2013-04-02. URL [http://www.ssab.com/Global/DOCOL/datasheets\\_docol/en/207\\_Docol%20M.pdf](http://www.ssab.com/Global/DOCOL/datasheets_docol/en/207_Docol%20M.pdf).
- [31] SSAB. Docol DP/DL Cold reduced dual-phase steels. Technical report, Swedish Steel AB, Accessed 2013-04-02. URL [http://www.ssab.com/Global/DOCOL/datasheets\\_docol/en/201\\_Docol%20DP%20DL.pdf](http://www.ssab.com/Global/DOCOL/datasheets_docol/en/201_Docol%20DP%20DL.pdf).
- [32] D. V. Wilson and B. Russel. Stress Induced Ordering and Strain-Ageing in Low Carbon Steels. *Acta Metallurgica*, 7:628–631, 1959.
- [33] D. V. Wilson and B. Russel. The Contribution of Atmosphere Locking to the Strain-Ageing of Low Carbon Steels. *Acta Metallurgica*, 8:36–45, 1960.
- [34] D. V. Wilson and B. Russel. The Contribution of Precipitations to Strain Ageing in Low Carbon Steels. *Acta Metallurgica*, 8:468–479, 1960.